VISUALIZATION AND NUMERICAL ANALYSES FOR MASS TRANSPORT DUE TO INTERNAL WAVES PROPAGATING IN THE DENSITY-STRATIFIED WATER WITH A DIFFUSIVE TRANSITION LAYER

By

NGUYEN KIM CUONG

A dissertation submitted for

the Degree of Doctor of Engineering

TOKYO METROPOLITAN UNIVERSITY

Graduate School of Urban Environmental Sciences

Department of Civil and Environmental Engineering

September, 2013

Contents

List of Figures

List of Tables

Acknowledgements

I had a great opportunity to improve my knowledge when I was granted the Asian Human Resources Fund supported by the Tokyo Metropolitan Government under the project "***Solutions for the water related problems in Asian metropolitan areas***" for taking a PhD course in the Tokyo Metropolitan University. I foremost would like to thank the financial support by Tokyo Metropolitan Government.

I would like to express sincere appreciation to my supervisor, Professor Motohiko Umeyama for selecting me as his PhD student, for his orientation, and numerous supports in researching this work.

I also would like to convey my sincere thanks to Dr. Tetsuya Shintani and his family members for their continuous supports for both my study and daily life in Japan.

It is my honor to send my sincere gratitude to Professor Masahito Asai (Department of Aerospace Engineering) and Associate Professor Katsuhide Yokoyama, for agreeing to be members in my examination committee, for spending their time to review my dissertation, and for providing me with very constructive suggestions and comments.

During my research, I received important supports from Faculty of Hydro-Meteorology and Oceanography – Hanoi University of Science – Vietnam National University, Hanoi, particularly, Professor Dinh Van Uu - Head of Department of Oceanography. I greatly appreciate their kindness and their supports during my doctoral study.

I would like to thank to my "senpai," Mr. Nguyen Hoang Duc, for his guides and to the students who carried out various experiments with me. Without their collaborations, I could not complete this dissertation.

My thanks are given to all colleagues and friends, both in Japan and Vietnam, who provided me the valuable datasets as well as shared with me their knowledge, experiences, and interests that indirectly inspired me to start and complete this study. I would like to thank my all Vietnamese friends, particularly, Nguyen Thanh Thuy, Nguyen Thi Hoang Anh, Bui Thu Ha, Bui Du Duong, Nguyen Quang Hung… in Tokyo Metropolitan University (VN-TMU) for their friendly helps, encouragements of homesickness, as well as share our sense of humors and delightful moments together during my ever-busy research life.

I am very grateful to my best friend, Nguyet Le, for her supports and sharing my difficulties every day during 3 years in Japan.

The last but not least, I would like to thank my parents, uncles, sisters, brothers-in-law, and my beloved nieces for giving me their trust, encouragement, and plenty supports.

Nguyen Kim Cuong

Tokyo, September 2013.

Summary

In general, below sea surface, water can be divided into three layers: (i) mixing layer, (ii) thermocline, and (iii) deep layer. Internal waves form at the thermocline over the edge of a steep bottom feature. These waves transport a considerable amount of energy and momentum horizontally and vertically. The study of internal waves in the density-stratified water is essential to the coastal environment because they cause the transport of planktonic larvae from the offshore to the coast and the mixing between subsurface water and bottom water. The shoaling and breaking of internal waves play important roles in the suspension, transport, and deposition of sediments in the ocean bottom. Knowing the water particle motion in an internal wave cycle is the key to solving the transport phenomenon. The subject may be of considerable importance for nearshore internal wave problems; however, the number of such investigations is still limited compared with those concerning nonlinear wave shapes. This is due to the inconvenience of describing the particle velocity and path experimentally under wave motion in the Lagrangian system. Use of recent imaging technique has made it possible to investigate the mechanism of internal waves in a wave tank. The latest developments in Particle Image Velocimetry have led to the visualization of velocity fields and particle paths.

Although the essential problems arising from the motion of internal waves approaching the coastal areas are changes in wave characteristics and wave-induced flows, the peculiar features of mass transport in a shallow water region are still not understood. The objective of this study is to measure and quantify the physical quantities of internal waves over a flat bottom and a uniform slope during a runup event using experimental techniques and a two-dimensional non-hydrostatic numerical model. Mass transport by internal wave is focused to investigate in the density-stratified water with a diffusive transition layer. For a two-layer density-stratified water, mass transport property has been quantified as the function of wave parameters and thickness ratios between the upper and lower layers.

Chapter 1

Introduction

1.1. Brief introduction to internal waves

1.1.1 History of internal waves

Nowadays, human being know more about the universe than the oceans. It is easier to send a person to space than to the bottom of the ocean. The ocean is dark and cold with the deepest portion of 11.034 km at the Challenger Deep (Mariana Trench). With its physical, biological, or chemical characteristics, such as wave, current, salinity, temperature, life inside ocean are still great unknown. Although there was an early knowledge of surface waves even to the primitive people, internal waves were discovered only in the years of 1900.

Internal gravity waves are water motions originating from density variations within the water body (Vlasenko et al, 2005). They arise from perturbations of hydrostatic equilibrium, wherein a balance is maintained between the gravity and buoyant restoring forces. Internal waves propagate inside the ocean or lake; therefore, people were oblivious of its existence, as against the surface waves. However, people took notice of the existence of internal wave later owing to its related phenomena as “dead water” or huge slick in the ocean surface. “Dead water” is a nautical term used to refer to a strange phenomenon in which a ship is hard to maneuver and/or is slowed down almost to a standstill on a fluid that is apparently still. The phenomenon of “dead water” was first observed by Fridjof Nansen during his polar cruise in 1892 (Defant, 1961). His heavy vessel “Fram,” which had a weak engine, proved to be very sensitive to the “dead water.” It seemed to him that there was a thin layer of light water superposed on heavier water. The vessel was stopped when it was at a relatively slow speed. A slight increase in the speed seemed to be sufficient to overcome the effect of the “dead water.” This phenomenon had been observed in the Baltic and the Kattegat (Meyer, 1904). Subsequently, Ekman performed theoretical and experimental studies (Nansen, 1904), and showed the mechanism to generate internal waves by a slow moving vessel. His experiments showed that there is presence “dead water” when the speed

of the ship remains below a threshold value. If the speed exceeds this value, only external waves are generated. However, the existence of true internal waves had been only proved when Helland–Hansen and Nansen (1909) introduced their first hydrographic observations repeated at short intervals over a long period. They confirmed that the internal waves appeared especially in zones where the discontinuity layer of density is well-developed. **Fig. 1.1** clearly illustrates the phenomenon of "dead water" as internal waves generated by the movement of a ship.

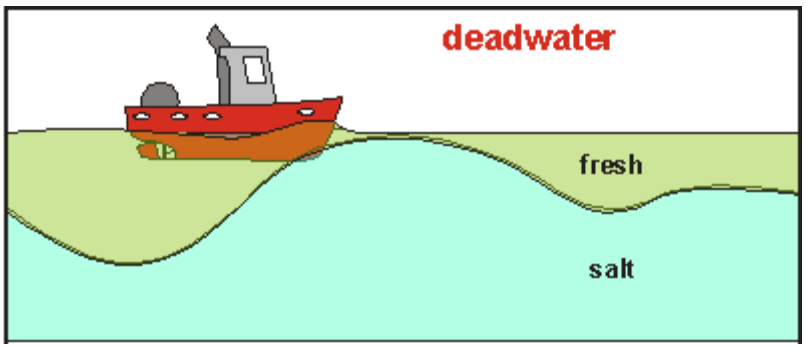

Fig. 1.1 Sketch of "dead water" phenomenon (Anthoni, 2000)

There was an urgent motivation to investigate the phenomenon of internal waves following several losses of modern submarines. One of the victims is the submarine USS Thresher that sank on April 10, 1963 with 129 members and civilians abroad. Although the Thresher had been the most advanced submarine in the world during that time, there was no indicator in it for equipment malfunction or for notifying unusual storm weather (Pinet, 1992, p. 220). However, later, even the Thresher was no more. The scientists speculated that it was probably cruising along a pycnocline when it encountered a large internal wave that moved the submarine down to a depth below the pressure capacity of the hull. Five min prior to the implosion, the Thresher had radioed through the UQC: "*Experiencing minor problem. Have positive angle. Attempting to blow.*" Apparently, the incident occurred too quickly for crew members to reduce the submarine's density to arrest their fall (Grue, 2006).

In the 1960s, the development of fast internally recording vertical arrays ("chains") of thermistors led to the observations of large internal waves in the coastal oceans and marginal seas (Helfrich and Melville, 2006). Perry and Schimke (1965) found internal-wave groups up to 80-m high and 2000-m long on the main thermocline at 500 m in water that was 1500-m deep in the Andaman Sea. From observation of offshore temperature variations, LaFond (1959) found that time-dependent isotherms are flattened for a shallower thermocline and peaked for a deeper thermocline on the wave crests. Osborne and Burch (1980) proved that

waves are generated owing to tidal flows through the channels in the Andaman and Nicobar island chains. Their observation showed that internal waves propagated toward the Sumatra coastline some hundreds of kilometers away. Such types of observations had been performed in other instances as in the following cases: LaFond (1959) in the inshore waters off Mission Beach; Ziegenbein (1969) in the Strait of Gibraltar; Halpern (1971) or Haury et al. (1979) in Massachusetts Bay; Thorpe (1971) in Loch Ness; Hunkins and Fliegel (1973) in Seneca Lake, New York etc. **Fig. 1.2** depicts a measurement of internal waves by using suspended thermistors performed by LaFond (1959).

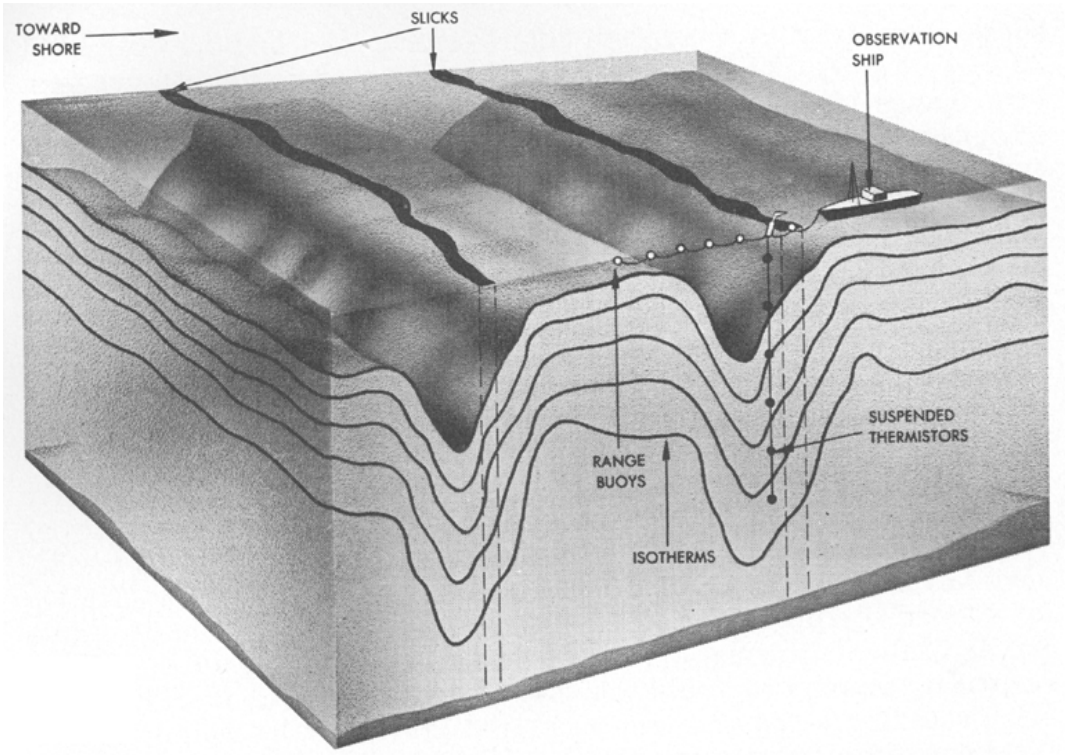

Fig. 1.2 Three-dimensional representation of internal waves in the inshore water off Mission Beach, San Diego (LaFond, 1959)

From the last 30 years of the 20th century up till now, with the development of remote sensing techniques, the presence of internal waves could be inferred from scattering of marine radar from short surface waves (Ziegenbein, 1969). Shand (1953) found internal wave fronts appearing on aerial photographs. The propagation of internal waves becomes apparent and can be captured in oceans. Apel et al. (1975, 1976, 1985) reported a series of research results for the internal waves observed in pictures from satellites, space shuttles, and aircraft. In addition to these indirect photographs, they also used various instruments such as the expendable bathythermograph, acoustic echo sounding, and ship radar. Apel et al. (1975)

processed the images from Earth Resources Technology Satellite collected in August 1972, May 1973, and July 1973, and reported the existence of internal waves in the New York Bight and the southwest coast of Africa. The SEASAT satellite was launched in 1978 with the synthetic aperture radar (SAR) that can capture images of ocean surface roughness. These SAR images demonstrated that the packets of shoreward-propagating internal waves, separated by tidal periods, were a ubiquitous feature of the coastal oceans (Fu and Holt, 1982) (see **Fig. 1.3**). Recently, the modern satellites improved the ability to capture the sea surface roughness with higher spatial and temporal resolutions. Their products become the key for monitoring the propagation of internal waves in the ocean. **Fig. 1.3** shows the areas in coastal ocean where the phenomena of internal waves have been captured by satellites. It could conclude that internal waves are general phenomenon of almost coastal region in the world.

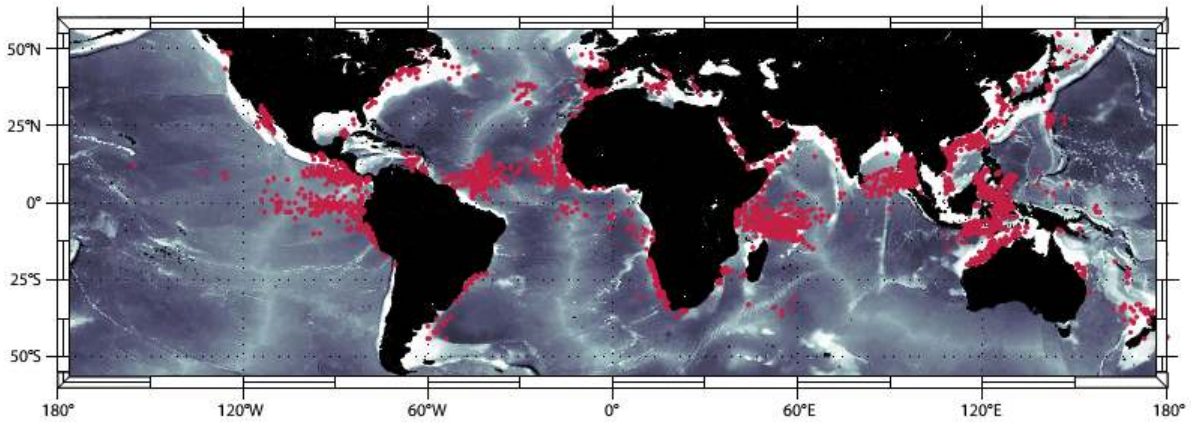

Fig. 1.3 Locations of nonlinear internal waves observed in 250 m resolution MODIS satellite sunglint imagery acquired from August 2002 through May 2004 (Jackson 2007).

1.1.2 Theoretical investigations of internal waves

Internal waves occur on interfaces between layers of different densities (**Fig. 1.4**). The internal waves cover deep waters of seas and oceans because the deep waters have a higher density than the waters above them. Internal waves act like surface waves. They can also propagate, distort, and break just like surface waves. Although internal waves cannot be seen by the human eye, they can be detected by studying temperature or salinity changes at a given location. In an ocean or a lake, the length of these waves could range from tens to hundreds of kilometers, while its height can reach 200 m. The typical velocity associated with internal waves is 5 cm/s. The typical period can range from min to h.

Theory of internal waves in a two-layer fluid was first introduced by Stokes (1847). He treated the interfacial movement in a fluid consisting of two layers of finite thickness. By assuming the existence of velocity potentials, the solutions for velocity potentials for the upper and lower layers of stratified fluid and wave celerity can be obtained. Rayleigh (1883) was the first to investigate wave motions for continuously stratified fluid. Love (1891) derived a solution for wave motion with an approach similar to that of Rayleigh, except that fluid was assumed to be irrotational. Later, Lamb (1932) presented an excellent description of wave motion in a two-layer fluid and an exponential density distribution fluid. His work was similar to that of Rayleigh (1883) and Love (1891). However, Lamb was the first to treat wave motion in a heterogeneous fluid as a physical problem behind each case, as opposed to a pure mathematical problem.

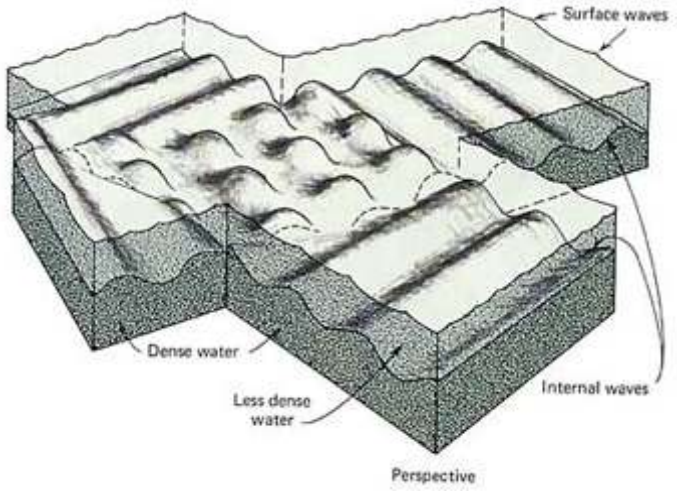

Fig. 1.4 Internal waves at interface between two layers of water of different densities (Gross, 1990).

Recently, Harleman (1961) and Gill (1982) introduced an important concept that wave motion in a two-layer fluid correlates the wave height ratio between the internal wave and surface wave. However, the solutions derived are inconsistent. On the other hand, Gill (1982) gave solutions in term of two widely separated roots. The larger one, called barotropic mode, was for the condition when the pressure being constant on a surface of constant density, and the smaller root, called baroclinic mode, was for the pressure that was not constant on a surface of constant density.

It is well known (Benjamin, 1966, 1967; Benney, 1966) that long nonlinear internal waves are possible in a density stratified fluid. In an analogy to the classical long wave theory,

both Benjamin and Benney used a two parameter perturbation expansion method to find a governing equation similar to the Korteweg-de Vries (KdV) equation.

Kubota et al. (1978) and Choi and Camasa (1996, 1999) performed a series of investigations to derive model equations for weak and strong nonlinear wave propagations in stratified fluids. The upper boundary is allowed to be either free or rigid. They used the following assumptions: (i) the wavelength of the interfacial wave is long; (ii) the upper layer is thin, and (iii) no depth restriction is made on the lower layer.

The development of internal wave theories is very impressive for predicting the interfacial displacement and velocity. However, the problem of mass transport was not concentrated to have suitable formula to predict the magnitude and direction in the ocean. The detailed problems for mass transport investigation will be introduced in following parts.

1.1.3 Experimental investigations of internal waves

Numerous experiments have been performed to investigate the shoaling and breaking of internal waves on various slopes fabricated in hydraulic laboratories. Thorpe (1968) examined the breaking and runup of internal waves propagating between two density-stratified layers. Close to a point of contact between the density interface and bottom slope, internal waves steepen at the front as the lower layer becomes shallow; however, the crests break backwards. On the upper slope, the wave becomes a blob and the dense fluid returns down the slope like a density current. Finally, a head-on collision occurs between the backflow and incident waves. Wunsch (1971) considered the second-order mass and momentum flux carried by the internal waves that encounter a shoaling region, and the wave set-up and set-down of the mean density interface caused by the Stokes drift. Using electrical conductivity meters and a shadowgraph technique, Cacchione and Wunsch (1974) performed a series of laboratory experiments for internal waves in a continuously stratified fluid over a uniform slope, and found interfacial mixing as a result of the wave breaking and energy dissipation as a result of the bottom viscous. They divided the wave categories into the subcritical and supercritical cases that depend upon the ratio of the bottom slope to the wave-characteristic slope. To investigate the evolution and breaking of an internal wave as it shoals on a sloping bottom connecting the deeper region, Kao et al. (1985) measured the fluid velocity during the passage of internal waves by using hot-film anemometers at some fixed locations at the undisturbed pycnocline, and the instantaneous velocity profile by using a hydrogen-bubble wiring system consisting of platinum wire, high-intensity light source, and slit-light box. They found that the major energy was dissipated over the slope, but the remainder was transmitted onto the shelf or reflected back to the deep-water region. Wallace and Wilkinson (1988) experimentally resolved the internal-wave structure of the breaking process by using conductivity probes from which the density field could be evaluated, and

investigated the shoaling, mixing, and run-up using various visualization techniques, which include fraction screen, dye injection, and particle tracking methods. Helfrich (1992) observed the interaction of an internal wave of depression with a sloping bottom using micro-scale conductivity temperature probes, and recognized the importance of the backflow that produces significant mixing. Sideview photographs and video recordings of shadowgraphs and dye movement were also used to obtain quantitative information on the kinematics of breaking and run-up. De Silva et al. (1997) investigated the temporal and spatial density and velocity, boundary layer extent, turbulence, mixing, and intrusion owing to the internal wave breaking on a sloping bed by employing three different flow visualization methods, namely a rainbow color schlieren method, a digital particle tracking method, and a dye visualization method. The mechanism of internal waves in a two-layer system comprising homogeneous fluids of slightly different densities has been studied since the work of Umeyama (2002), who used a digital video camera to illustrate the internal waves propagating in a fluid of finite depth over a flat bed. After analyzing continuous photos, the temporal and spatial variations of the density interface were obtained from a set of luminance values in the upper and lower layers, in which the water was visualized by adding a blue dye. To observe the runup and breaking of internal waves over a uniform slope, Umeyama and Shintani (2004) installed a Plexiglas plate in a wave tank and measured the profile of internal waves and the mixing between two layers. Later, Umeyama and Shintani (2006) performed more precise laboratory tests by considering additional aspects, such as transformation, attenuation, set-down, and setup during shoaling and breaking events.

Visualization techniques with lasers have played an essential role in fluid flows since the late 1970s because they yield both qualitative and quantitative insights in fluid mechanics. The developments in particle image velocimetry (PIV) and particle tracking velocimetry (PTV) have led to the visualization of fluid velocity. The two methods have used different evaluation techniques to extract velocity vectors from the images. Especially, the progress of PIV in last decades was huge in its capability of resolving spatial and temporal quantities and wide in its area of the application. The PIV technique is now a standard measurement tool for the quantification of the velocity field in fluid mechanics. In contrast, PTV has been developed to measure a sufficient number of velocity vectors with meaningful accuracy. Both techniques are analysis methods for image pairs taken in a seeded flow field with known temporal separation. Michallet and Ivey (1999) measured water velocities due to the shoaling and breaking of internal solitary waves on uniform slopes using PIV. The velocity field was calculated with two consecutive frames by cross-correlation method (Stevens and Coates 1994). Grue et al. (1999) investigated solitary waves propagating in a two-layer fluid by using both PIV and PTV. Shimizu et al. (2005) employed a PIV system consisting of a Nd:YAG pulsed laser and CCD camera and got precise features of velocity field along a slope during the pass of internal waves. Umeyama and Shinomiya (2009) developed a new

PIV system that utilized halogen lamps and three high-definition digital video cameras to expand the field of view. The velocity field was measured under realistic laboratory conditions, and the experimental velocity distributions were compared with the corresponding results by the third-order Stokes internal-wave theory. These attempts proved that the PIV technique enables the measurement of water velocity spatially induced by the nonlinear internal waves with considerable accuracy. Umeyama and Matsuki (2011) recently measured the similar physical quantities with two frequency-doubled Nd:YAG lasers of 50 mW. The PIV method was applied to trace water particle path, and the measured trajectory was compared with the particle positions theoretically obtained by integrating the Eulerian velocity to a higher order in a Taylor series expansion. In addition, the knowledge was extended to analyze mass transport velocity in a shallow-water region.

1.1.4 Numerical investigations of internal waves

Numerical models have also been used to investigate the characteristics of internal waves. Bogucki and Garrett (1993) studied shear-induced decay of an internal solitary wave and thickening of the interface between the two layers. In their study, the overview of theoretical models and formulae for damping rate are discussed. Cummins (2000) investigated the importance of flow separation in the lee of the sill at Knight Inlet with a two-dimensional version of the Princeton Ocean Model (POM). Afanasyev and Peltier (2001) applied their numerical model to study breaking internal waves over the sill in Knight Inlet. The model is nonhydrostatic, but it applies a slip bottom boundary condition, and hence it does not allow for bottom boundary separation. Their main conclusion is that it is the breaking of a forced stationary internal wave, resulting in irreversible mixing, that creates the body of well-mixed fluid in the lee of the sill. Vlasenko and Hutter (2002) used a numerical model to investigate the breaking and criterion for breaking of solitary internal waves over a slope. Legg and Adcroft (2003) applied the MITgcm to study the interactions of internal waves with both concave and convex slopes. The critical slope angle and importance of nonhydrostatic pressure were discussed. Fringer and Street (2003) performed two- and three-dimensional numerical simulations to study interfacial waves in a periodic domain by imposing a source term in a horizontal momentum equation. In their work, the effects of interface thickness on dissipation and mixing were also considered. Haidvogel (2005) used hydrostatic Spectral Element Ocean Model to simulate waves created at a coastal canyon. His results were in good agreement with with measurements from a rotating tank. Davies and Xing (2005) studied with a two-dimensional cross coast model near inertial internal waves that are wind generated. Smyth et al. (2005) applied DNS to investigate differential diffusion in breaking Kelvin-Helmholtz billows. Katsumata (2006) used POM to study the internal tide generation and energy fluxes at a continental slope (outside Australia). He discussed two- and three-dimensional models of internal tide, and state that by using two-dimensional models the

energy fluxes may be underestimated. Venayagamoorthy and Fringer (2006) applied cross-sectional numerical models to compute nonhydrostatic and nonlinear contributions to energy fluxes up an incline with laboratory scale. Bourgault and Kelley (2007) study the reflectance of internal waves on a slope and relate two-dimensional slice model results to laboratory experiments described in Helfrich (1992) and Michallet and Ivey (1999). Umeyama and Shintani (2004, 2006) used the $k-\varepsilon$ model to explain the velocity and density field during runup events. Their numerical results were shown to be in good agreement with the experimental data. Shintani (2005) also applied the two-dimensional nonhydrostatic model to investigate the internal wave upwelling and breaking with fine resolutions. In recent years, the numerical modelling is a widely used methodology in investigation of internal waves for both laboratory experiments and ocean/lake. In this study, the two-dimensional nonhydrostatic model was applied to investigate the mass transport and internal wave kinematics in laboratory wave tank scale.

1.2. Literature reviews on investigations of mass transport by internal waves and problem statement

It is proven that internal waves have a significant impact on both fundamental processes and engineering applications. In the ocean, for example, internal waves play an important role in tidal dissipation, eventually affecting abyssal mixing. They are also of importance in engineering fields such as deep-water oil drilling, submarine technology, and acoustic communications (Mathur, 2011). Another noticeable effect of internal waves is the transport of floating particles, such as suspended sediment, nutrients, larvae, and contaminants. The examination of suspended particles, planktonic larval, post-larval invertebrate, and fish has been performed by several researches.

Cacchione and Southard (1974) performed the measurements of internal waves in a linearly stratified medium and suggested that shoaling internal waves are associated with the movement of bottom sediment along the continental shelf. The interaction of internal waves with sloping boundary generates strong horizontal flows that can cause transport of sediments near the bed (Cacchione et al., 2002). Stastna and Lamb (2008) discussed about the contribution of internal waves to the resuspension of sediments and the maintenance of sediment concentration in the water column. Hosegood and van Haren (2004) argue that internal waves may be the dominant mechanism driving on-shelf sediment fluxes. Therefore, special attention needs to be paid to the mass transport by internal waves along a sloping boundary to understand the shaping of the continental shelf.

In the offshore regions, internal waves contribute to the redistribution of suspended particles. Shanks (1983) proved that crab larvae could be transported shoreward by unbroken internal waves. Shanks (1987) showed that large-amplitude internal waves could be

considered when calculating the dispersion of an offshore oil spill off the coast of North Carolina. Leichter et al. (1998) showed that internal waves provide nutrients to benthic animals around the coral reefs off the coast of the Florida Keys. Leichter et al. (2003) presented field measurements that demonstrate the degree of correlation between the concentration of nutrients and the arrival of internal bores containing cool, deep, and nutrient rich water at Conch Reef, Florida Keys.

On coral reefs, temperature variability is important owing to physiological stresses in corals occurring at both high and low temperatures (Brown, 1997; Knowlton and Jackson, 2001) and because temperature shows strong inverse correlation with dissolved nutrient concentrations. Physical forcing associated with internal waves is known to occur both on other coral reefs (e.g., Wolanski and Pickard, 1983; Wolanski and Hamner, 1988; Wolanski and Delesalle, 1995; Wolanski and Deleersnijder, 1998) and in a wide variety of shallow water marine environments (e.g., Sanstrom and Elliott, 1984; Holloway, 1987; Pineda, 1991, 1994; MacKinnon and Gregg, 2003).

The onshore transport of contaminants is a serious health and economical concern that coastal communities face. Internal waves have also been shown to play a role in the transport of discharged pollutants across shore. Boehm et al. (2002) evaluated the potential for effluent transport via internal tides from the Orange County Sanitary District ocean water sewage outfall in the onshore direction toward Huntington Beach, CA, in which for several summers, high levels of fecal indicator bacteria were found, forcing the beach to be posted as unfit for swimming.

Although there were many field observations of mass transport in the ocean or lake, there is a little work in the theoretical mass transport, particularly in the development of accurate models for transport via internal waves in near-shore environments (Huthnance, 1989). Dore (1970) was the first person who calculated the horizontal mass transport velocity for a progressive wave in a two-layer system with no net horizontal flow conditions. He found that the velocity at the interface is in the direction of wave propagation. Dore (1970, 1973) pointed out that the mass transport velocity in a two-layer system can be much greater than that in a one-layer system, such as the one included in the study conducted by Longuet–Higgins (1953).

Wunch (1971) investigated the mass transport due to internal waves propagating in a continuously stratified fluid. His study indicated that the mass transport is in the direction of wave propagation at the top and bottom of water column, while it is in the opposite direction of wave propagation in the middle of the water column. Later, Wen and Liu (1995) investigated mass transport with viscous damping, which was ignored by Dore (1970) and a trend of mass transport similar to that in the study conducted by Dore (1970) was found. They also found that viscous damping plays an important role in estimating mass transport

velocity. Tsuji and Nagata (1973) proposed a solution for mass transport due to internal waves propagating on the interface between two layers of infinite thickness. They concluded that mass transport appears in the direction of the wave propagation in both layers. It seems that the profile of mass transport strongly depends on the assumptions of stratification. The most popular assumption for investigating the mass transport due to internal waves is two-layer stratification, but how the ratio between thicknesses of these layers affects mass transport still remains a challenge.

Numerous studies related to mass transport owing to the internal wave propagation at density interface have been undertaken for two-layer and linearly stratified fluids. These stratified fluid systems are not so realistic as the ones that consist of two homogeneous layers (epilimnion and hypolimnion) separated by a diffusive interfacial layer (metalimnion). However, previous research failed to theoretically and experimentally investigate mass transport when internal waves propagate in this realistic stratification structure. In this study, particular focus is paid to the effect of transition layer on mass transport due to internal wave propagation over a flat bottom and constant slope.

In this thesis, three major problems are addressed. Answering these question helps in understanding the mechanism of internal wave propagation, kinetics, and mass transport from the offshore to onshore waters.

Problem 1: Characteristics of internal waves propagating over a constant slope

Problem 2: Mass transport due to internal waves along a slope and the effect of thickness ratio between upper and lower layers.

Problem 3: Effect of diffusive transition layer on mass transport by internal waves

To solve these problems, laboratory experiments were conducted for both flat bottom and constant slope with different methods such as Particle Image Velocimetry, light attenuation, and dye-streak methods. The numerical method was also applied to the laboratory wave-tank scale to quantify the physical quantities of internal waves that related to mass transport phenomena for different stratifications. A series of experimental and computation cases were performed to solve three above problems. The details of the cases were presented in the Appendix.

1.3. Thesis structure

This dissertation comprises seven chapters.

Chapter 1 gives a brief introduction to physical aspects of internal waves that propagate in the density-stratified fluid layers. It also includes the motivation and objective of this study.

Chapter 2 reviews previous studies of the internal wave kinematics that include interfacial displacement, celerity, water particle velocity, and trajectory. The theoretical background on mass transport in the presence of internal waves is also presented for different stratifications.

Chapter 3 experimentally investigates the behavior of internal waves propagating along a uniform slope. Experiments were performed in a wave tank having an overall length of 6.0 m and a cross section 0.15 m wide by 0.35 m deep. A slide-type wavemaker with a D-shaped wave paddle was placed at one end, and a Plexiglas plate with a slope 3 in 50, was fabricated between 1.0 and 6.0 m from the tip of the paddle. A density-stratified fluid consisting of fresh water and salt water with a density of 1,028 mg/cm^3 was prepared for a series of laboratory tests. The instantaneous water particle velocity in a wave motion was measured using a single-exposure PIV system that consists of a frequency-doubled Nd:YAG laser of 8-W energy at 532 nm, and two high-definition digital video cameras with a maximum resolution of 1920 × 1080 pixels. A cross-correlation method was performed to calculate the water particle displacement and local velocity in an Eulerian scheme by processing a pair of image frames. The PIV technique was applied to the computation of Lagrangian velocity and the prediction of Stokes drift. In addition to the PIV measurement, the spatial and temporal variations of the density interface, wave celerity, and mass transport due to shoaling and breaking of internal waves were obtained using two imaging techniques. The first method used light-attenuation to mark the vertical motions of isopycnal layers, and the second used dye-streak to visualize the water particle movement. Experiments were performed in the fluid having different thickness ratios between two layers for some different wave periods using the first method and in the fluid having a thin diffusive interfacial layer between two homogeneous layers.

Chapter 4 concerns a numerical approach that is applied for the experimental setup. The theoretical aspect of the problem was based on a two-dimensional numerical model. In formulating the model, the Boussinesq approximation was applied to the continuity and momentum equations. To solve these governing equations, an explicit finite difference technique with the fractional-step method was employed on staggered grids. The advective and diffusive terms were discretized using the ULTIMATE-QUICKET scheme and the central difference scheme, respectively, and velocity, trajectory, and interface were computed in the whole flume with spatial resolutions. After the accuracy of the numerical model was confirmed by verification studies using experimental data, it was applied to several test results for various hydraulic and geometric conditions.

Chapter 5 investigates the effect of the thickness ratio on mass transport due to propagation of internal waves. Because boundary conditions are essential in the limited wave tank, initially the case of a horizontal bottom is considered to point out the various existing approximations given in the different models. The mass transport velocity was estimated

from the horizontal excursion of water particle. The water particle trajectory computed by the nonhydrostatic model was compared with PIV results from the wave tank. It was confirmed that the numerical model reasonably reproduces the measured mass transport velocity of the internal waves in various bottom conditions. A series of numerical experiments showed the dependency of mass transport on the layer thickness ratio and internal wave height. The maximum mass transport velocity was highest when the thickness ratio of upper and lower layers was unity and became smaller when the lower layer thickness exceeded the upper-layer thickness. For all thickness ratios, the mass transport velocity increased with the internal wave height.

Chapter 6 is concerned with a few aspects of nonlinear internal waves in a fluid system of two homogeneous layers separated by a thin diffusive transition layer. First, the transport of water particles inside the interfacial layer and adjacent regions was investigated using a numerical model having very high resolution in the case of a flat bottom, and subsequently, the horizontal mass transport in the case of a uniform slope is discussed.

Chapter 7 presents the conclusions and recommendations of this investigation. Conclusions are given to remark the fulfillment of the present work to the objective. Recommendations are made for further considerations on investigation of mass transport in homogeneous layers with a diffusive layer.

Chapter 2

Previous Theoretical Studies of Internal Wave Kinematics and Mass Transport

2.1. Introduction

In this chapter, the basic theories of kinematics of internal waves and mass transport are presented. Stokes internal waves propagating along the interface between two homogeneous incompressible and inviscid fluids of different density in a constant depth are reviewed. For the surface waves, Stokes (1847) proved that the particles of fluid apart from their orbital motion with a steady second-order drift velocity (mass-transport velocity) using an assumption of a perfect, non-viscous fluid. However, the experiments later for the surface waves indicated that the drift of particles can be very different from results predicted by Stokes' theory. Longuet-Higgins (1953) took account of the viscosity to his solutions and developed a general theory of mass transport that was in better agreement with observation. The mass transport by internal waves did not get much interest as surface waves, because it is not easy to measure the transport of particle under the water surface. However, with recent development of measurement technique the reason has been solving. Following the Longuet-Higgins' approach for surface waves, Dore (1970) was the first person who calculated the horizontal mass transport velocity for a progressive wave in a two-layer system with no net horizontal flow conditions. Dore (1970, 1973) pointed out that the mass transport velocity in a two-layer system can be much greater than that in a one-layer system such as the one in the work by Longuet-Higgins (1953). The mass transport in a continuously stratified fluid was also considered by Wunch (1971). Following Phillips (1966) and Longuet-Higgins (1969), Wunch derived the formula to compute the distribution of mass transport velocity for both flat bottom and a constant slope cases. In this chapter, the foundations of resulting mass transport by water particle trajectory due to internal wave propagation for different stratifications are discussed. The discussion for the realistic stratification is also presented.

2.2. Internal wave kinematics

2.2.1 Linear internal wave theory

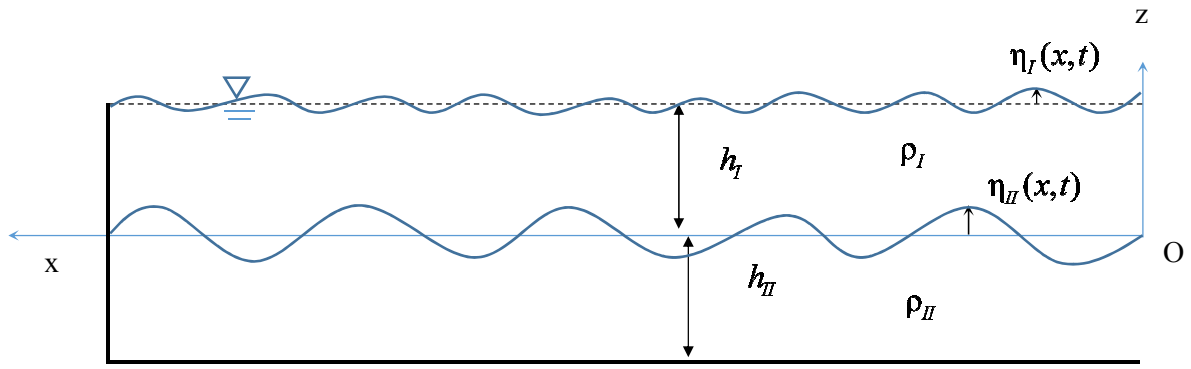

Fig. 2.1 Schematic of the definitions of variables

The origin of the axes is located in the undisturbed interface (**Fig. 2.1**). The density and depth of the upper layer are ρ_I and h_I, and those of the lower layer are ρ_{II} and h_{II}. The vertical displacements of the free surface and the density interface are $\eta_I(x,t)$ and $\eta_{II}(x,t)$. Let $\varphi_I(x,z,t)$, and $\varphi_{II}(x,z,t)$ denote the velocity potentials in the upper and lower layers, so that the Laplace equations are

$$\varphi_{Ixx}+\varphi_{Izz}=0 \tag{2.1}$$

$$\varphi_{IIxx}+\varphi_{IIzz}=0 \tag{2.2}$$

where x is the horizontal coordinate; and z is the vertical coordinate. The kinematical and dynamical boundary conditions at the free surface are

$$g(\eta_I+h_I)+\varphi_{It}+\frac{1}{2}(\varphi_{Ix}^2+\varphi_{Iz}^2)=0 \qquad \text{on } z=h_I+\eta_I \tag{2.3}$$

$$\eta_{It}+\eta_{Ix}\varphi_{Ix}-\varphi_{Iz}=0 \qquad \text{on } z=h_I+\eta_I \tag{2.4}$$

where g is the gravity acceleration; and t is time. The boundary conditions at the density interface are

$$\eta_{IIt}+\eta_{IIx}\varphi_{Ix}-\varphi_{Iz}=0 \qquad \text{on } z=\eta_{II} \tag{2.5}$$

$$\eta_{IIt}+\eta_{IIx}\varphi_{IIx}-\varphi_{IIz}=0 \qquad \text{on } z=\eta_{II} \tag{2.6}$$

$$\rho_I\{g\eta_{II}+\varphi_{It}+\frac{1}{2}(\varphi_{Ix}^2+\varphi_{Iz}^2)\}=\rho_{II}\{g\eta_{II}+\varphi_{IIt}+\frac{1}{2}(\varphi_{IIx}^2+\varphi_{IIz}^2)\} \qquad \text{on } z=\eta_{II} \tag{2.7}$$

The bottom boundary condition is

$$\varphi_{IIz} = 0 \qquad \text{on } z = -h_{II} \tag{2.8}$$

In the finite-amplitude wave theory, the perturbation method is used to solve the above basic equations and boundary conditions. These solutions have been obtained to the second order by Umeyama (1998), and to the third order by Umeyama (2000).

When the displacement of fluid interface is given by a linear profile such as $\eta_{II} = a\cos(kx - \sigma t)$, the horizontal and vertical velocity components for the water particle can be obtained from the velocity potentials where $u_I = -\partial\varphi_I / \partial x$, $w_I = -\partial\varphi_I / \partial z$, $u_{II} = -\partial\varphi_{II} / \partial x$, and $w_{II} = -\partial\varphi_{II} / \partial z$. Therefore, the velocity components in both layers are expressed as

$$u_I = \frac{ak}{\sigma}(\alpha\cosh kz - \frac{\sigma^2}{k}\sinh kz)\cos(kx - \sigma t) \tag{2.9}$$

$$w_I = -\frac{ak}{\sigma}(\alpha\sinh kz - \frac{\sigma^2}{k}\cosh kz)\sin(kx - \sigma t) \tag{2.10}$$

$$u_{II} = -\frac{a\sigma}{\sinh kh_{II}}\cosh k(z + h_{II})\cos(kx - \sigma t) \tag{2.11}$$

$$w_{II} = \frac{a\sigma}{\sinh kh_{II}}\sinh k(z + h_{II})\sin(kx - \sigma t) \tag{2.12}$$

where a is internal wave amplitude; k is wave number; and α is a constant that is given by

$$\alpha = \frac{\rho_{II} - \rho_I}{\rho_I}g - \frac{\rho_{II}}{\rho_I}\frac{\sigma^2}{k}\coth kh_{II}$$

The dispersion relation may be written as

$$\sigma^4(\coth kh_I \coth kh_{II} + \frac{\rho_I}{\rho_{II}}) - \sigma^2(\coth kh_I + \coth kh_{II})gk + \frac{\rho_{II} - \rho_I}{\rho_I}(gk)^2 = 0 \tag{2.13}$$

Solving Eq. (2.13) for $C = \sigma / k$ and assuming $\rho_{II} \approx \rho_I$, it becomes

$$C = \sqrt{\frac{\rho_{II} - \rho_I}{\rho_I}\frac{g}{k(\coth kh_I + \coth kh_{II})}} \approx \varepsilon_g\sqrt{\frac{(\eta_{II} + h_{II})h_I}{(\eta_{II} + h_I + h_{II})}} \tag{2.14}$$

where $\varepsilon_g = \sqrt{\frac{\rho_{II} - \rho_I}{\rho_I}g}$. Thus the group velocity for internal waves is given by

$$C_g = \frac{C}{2}\left(1+\frac{\dfrac{kh_I}{\sinh^2 kh_I}+\dfrac{kh_{II}}{\sinh^2 kh_{II}}}{\coth kh_I+\coth kh_{II}}\right) \tag{2.15}$$

2.2.2 *The method of characteristics for long internal waves on a slope*

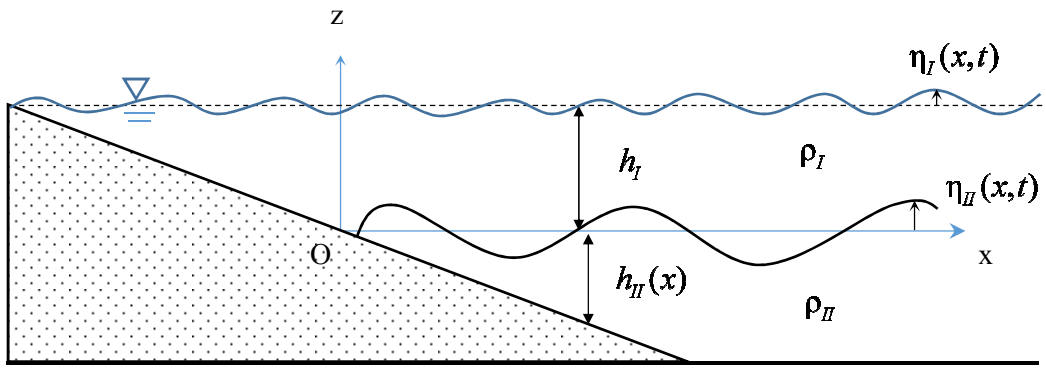

Fig. 2.2 Schematic of the definitions of variables on a slopping boundary

Umeyama and Shintani (2004) investigated the runup of internal waves on a plane impermeable slope. A reliable solution for the displacement of the density interface and the horizontal velocity of the internal waves was derived by means of the method of characteristics. Let $u_{II}(x,z,t)$ denotes the horizontal velocity for long internal waves so that the governing equations are

$$2(1+\frac{\eta_{II}+h_{II}}{h_I})C_t + u_{IIx}C + 2(1+\frac{\eta_{II}+h_{II}}{h_I})C_x = 0 \tag{2.16}$$

$$u_{IIt} + u_{II}u_{IIx} + 2(1+\frac{\eta_{II}+h_{II}}{h_I})^2 CC_x = g\frac{\rho_{II}-\rho_I}{\rho_{II}}h_{IIx} \tag{2.17}$$

It is convenient to define the lower-layer thickness for a uniform slope as

$$h_{II} = h_{II}(x) = m\frac{\rho_I}{g(\rho_{II}-\rho_I)}x$$

where m = constant. By adding and subtracting Eqs. (2.16) and (2.17), and assuming $\eta + h_{II} << h_I$, the results can be written in the familiar form:

$$[\frac{\partial}{\partial t}+(u_{II}\pm C)\frac{\partial}{\partial x}](u_{II}\pm 2C - mt) = 0 \tag{2.18}$$

Use of the method of characteristics will make it possible to describe η_{II} and u_{II} such as

$$\eta_{II} = -\frac{A^2}{2}\frac{h_I + sx}{h_I sx}[J_1(X)\cos T + \{J_0(X) - \frac{J_1(X)}{X}\}\sin T]^2 + A\{J_0(X)\sin T + J_1(X)\cos T\} \tag{2.19}$$

$$u_{II} = A\varepsilon_g\sqrt{\frac{h_I + sx}{h_I sx}}[J_1(X)\cos T + \{J_0(X) - \frac{J_1(X)}{X}\}\sin T] \tag{2.20}$$

where A = constant; and J_p = the Bessel function of order p. The dependent variables are given by

$$X = \frac{2\sigma}{s\varepsilon_g}\sqrt{\frac{h_I sx}{h_I + sx}} \text{ , and } T = -\sigma t$$

For convenience, the dependent variable X will not be shown hereafter.

A displacement of the interface will cause an associated surface displacement (Umeyama et al., 2011). In the upper layer, the linearized momentum equation may be simply given by

$$\frac{\partial u_I}{\partial t} = -g\frac{\partial \eta_I}{\partial x} \tag{2.21}$$

The continuity equation can be determined in the same manner:

$$u_I = \frac{C(\eta_I - \eta_{II})}{h_I + (\eta_I - \eta_{II})} \approx -\frac{C}{h_I}\eta_{II} \tag{2.22}$$

Combining Eqs. (2.21) and (2.22), the following differential results:

$$\eta_I = -\frac{A^2\sigma C}{g}\int\frac{h_I + sx}{h_I^2 sx}[J_1\sin T - \{J_0 - \frac{J_1}{X}\}\cos T][J_1\cos T + \{J_0 - \frac{J_1}{X}\}\sin T]dt - \frac{A\sigma C}{gh_I}\int\{J_0\cos T - J_1\sin T\}dt \tag{2.23}$$

2.3. Mass transport

2.3.1 Stokes drift due to water waves in a single-layer fluid

For a pure wave motion in fluid dynamics, the Stokes drift velocity is the average velocity when following a specific fluid parcel as it travels with the fluid flow. For instance, a particle floating at the free surface of water waves, experiences a net Stokes drift velocity in the direction of wave propagation. More generally, the Stokes drift velocity is the difference between the average Lagrangian flow velocity of a fluid parcel, and the average Eulerian flow velocity of the fluid at a fixed position. This nonlinear phenomenon is named after

George Gabriel Stokes, who derived expressions for this drift in his 1847 study of water waves.

First, the mass transport in a single layer (**Fig. 2.3**) is discussed. If the equation of the free surface is

$$z = ae^{i(kx-\sigma t)} + \mathrm{O}(a^2 k) \tag{2.24}$$

then Stokes' expression for the mass transport velocity U_S

$$U_S(z) = \frac{a^2 \sigma k \cosh 2k(z-h)}{2\sinh^2 kh} + C \tag{2.25}$$

In deep water ($kh >> 1$)

$$U_S = a^2 \sigma k e^{-2kz} \tag{2.26}$$

where t is the time; a is the wave amplitude; $k = 2\pi/L$ is wave number; L is wave length; T is wave period; $\sigma = \frac{2\pi}{T}$ is wave frequency; h is the depth; and C is an arbitrary constant.

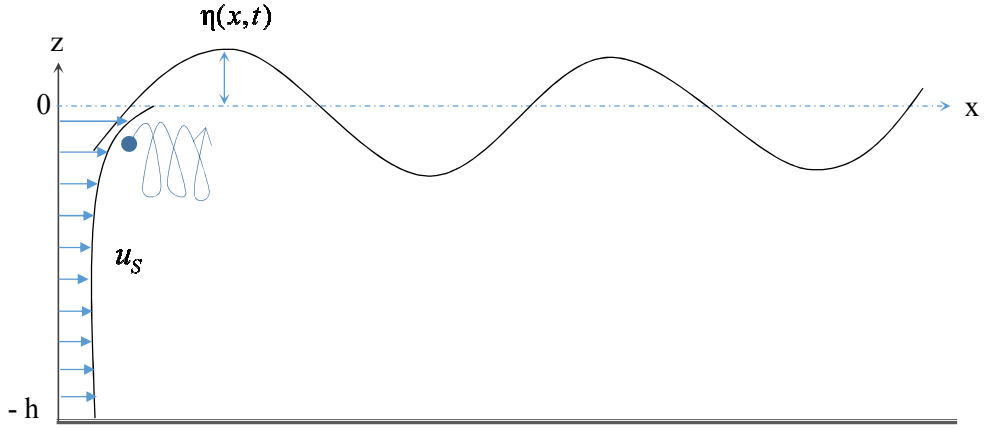

Fig. 2.3 Sketch of waves in a one-layer fluid

2.3.2 *Mass transport due to water waves in a two-layer density stratified fluid*

Dore (1970) applied the method of matched asymptotic expansions to consider about mass transport in a two-layered fluid system. The method of analysis involves a double expansion in powers of two-small parameters associated with wave amplitude and fluid viscosities together with notions of boundary-layer theory. Consider about two homogeneous incompressible fluids with Cartersian co-ordinates (x,z) as shown in **Fig. 2.1**; u, w, p, ρ, and υ are horizontal, vertical fluid velocities, change in pressure from the equilibrium state, density and kinematic viscosity, respectively. The equations of laminar motion for either fluid are

$$\frac{\partial q}{\partial t} + (q.\nabla) q = -\frac{1}{\rho}\nabla\rho + \upsilon\nabla^2 q \tag{2.27}$$

where $q = (u, w)$. If ψ is stream function:

$$u = \frac{\partial\psi}{\partial z},\ w = \frac{\partial\psi}{\partial x}$$

Then (2.8) will become:

$$\left(\frac{\partial}{\partial t} + \frac{\partial\psi}{\partial z}\frac{\partial}{\partial x} - \frac{\partial\psi}{\partial x}\frac{\partial}{\partial z}\right)\nabla^2\psi = \upsilon\nabla^4\psi \tag{2.28}$$

The method of matched asymptotic expansions is employed to calculate the mass transport velocity due to small amplitude oscillatory waves. According to Longuet-Higgins (1953), the mass transport velocity is

$$U_l = \overline{u_{II}} + \overline{\int^t u_I dt \frac{\partial u_I}{\partial x} + \int^t w_I dt \frac{\partial u_I}{\partial z}} \tag{2.29}$$

Dore (1970) successfully derived equation for the mass transport velocity of fluid bounded by horizontal planes.

$$U_l = \alpha^2\varepsilon^{-1} D e^{i(k-k^*)x} \tag{2.30}$$

where α is an ordering parameter which based on the ratio of wave amplitude to wave length, $\varepsilon = \left(\frac{\upsilon k_0^2}{\sigma}\right)^{1/2}$ is the inverse wave Reynolds number, σ is the real angular frequency of oscillation, k is the complex wave number, k^* is the complex conjugate of k, k_0 is the wave-number according to the inviscid theory of waves of infinitesimal amplitude, and D is a parameter that can compute from density and wave's parameters. The details of D can be referred in Dore (1970).

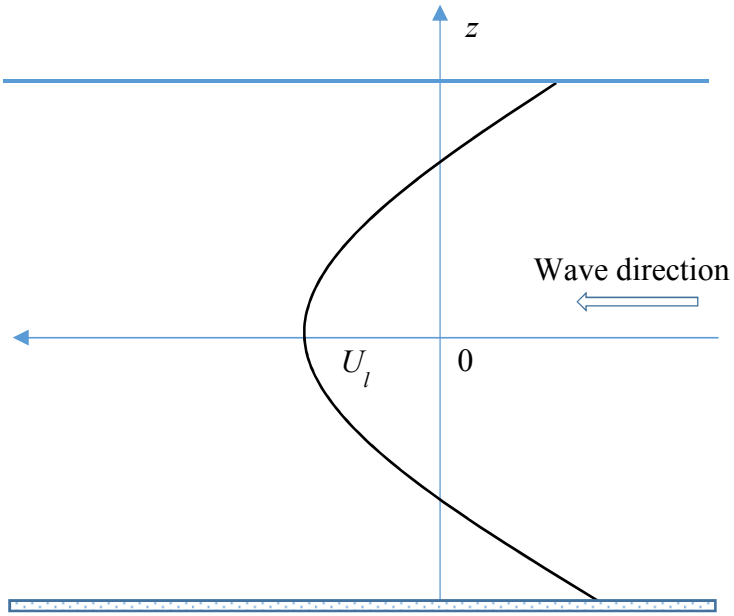

Fig. 2.4 Sketch of profile of horizontal mass transport velocity in a progressive wave for a two-layer fluid system bounded by two rigid horizontal planes.

The profile of horizontal mass transport velocity for a two-layer fluid system is plotted in **Fig. 2.4**. According to Dore (1970), at the bottom and surface boundaries mass transport velocity vanishes. In the interior of lower fluid, mass transport velocity has the parabolic distribution with a stationary value:

+ Minimum: $U_l = -\frac{1}{3}U_{li}$ at $z = -\frac{2}{3}h_I$

+ Vanished ($U_l = 0$) at $z = -\frac{1}{3}h_I$

+ $U_l = U_{li} \geq 0$ at the edge of the interfacial layer. U_{li} is the mass transport velocity at the interface.

It should be noted that the mass transport velocity is the greatest at the interface and it is in the direction of the wave propagation for all possible values at the physical quantities involved. The profile of mass transport velocity in the upper layer fluid is similar in form to that in the lower fluid.

2.3.3 Mass transport due to internal waves in a continuously stratified fluid over a flat bottom

Consider a channel with depth d , constant Brunt frequency N with internal wave propagating in a Boussinesq fluid. The top and bottom boundaries are rigid. u and w are the horizontal and vertical components of velocity, respectively. ω is the wave frequency. ψ is the stream function

$$u = -\frac{\partial \psi}{\partial z} \tag{2.31}$$

$$w = -\frac{\partial \psi}{\partial x} \tag{2.32}$$

Eqs. (2.36) and (2.37) must be satisfied the linear equation governing internal wave propagation

$$\frac{\partial^2 \psi}{\partial x^2} - \frac{1}{c^2}\frac{\partial^2 \psi}{\partial z^2} = 0 \tag{2.33}$$

where

$$c^2 = \frac{\omega^2}{N^2 - \omega^2} \tag{2.34}$$

The solution of Eq. (2.38) is

$$\psi = \sin\frac{n\pi z}{d}\cos\left(\frac{n\pi}{d}cx + \omega t\right) \tag{2.35}$$

The Lagrangian velocity is defined for infinitesimal waves as

$$\overrightarrow{u_L} = \overrightarrow{u_E} + \overrightarrow{u_S} \tag{2.36}$$

or $$\overrightarrow{u_L}(\vec{a},t) = \overrightarrow{u_E}(\vec{a},t) + (\int \overrightarrow{u_E}(\vec{a},t')dt')\nabla_a \overrightarrow{u_E}(\vec{a},t) \tag{2.37}$$

According to Wunch (1971)

$$\left\langle \overrightarrow{u_L} \right\rangle = \left\langle \overrightarrow{u_S} \right\rangle = -\left(\frac{n\pi c}{d}\right)^3 \frac{1}{2\omega c^3}\cos\frac{2n\pi z}{d} \tag{2.38}$$

$$\left\langle W_L \right\rangle = 0 \tag{2.39}$$

where u_L and u_S are Lagrangian and Stokes velocities, $\vec{a}$ is the Lagrangian initial position tag. The angle brackets denote a time averages.

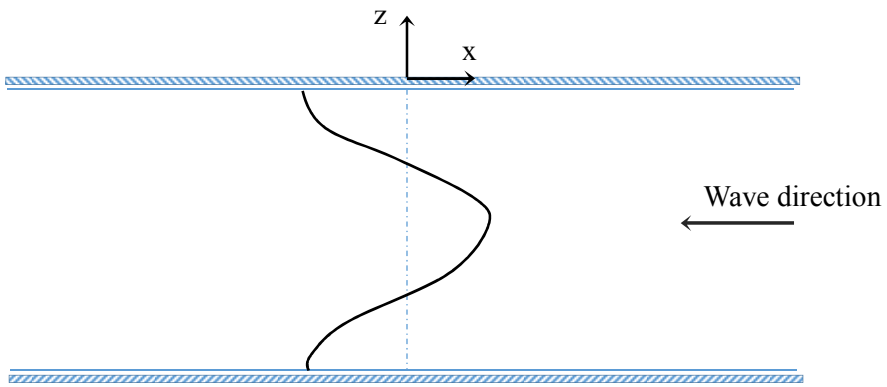

Fig. 2.5 Sketch of mean Lagrangian drift velocity for the fundamental channel mode n = 1

From Wunsch (1971)'s approach, the mean Lagrangian drift velocity can be estimated as plotted in **Fig. 2.5**. It is noted that the internal waves carry no net mass transport. The mass is transported in the wave propagation direction near the bottom and surface boundaries while is in the opposite direction in the middle of water column. It means the directions of mass transport are opposed to those for the two-layer fluid obtained by Dore (1970).

2.4. Discussion

This chapter presents a basic background of mass transport by internal waves in density stratified fluid. The ideas for estimating mass transport velocity of surface waves by Stokes (1847) and Longuet-Higgins (1953, 1969) have been adapted by Dore (1970) and Wunch (1971) for internal waves. For a two-layer fluid, the most noticeable conclusion by Dore (1970) is that the horizontal mass transport at the interface is in the direction of wave propagation, whereas near the surface and bottom boundaries, it opposes the direction of wave propagation (**Fig. 2.4**). For the continuously stratified fluid, the mass transport is in the direction of wave propagation at the top and bottom of water column and in the direction opposite to that of wave propagation in the middle of water column (Wunch 1971). This tendency of mass transport had been reported by Thorpe (1968) using dye-streak method and recently confirmed by numerical method of Gil and Fringer (2011). However, these assumptions of stratified fluid seem to be not suitable to investigate the mass transport in the body of coastal water, especially in shallow water regions. There exists a transition layer that separates the upper well-mixed water layer and lower stable and denser water layer. In ocean and lake, this layer is considered as pycnocline, which usually ranges from tens to hundreds of meters. In this layer, light objects such as larvae or fine sediments can stay without sinking into the heavy lower layer. The dissolved oxygen or nutrients are normally discontinuous through this layer. For such type of stratified fluid, the remaining question is manner of the mass transport because it is the intersection of two theories for two-layer homogeneous fluid in two layers and continuously stratified fluid in the transition layer. Al-Zanaidi and Dore (1976) investigated the Stokes' drift due to the first internal mode propagating along a thin and thick thermocline in a stratified fluid. They argued that Stokes' drift is in the direction opposite to that of the wave propagation within the thermocline and in the same direction as that of the wave propagation near the top and bottom boundaries. Turner (1980) suggested that backflow at mid-depth is expected in a fluid system that includes a diffuse interface separating two homogeneous layers. Therefore, in this thesis, the mass transport will be investigated with the consideration of thickness of diffusive interfacial layer. **Fig. 2.6** shows the schematic sketch of mass transport velocity profile for different stratification conditions. A diagnosed profile has been proposed for a water column that consists of a diffuse interface separating two homogeneous layers. The profile of mass transport velocity in the realistic stratification should be reflected in the characteristics of transport in both two-layer and continuously stratified fluids. It means that the mass in the homogeneous layers is transported in the direction opposite to that of wave propagation near the bottom and surface boundaries and inside the diffusive transition layer, while it is transported in the same direction as those of the parts near the interfacial layer (**Fig. 2.6**). The distribution of mass transport with effect of interfacial layer is further numerically and experimentally investigated in Chapter 6.

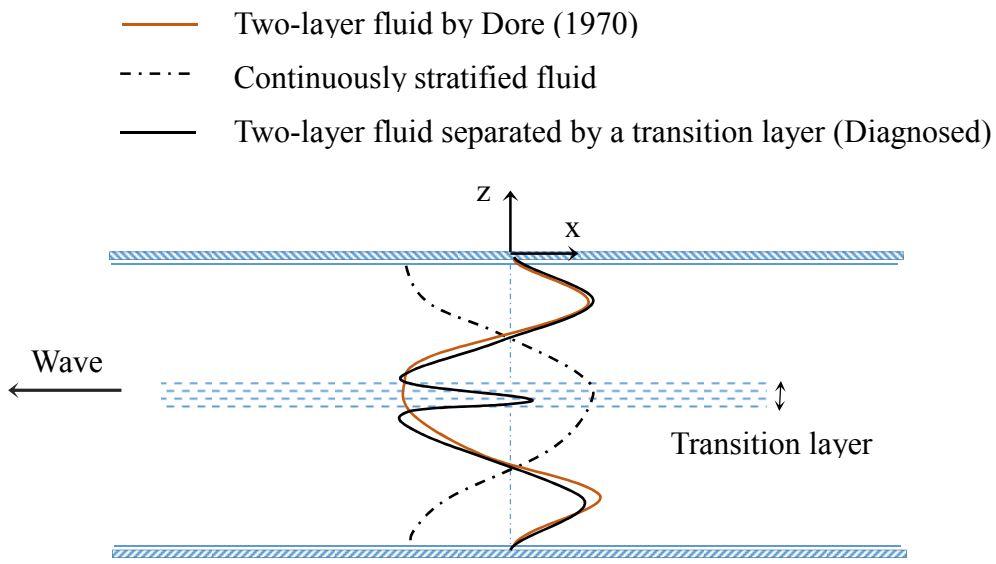

Fig. 2.6 Schematic sketch of mass-transport velocity for different stratified fluids

Chapter 3

Experimental Arrangements and Methods

Abstract

This chapter presents the experimental arrangements and processing techniques to investigate kinematics of internal waves and resulting mass transport by internal waves propagating over a sloping bottom in a two-layer stratified water. The setup for particle image velocimetry method to measure velocity fields is presented. The light attenuation method and dye-streak method are also described. A technique to transfer the velocity in Eulerian grids into Lagrangian velocity is presented. Therefore, the particle velocity and trajectory can be estimated due to the shoaling of internal waves. The distributions of particle velocities and trajectories have been investigated for different layer thickness ratios and wave periods. Experimental results for the kinematics of internal waves that propagate over a gentle slope in a two-layer stratified density fluid are also described in this chapter.

3.1. Experiments

3.1.1 Experimental setup

In this thesis, all experiments were conducted in the same wave tank, having an overall length of 600 cm and a cross section 15-cm wide by 35-cm deep. It was constructed of 12 Plexiglas panels, 10 stainless flanges, and a stainless bottom (**Fig. 3.1**). Each glass panel was 92-cm long and 27-cm high. A slide-type wave generator with a D-shaped wave paddle (**Fig. 3.2**) was placed at one end. A 1-cm-thick Plexiglas plate, which served as the plane seabed with a slope 3 in 50, was fabricated between 100 and 600 cm from the wavemaker.

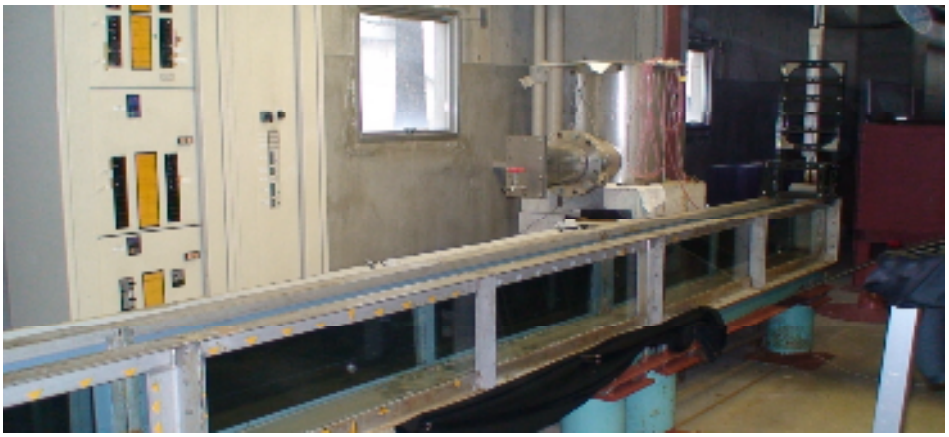

Fig. 3.1 A schematic diagram of experimental arrangements and a photograph of wave tank

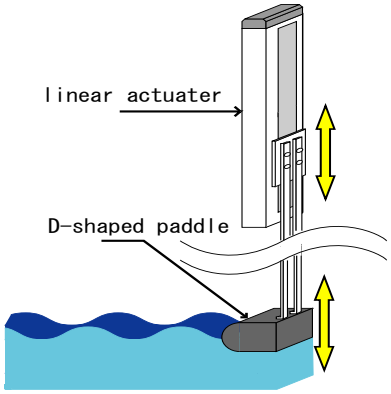

Fig. 3.2 A slide-type wavemaker with a D-shaped paddle

Because the temperature was not changed during the running time, the density depends only on the salinity concentration. A density-stratified fluid consisting of fresh water in the upper layer and salt water in the lower layer was prepared for a series of experiments. The densities of the fresh and salt water were 998 mg/cm^3 and 1,028 mg/cm^3, respectively. The water depth was kept at 30 cm during all experiments. The upper and lower thicknesses in the toe of slope were h_I and h_{II}, respectively.

Interfacial displacement was measured by an internal wave gauge (KENEK, LC-101) located at x = 100 cm from the wavemaker. The internal gauge has a conductivity sensor at the tip of a rod to distinguish the density interface. The rod was controlled by an electric servomotor with the feedback from the sensor. Accordingly, the rod moves vertically keeping the position of the sensor at the density interface. A data recorder (KEYENCE, NR-2000) was used to digitally record the displacement of the sensor.

3.1.2 Particle Image Velocimetry (PIV) method

PIV is a technique measuring an instantaneous velocity field using the sequential digital images. The development of PIV was well described in a comprehensive review article of Adrian (1991). The basic principle of PIV is evaluating the instantaneous velocities through recording the position of images of small tracers, suspended in the fluid, at successive instants in time. In practice, when two successive images of tracers illuminated in a thin and intense light sheet are acquired, the velocity is calculated from the known time difference and measured displacement. The analysis of the displacement of images in each interrogation window by means of the cross-correlation method leads to an estimated average displacement of particles.

To apply the PIV method, the two-layer density stratified fluid system was generated in the wavetank. To capture the high-contrast images with the particle tracer in both layers, DIAION (DK-FINE HP20SS) consisting of ion-exchange resin with the homogeneous matrix structure inside the particle was used. This type of matrix gave micropores formed by the polymeric networks, so that water could pass through these pores. Before generating the stratification for PIV experiment, DIAION was mixed in the salt water and fresh water. The saline water is first introduced into the wave tank having a thickness of up to h_{II} (cm). Then, the fresh water is very slowly filled in the wave tank using two diffuse plates as shown in **Fig. 3.3**.

In this study, the water particle velocity was measured using a single exposure image PIV system. The instantaneous particle velocity was measured through the 91.0-cm long, 27.0-cm high, and 1.0-cm thick glass panel using a frequency-doubled Nd:YAG laser of 8-W energy at 532 nm. A 2-mm thick light sheet was emitted from the upper side; this light sheet had a very uniform intensity and covered the total area of the glass panel. The system included two high-definition digital video cameras (SONY HXR-NX5J) with a maximum resolution of 1920 × 1080 pixels. The video camera was arranged from the sidewall of the wave tank. The camera image area was centered in the light sheet.

Following Umeyama et al. (2012), the analysis of the displacement of images in each interrogation window by means of the cross-correlation method leads to an estimated average displacement of particles (**Fig. 3.4**). The resolution is directly related to the size of the interrogation window. The displacement vector computed at any location is the spatially averaged transitional motion of particles. Vector fields could be obtained with the PIV system processing a pair of images, using an interrogation window of 64 × 64 pixels in a candidate region of 128 × 128 pixels. Because the internal wave topography does not significantly change over 0.1 s, the resultant displacement of topographic features for two images spaced in Δt = 0.1 s was chosen for a direct calculation of the velocity vectors.

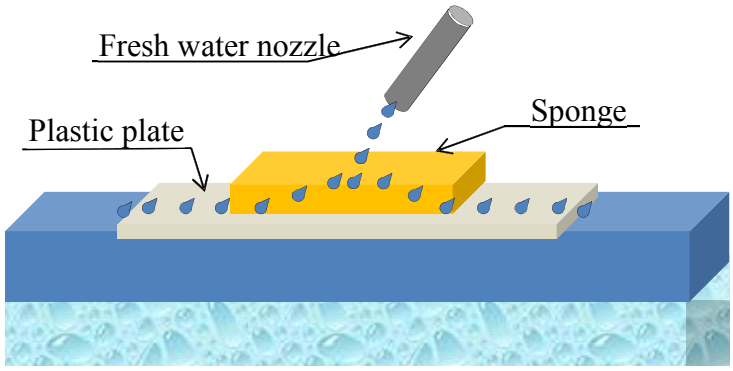

Fig. 3.3 Schematic diagram of floating diffuse plate to generate density stratification

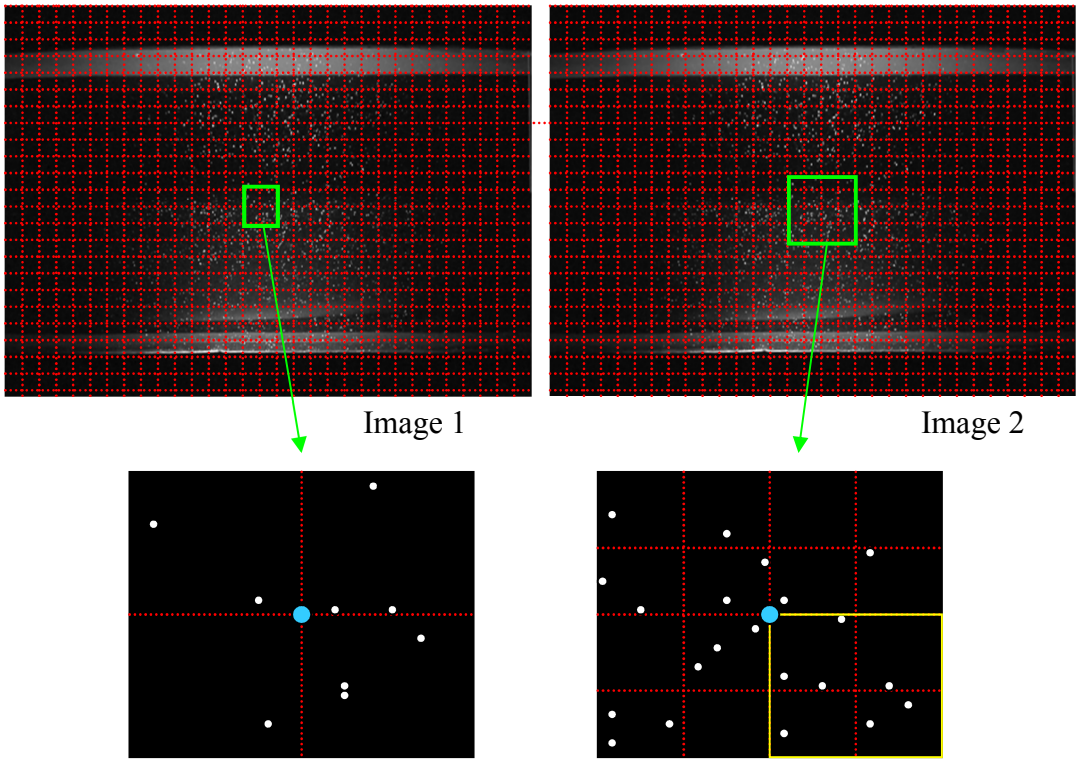

Fig. 3.4 Particle movement in images of different time

3.1.3 Light attenuation method

Using light attenuation method and image processing technique, the temporal and spatial variations of the density interface in the density-stratified two-layer fluid on a sloping bed can be measured. The objective of the method is to observe internal waves approaching

an upper slope in a wave tank using a video recording system, convert the measured data to the wave profile and celerity, and then compare the experimental values with theoretical ones.

In experiments, the stratification was generated using a method same as PIV. However, for application of this method, seeding particles were not used. Blue dye was added to the salt water to aid visualization of the density field before the fresh water was floated onto the salt water. The video recording system was modelled after that of Umeyama and Shintani (2004). It consisted of two video cameras (SONY HXR-NX5J), a white board, and a row of fluorescent lamps lying on the floor along the wave tank. The light from these lamps reflected on the white board and penetrated into the stratified water. These video cameras aimed at a front glass panel, and the video images were digitally recorded at 30 fps (frames per second).

Then, following Umeyama (2008), an image processing technique was used to illustrate the progressing profile of internal waves. The maximum resolution of the colour images was 1920 × 1080 pixels and the colour depth of files was 8 bits (**Fig. 3.5**). Each colour image file was transferred to an 8-bit (256 grades) grayscale image file. Using the method of image segmentation, individual pixels in a grayscale image were marked as object or background pixels. The threshold was obtained by creating a histogram of the image pixel intensities and calculating the valley point. The image was segmented into object and background pixels as

$$G_v = \begin{cases} 0 & if\,(C_v < T_r) \\ 255 & if\,(C_V \geq T_r) \end{cases} \tag{3.1}$$

where G_v = image value, C_v = grayscale value, and T_r = threshold. The processed data were saved to ASCII files and transformed to real scale. The density interface was estimated from the spatial distribution of the threshold.

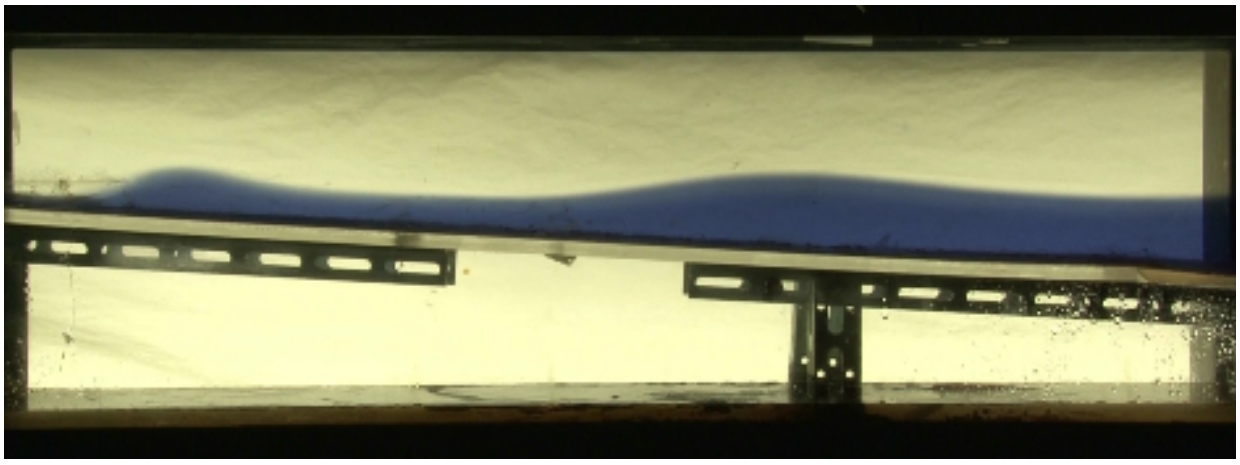

Fig. 3.5 Instantaneous view of wave propagation over a constant slope

3.1.4 Particle tracking technique

A cross-correlation method was performed to calculate the water particle displacement and local velocity by processing a pair of image frames. Although the representation of the velocity vector field in an Eulerian system is a typical example of the PIV method, the result can be applied to a particle tracking process in a Lagrangian system. Umeyama and Matsuki (2011) used the velocity given at the spatially discrete nodal point to estimate the imaginary velocity and location of a particle. The following explains the particle motion within a tracking time step Δt along an arbitrary trajectory across a general mesh of quadrilateral cells (**Fig. 3.6**). In general, the particle motion within a tracking time step Δt on a Eulerian grid could be estimated as following procedures:

(1) The nodal velocities in a Eulerian system were computed by PIV method.

(2) The particle velocity of a certain location was obtained by interpolating four velocities at neighboring nodal points, and

$$u = \frac{\frac{u_1}{l_1} + \frac{u_2}{l_2} + \frac{u_3}{l_3} + \frac{u_4}{l_4}}{\frac{1}{l_1} + \frac{1}{l_2} + \frac{1}{l_3} + \frac{1}{l_4}} \quad \text{at } t = t \tag{3.2}$$

and

$$u' = \frac{\frac{u'_1}{l'_1} + \frac{u'_2}{l'_2} + \frac{u'_3}{l'_3} + \frac{u'_4}{l'_4}}{\frac{1}{l'_1} + \frac{1}{l'_2} + \frac{1}{l'_3} + \frac{1}{l'_4}} \quad \text{at } t = t + \Delta t \tag{3.3}$$

where u_1, u_2, u_3, u_4 at $\mathrm{P}_1, \mathrm{P}_2, \mathrm{P}_3, \mathrm{P}_4$, respectively, where $\mathrm{P}_1, \mathrm{P}_2, \mathrm{P}_3$, and P_4 are corners of the mesh. $\mathrm{l}_1, \mathrm{l}_2, \mathrm{l}_3, \mathrm{l}_4, \mathrm{l}_1', \mathrm{l}_2', \mathrm{l}_3'$, and l_4' are distances to the imaginary location of a particle from the Eulerian grid points.

(3) A particle location was determined by translating the particle with the obtained particle velocity.

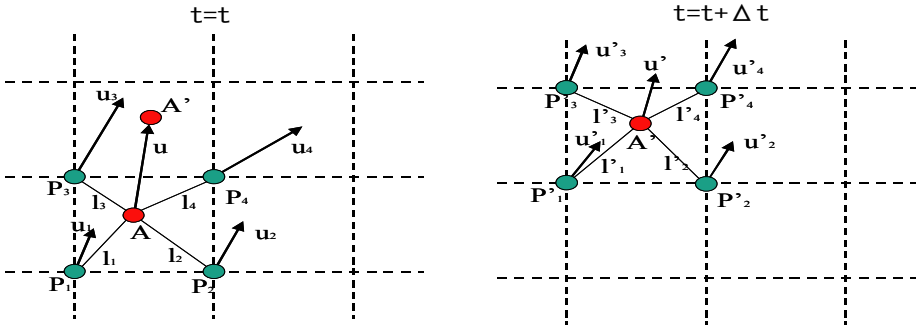

Fig. 3.6 Scheme of particle tracking

3.1.5 Dye-streak method

This method is usually used to visualize the horizontal displacement of water by observing the movements of dye streaks. Bagnold (1947) used this method to investigate mass transport for surface waves, which contributed to the excellent work of Longuet–Higgins (1953) in mass transport. Noda (1968) also used this method to study mass transport in boundary layers in standing waves. Thorpe (1968) applied a similar method to observe mass transport due to internal waves in a linearly stratified fluid.

The two-layer fluid is made with salt water of density 1,028 kg/m^3 which is overlain with fresh water. The water level is kept at 30 cm for all of experiments. The thicknesses of upper fresh water and lower salt water layers are equal. Experiments were conducted with different thicknesses of interfacial layer (d). To create the stratified fluid with a diffusive transition layer with desired thickness d (cm), the "two-tank" method (Hill, 2001) has been applied. This method uses two tanks of water in which one tank stored the salt water (T1) and connected with one fresh water tank (T2). Another big bucket of salt water (T3) uses the same bottom injection system to produce salt water to the wave flume. All of these valves are connected with a hose of 20-mm diameter (□). A mixer is used to mix salt water and fresh water in this tank. The system is joined to the flume through 12 bottom diffuser plates. The system is controlled with three valves: V1, V2, and V3 (**Fig. 3.7**). To easily visualize easily the interfacial layer, the salt water in the tank T1 has been colored with blue dye. The experiments will be performed using the following steps:

(a) Step 1: The fresh water is introduced with thickness of $h_I = 15 - d/2$ (cm) to the wave tank.

(b) Step 2: In this step, after filling the three tanks T1, T2, and T3 with the suitable amount of water, the valves V1 and V2 are opened, while the vale V3 is closed. The water from tanks T1 and T2 is gradually introduced into the bottom of wave tank via thin diffuser plates at the bottom. The mixer will help in creating a linear transition layer with blue color. After the process of filling transition layer finishes, the valve V2 has been closed.

(c) Step 3: Open the valve V3. The salt water is introduced into the wavetank from the bottom using the same bottom injection system. This step will finish when the thickness of lower layer reaches $h_{II} = 30 - d - h_I$ (cm).

Density profile can be obtained by measuring the vertical distribution of conductivity using an electrical conductivity (EC) meter. The EC meter is joined to a rod that is connected with a linear actuator. The linear actuator (EZ limo, EDR36D-K) was controlled by a sequence program from a PC. From the recorded conductivity, the distribution of salinity and density could be estimated with the vertical resolution of 2.0 mm. To maintain the desired thickness of transition layer between two homogeneous layers, water is selectively withdrawn

from the interfacial region prior to an experiment using small nozzles that are attached to a pump and positioned at the density interface. Water is then added through the bottom and top diffuser plates to compensate the fluid-layer depths.

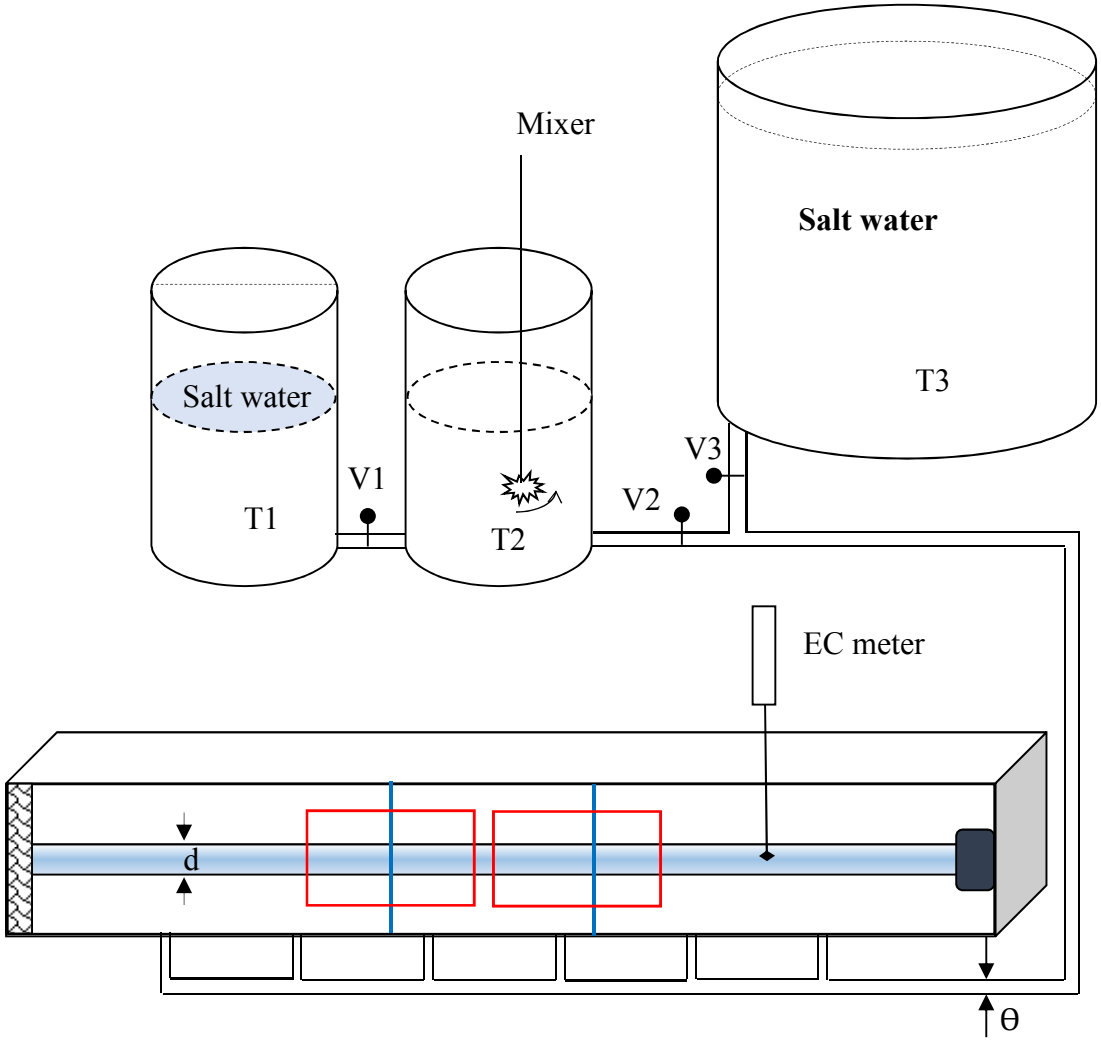

Fig. 3.7 Scheme of experimental setup for creating stratification

Before the wavemaker was started, several grains of dye were inserted into the water; these fell to the bottom, leaving nearly vertical streaks, which then gradually deformed, giving a direct picture of the velocity profile (**Fig. 3.8**). The movements of these dye streaks were recorded by two high-definition (HD) cameras (SONY HXR-NX5J), which were set at one side of the wavetank. In another side, a halogen light source covered by white diffuse paper sheet was positioned to support the viewing of the distortion of dye streaks. This method proved advantageous in that a series of water-particle displacements could be recorded in a single exposure because a conspicuous dye streak was produced every cycle.

The maximum displacement of water particles and its vertical profiles per cycle were measured from similar photographs.

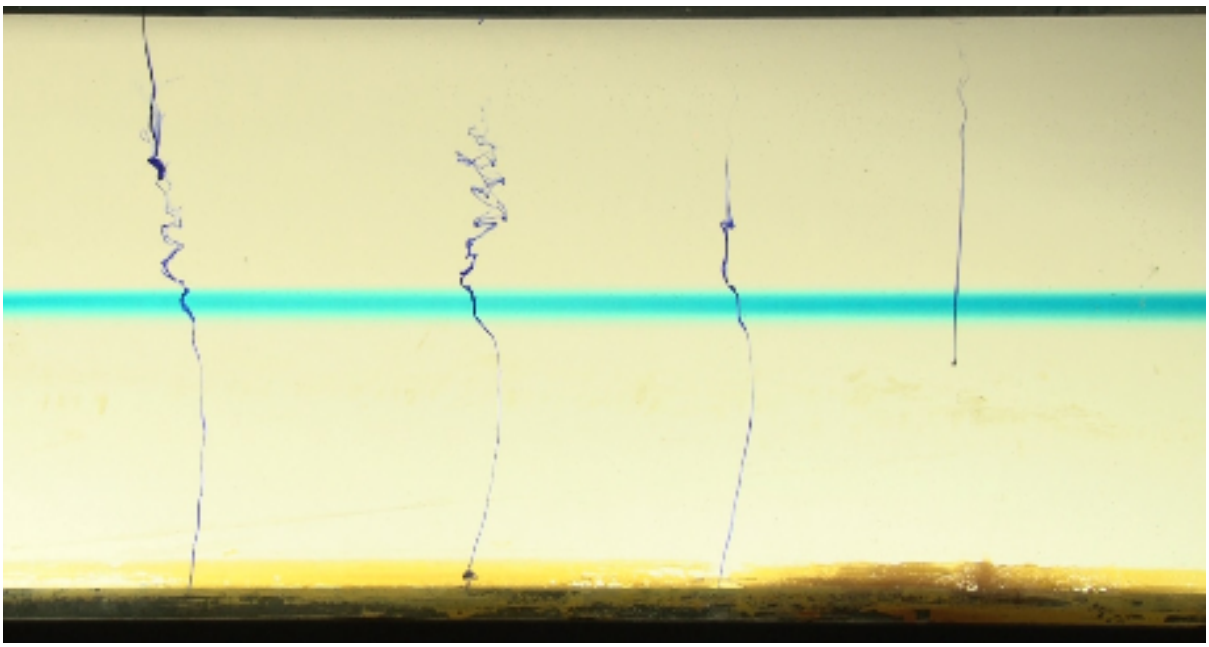

Fig. 3.8 Example image of sinking process of grains of dye from the water surface

3.2. Results

In this study, six experimental runs for internal waves propagating over a constant slope in the two-layer fluid system were performed (**Table 1**). Three thickness ratios between two layers were considered, having periods T = 5.2 s and 7.2 s. The details of coordinate system or parameters are depicted in **Fig. 3.9**. Consider the internal waves propagating over a uniform slope in a two-layer density-stratified fluid. The origin of the axes is set at the intersection between the undisturbed interface and the slope. In this chapter, the experimental results of Cases S1 and S2 are presented. The results of other cases will be presented and discussed in Chapter 4 in comparison with the computed results from numerical method.

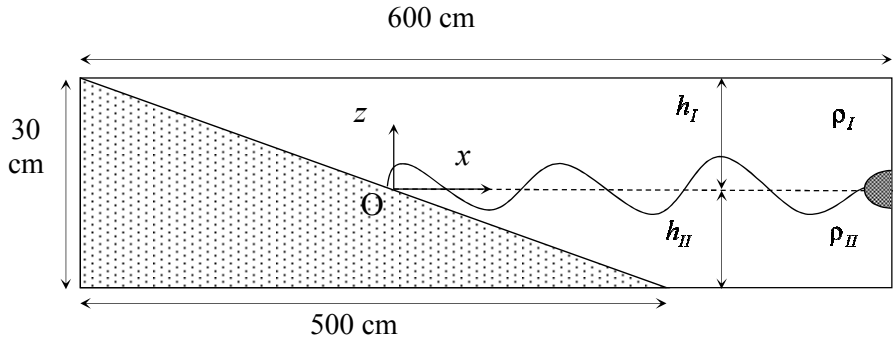

Fig. 3.9 Sketch of internal wave in the wave tank

3.2.1 Instantaneous velocity fields

The internal wave was generated from the wavemaker located in one side of wave tank. The wave height was measured at 100 cm from it by using a wave gauge. When a group of internal waves propagates shoreward, oscillatory water particle movements are induced in both upper and lower layers. **Fig. 3.10** shows the velocity vector fields due to such internal waves for Case S1. **Fig. 3.10** (a) and (b) depict velocity vector distributions from x = 20 cm to 110 cm and x = 120 cm to 195 cm, respectively. The measured instantaneous velocity fields were depicted for four different phase values of t/T=0, 0.25, 0.50, and 0.75. The abscissa and ordinate are the horizontal and vertical distances from the origin, respectively. Internal waves propagate from right to left, i.e., in the negative x direction. The corresponding wave height is H = 2.2 cm at x = 100 cm. **Fig. 3.10** (a) depicts the velocity fields for the measured region that is closer to the origin. The results show that the size of vortices gradually decreases when internal waves travel from offshore to inshore. The change of vortices involves the energy dissipation effect due to the instabilities and mixing during the runup event on a slope. As a result, vortices become thinner but velocities increase toward the upper slope. Inspecting the velocity in the region from x = 40 cm to 60 cm, it seems that the vortices change their shape from elliptic to round when they transfer cross this region. It means that the internal wave may break in this region owing to the enhancement of velocity. After internal wave breaks, it generates boluses of dense fluid and propagates up the slope. The round shape of vortices at x = 40 cm for the phase of t/T = 0.0 proves this tendency. In other phase values of t/T = 0.25, 0.5, and 0.75, this bolus propagates and decreases its size and speed owing to the interaction with the return flows. Inspecting the **Fig. 3.10** (b), there is an imposing array of asymmetric vortices in which a thicker clockwise vortex alternates with a depressed counterclockwise vortex. The scales of these vortices decrease when the waves propagate along a slope. Near the density interface, the mean velocity in the lower layer appears to be relatively larger than that in the upper layer. As a consequence, the pairs of

vortices have been distorted but they still keep the quasi-elliptical shape. In addition, the center of ellipse departs upward from the mean density interface at the wave crest, while it deviates slightly downward from the interface at the wave trough. The particle velocity reaches its maximum near the density interface. The flow converges to the front of the wave crest and diverges behind it.

Fig. 3.11 illustrates the measured velocity fields for one wave cycle with an interval of T/4 in the case of T = 7.2 s. The clockwise and counterclockwise vortices are in an orderly line when compared with those in the previous case of T = 5.2 s. This fact suggests that an increase in wave period leads to an increase in the stability of vortices that gradually decrease the size with distance up the slope. From a pair of counter-rotating vortices, one can expect the nonlinearity of internal wave, although the difference of two vertical positions for the counter-rotating vortices is relatively small. It seems that the vortex becomes more flat when it propagates to the shallow water before breaking and becomes round trap of dense water.

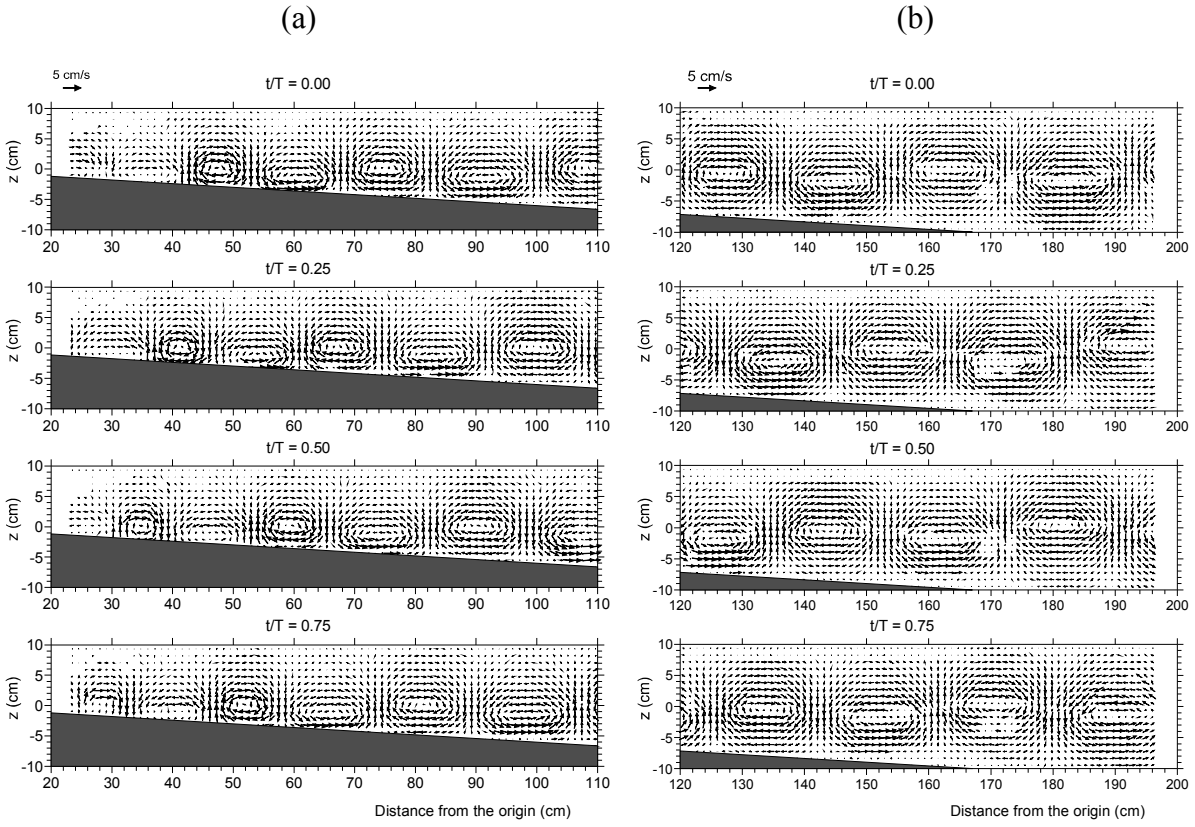

Fig. 3.10 Velocity fields for Case S1

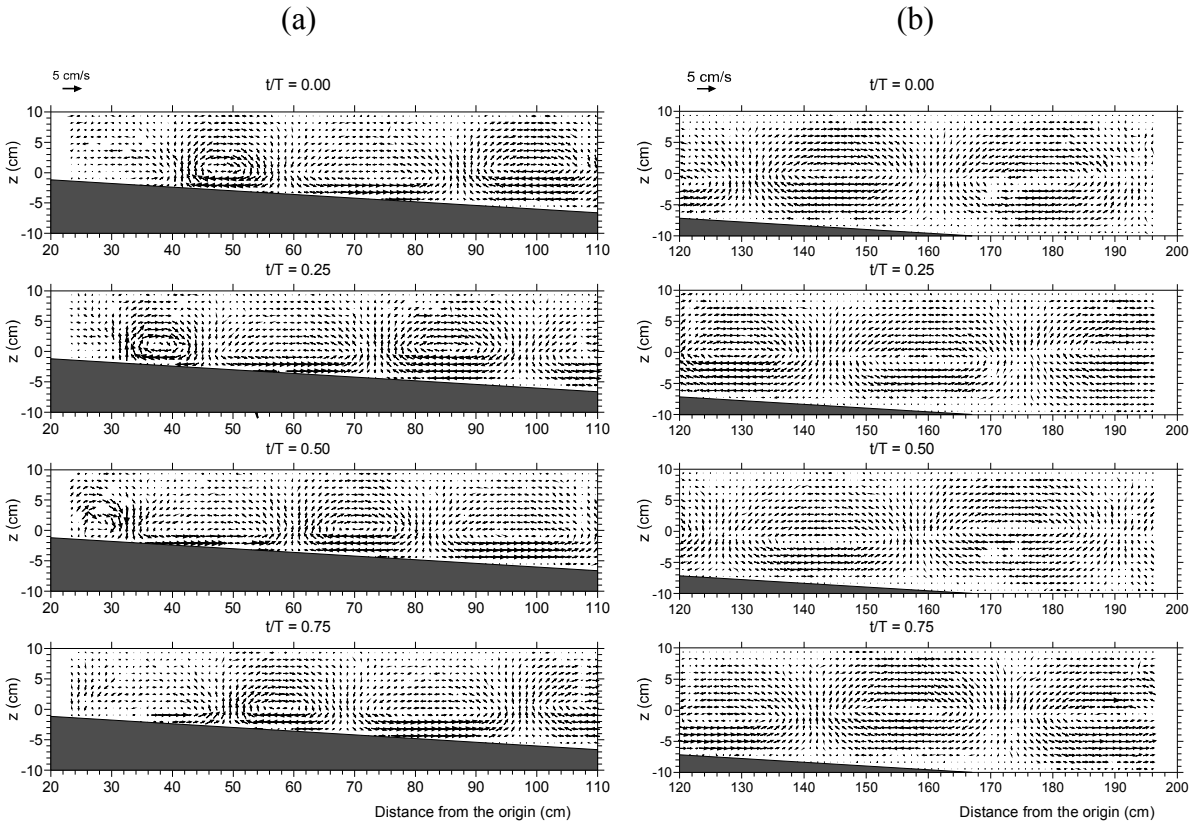

Fig. 3.11 Velocity fields for Case S2

3.2.2 Water particle trajectory

Fig. 3.12 shows the plots of the measured particle orbit geometries for Case S1 during three wave cycles of T = 5.2 s at three locations (a) x = 60 cm, (b) x = 90 cm, and (c) x = 190 cm. The triangle symbol shows a position of water particle estimated from the PIV measurement at interval of 2 cm. At x = 60 cm, the water particles near the interface drift toward the shore whereas particles in the remaining layers tend to move in the direction opposite to that of the wave propagation to conserve mass in whole flume. Water particles move clockwise in the upper layer and anticlockwise in the lower layer. This tendency is quite similar at x = 90 cm. **Fig. 3.12** (c) shows the different movement of water particle very close to the interface at deeper region (x = 190 cm). The particle skips with the wave and it seems that the particle moves further than other particles. When the internal waves propagate in two-layer stratified fluid over a constant slope, the particle excursions in the interface becomes shorter owing to the slowdown of the wave speed due to dissipation and friction. However, the return flow is very noticeable near the origin, especially in the lower layer. After breaking, it generates upslope surging vortex cores of dense fluid (boluses), and these cores continue to propagate further upstream. When they reach the critical elevation, they

stop, and subsequently, mix and return to the lower layer. This explains the reason why the particles in the lower layer drift relatively long distance toward the shore compared to those in the offshore direction.

Fig. 3.13 depicts the water particle trajectories for the same thickness ratio with T = 7.2 s. The initial positions of water particle are x = 60 cm, 90 cm, and 190 cm. Carefully inspecting the movements of water particles in all elevations, it can be confirmed that the particle trajectories are not closed in the total depth. At x = 60 cm, the particle moves similar to that in the case of T = 5.2 s, except the excursion length. The water particles around density interface tend to move in the direction of the wave propagation while those in the remaining region travel in the opposite direction. Near the bottom, the water particles are quite close at three locations during three wave cycles.

(a) x = 60 cm (b) x = 90 cm (c) x = 190 cm

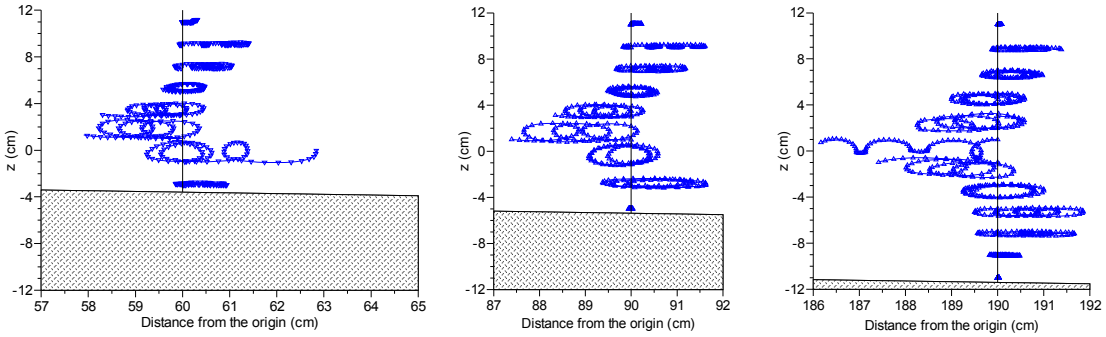

Fig. 3.12 Water particle trajectories for Case S1

(a) x = 60 cm (b) x = 90 cm (c) x = 190 cm

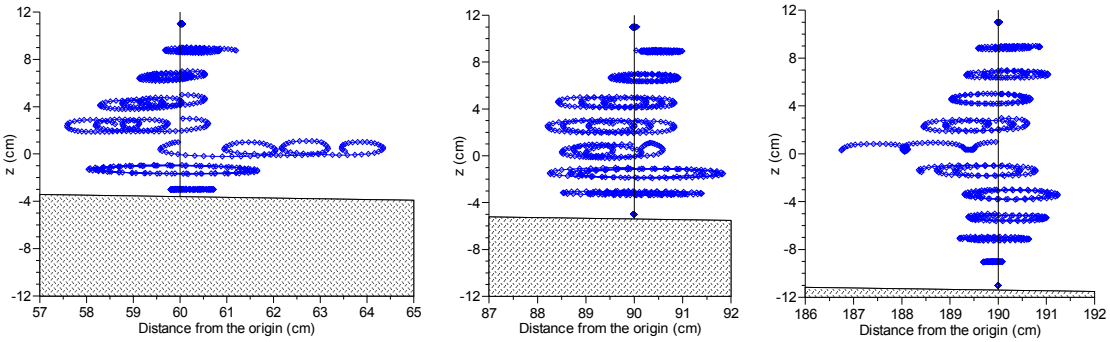

Fig. 3.13 Water particle trajectories for Case S2

3.2.3 Internal wave celerity

In addition to the distributions of velocity vectors and particle trajectories along the gentle slope, we considered spatial variations of wave celerity. Lamb (1932) proposed a dispersion relation between wave speed and wavenumber from the linearized theory as

$$c = \sqrt{\frac{g}{k}\frac{\rho_{II} - \rho_I}{\rho_I \coth kh_I + \rho_{II} \cosh kh_{II}}} \tag{3.4}$$

The wave celerity was estimated from spatial wave profiles obtained by image processing technique. **Fig. 3.14** shows the variations of internal wave celerity for Cases S1 and S2, respectively. In each figure, the measured and theoretical celerities are depicted. The tendency of measured data is in good agreement with the theoretical distributions. Internal wave celerity tends to decrease toward the origin. For the case of T = 5.2 s, the measured celerity is always smaller than those estimated from the dispersion relation and the method of characteristics. The author attributes the difference between the measured and the theoretical celerities to the bottom topography. Eq. (3.4) was derived for a flat bottom condition; however, the present bottom of wave tank consists of flat and sloped bottom. **Fig. 3.14** (b) shows a similar comparison of celerity in the case of T = 7.2 s. It is noticed that for this case, the measured celerity is reasonably well fit with theoretical results when compared with that for the case of T = 5.2 s. It suggests that only numerical method will work well for the calculations of this type of topography; however, additional components such as frictions in the formula of dispersion relation and the method of characteristics (Eq. 2.14) will expand the range of computation.

(a) T = 5.2 s (b) T = 7.2 s

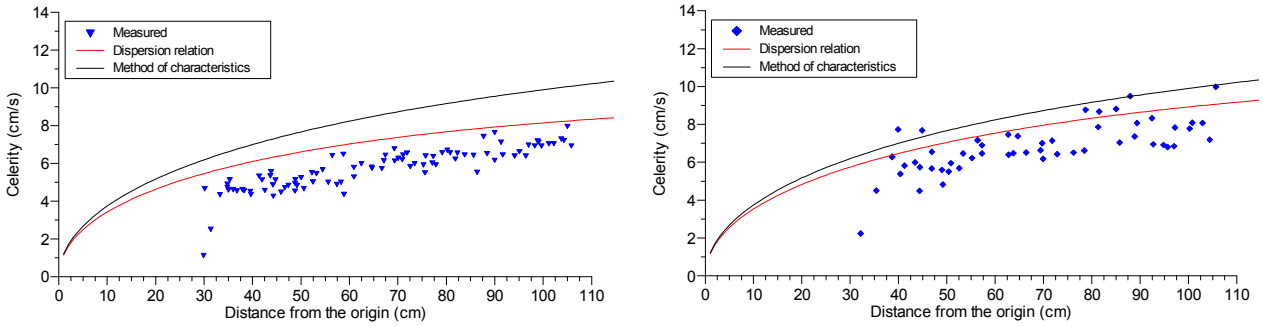

Fig. 3.14 Distributions of wave celerity for Cases S1 and S2

3.3. Conclusions

In this chapter, the experimental arrangements, methods, and results were presented to investigate the physical aspects of internal waves propagating on a sloping bottom in a density-stratified two-layer fluid. The velocity fields have been measured using the PIV technique for different wave periods and thickness ratios. The water particle trajectories were computed using Euler–Lagrangian method that transfers the velocity at the Eulerian grids into the Lagrangian velocity. The visualization method using dye streaks was also described to depict the mass transport of water particles in a wave tank. Wave celerity was experimentally and theoretically investigated. Over the range of interest, the spatial variations of internal wave celerity were fairly predicted by the dispersion relation equation. In addition, the wave celerity was obtained by analyzing the experimental data and compared with the result by the method of characteristics.

Using a PIV system, the successive velocity fields over one wave cycle were measured. The instantaneous velocity vector map clearly illustrated a vortex pair when the thickness ratio was relatively large in a fluid of two density layers. The vertical distributions of velocities analyzed from the PIV data were also presented at different phases. The algorithm for PIV was employed to compute Lagrangian velocity and track water particle displacements in Eulerian grids. The particle trajectories in a cross section were simulated using a solution based on the definition of the Lagrangian approach to the method of characteristics. The proposed approach of the PIV can be applied to the Lagrangian description of the trajectory of a water particle when internal waves propagate above a sloping bottom.

Chapter 4

Two-Dimensional Hydrodynamic Model and Simulation of Experiments

Abstract

This chapter presents the basics of two dimensional hydraulic model which was used to simulate the phenomena in the laboratory tank. The momentum and continuity equations were solved with the Boussinesq approximation. The model was used to investigate the kinematics of internal waves which propagate over a gentle slope in a two-layer stratified density fluid. The interfacial displacement, velocity, particle trajectory were computed by two-dimensional hydrodynamic model. The computed results were compared with measured results.

4.1. Introduction

Stably stratified flows are prevalent in the natural environment. The presence of the buoyancy force due to the density stratification may have a substantial effect on the flow development and mixing processes, and hence influence the distribution of scalar substances such as suspended sediment and pollutants.

In this study, the two-dimensional (2D) hydrodynamic model was used to simulate the phenomenon related to internal wave propagation in a laboratory tank. The numerical model helps to reproduce more results with very fine spatial and temporal scales to shed some light on the riddles of internal wave kinematics. The basics of numerical model, the computed results and comparisons are presented in the following parts.

4.2. Numerical method

4.2.1 Governing equations

The equations of continuity, momentum and salinity for incompressible flow in terms of Cartersian tensors

$$\frac{\partial \rho}{\partial t}+\frac{\partial \rho u_j}{\partial x_j}=0 \tag{4.1}$$

$$\frac{\partial u_i}{\partial t}+\frac{\partial u_i u_j}{\partial x_j}=-\frac{1}{\rho}\frac{\partial p}{\partial x_i}+\frac{\partial}{\partial x_j}\left\{\upsilon\left(\frac{\partial u_i}{\partial x_j}+\frac{\partial u_j}{\partial x_i}\right)\right\}-g\delta_{i3} \tag{4.2}$$

$$\frac{\partial S}{\partial t}+\frac{\partial u_j S}{\partial x_j}=\frac{\partial}{\partial x_j}\left\{\frac{\upsilon}{S_c}\frac{\partial S}{\partial x_j}\right\} \tag{4.3}$$

For all experiments, it can be assumed the difference of temperature in whole wave tank is insignificant, so that

$$\rho = f\left(S\right) \tag{4.4}$$

It is proved that the Boussinesq approximation can be used for present problem due to the change of water density is not more than 10% (Shintani, 2005). It means that the density is assumed to be constant except when it contributes directly to the buoyancy. Therefore, the governing equations can be written as

$$\frac{\partial u_j}{\partial x_j}=0 \tag{4.5}$$

$$\frac{\partial u_i}{\partial t}+\frac{\partial u_i u_j}{\partial x_j}=-\frac{1}{\rho_0}\frac{\partial p}{\partial x_i}+\frac{\partial}{\partial x_j}\left\{\upsilon\left(\frac{\partial u_i}{\partial x_j}+\frac{\partial u_j}{\partial x_i}\right)\right\}-\frac{\tilde{\rho}-\rho_0}{\rho_0}g\delta_{i3} \tag{4.6}$$

$$\frac{\partial S}{\partial t}+\frac{\partial u_j S}{\partial x_j}=\frac{\partial}{\partial x_j}\left\{\frac{\upsilon}{S_c}\frac{\partial S}{\partial x_j}\right\} \tag{4.7}$$

$$\tilde{\rho}=\rho_0\left\{1+\beta_s\left(S-S_0\right)\right\} \tag{4.8}$$

where

ρ = density

t = time

x_i = the Cartesian coordinates

u_i = the corresponding velocity components for x_i

υ = the kinematic viscosity

g = the gravity acceleration

δ = the Kronecker's delta

S = the salinity

S_c = the Schmidt number (= 638 for saline water at $T = 20^0$C)

β_s = a constant

S_0 = the reference value of salinity

4.2.2 Numerical schemes

To solve these governing equations, an explicit finite difference technique with the fractional-step method is employed on staggered grids. The advective terms are discretized using the ULTIMATE-QUICKEST scheme (Leonard, 1979; Lin and Falconer, 1997), while the diffusive terms are discretized by the central difference scheme. With those techniques, the velocity and density distribution are computed in the whole flume with spatial resolutions of Δx , Δz , and a time step of Δt . The particle trajectory is estimated with the same technique described above for the experiments.

a) Fractional-Step Method

Time integration of the Navier-Stokes equations is carried out by means of the fractional-step procedure, first suggested by Harlow & Welch (1965) and Chorin (1968), and modified by Kim & Moin (1985). In this method, at first step, the momentum equations without pressure gradient terms are explicitly integrated to yield an approximate velocity $\overline{u_i}$, which is in general not divergence free. We can write the momentum equation of the first step by a tensor form using explicit Euler scheme in time discretization.

$$\frac{\overline{u_i} - u_i^n}{\Delta t} = -\frac{\partial u_i^n u_j^n}{\partial x_j} + \frac{\partial}{\partial x_i}\left\{\left(\frac{1}{\mathrm{Re}} + \upsilon_t\right)\left(\frac{\partial u_i^n}{\partial x_j} + \frac{\partial u_j^n}{\partial x_i}\right)\right\} - Ri\rho\delta_{i3} \tag{4.9}$$

where u^n is the velocity at known present time step and Δt is the time increment. In the second step, a correction is applied to that velocity field to produce a divergence free velocity field.

$$\frac{u_i^{n+1} - \overline{u_i}}{\Delta t} = -\frac{\partial p_i^{n+1}}{\partial x_i} \tag{4.10}$$

where u^{n+1} is the velocity at unknown next time step. Therefore, u^{n+1} is the solution of the Navier-Stokes equations. Taking the divergence of (4.27) and using $div(u^{n+1}) = 0$, we obtain the Poisson equation of pressure as follows,

$$\frac{\partial}{\partial x_j}\left(\frac{\partial p^{n+1}}{\partial x_j}\right) = \frac{\partial u_j}{\partial x_j} / \Delta t \tag{4.11}$$

The above equation is solved by an iterative matrix solver (e.g. SOR method). Once p^{n+1} is obtained, u^{n+1} can be calculated from (4.10).

In the present numerical method, the governing equations were divided into two phases except the continuity equation. The governing equations can be written in the general form as,

$$\frac{\partial f}{\partial t} + u_i \frac{\partial f}{\partial x_i} = G \tag{4.12}$$

where f represents u, S, k and ε. G represents the non-advective terms for each equation such as the diffusion and the external force terms. The above equation is splitted into an advective phase and a non-advective phase as follows,

$$\frac{\partial f}{\partial t} + u_i \frac{\partial f}{\partial x_i} = 0 \tag{4.13}$$

$$\frac{\partial f}{\partial t} = G \tag{4.14}$$

In the first step of the fractional-step method, firstly the advective phase equation (4.13) is solved by the ULTIMATE-QUICKEST scheme. After calculating the advective phase, the non-advective phase (4.14) is calculated before the pressure correction.

b) ULTIMATE-QUICKEST scheme

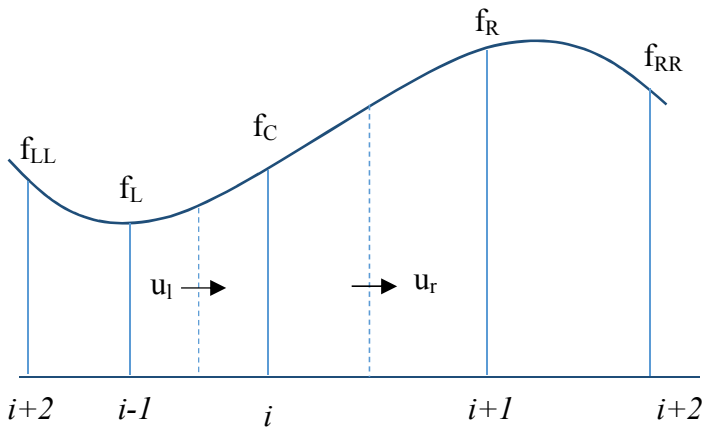

Fig. 4.1 Definition of terms

To solve the Eq. (4.13), the ULTIMATE-QUICKEST scheme was applied.

$$f_C^{n+1} = f_C^n - \left[(Cr)_r f_r - (Cr)_l f_l \right] \tag{4.15}$$

where $(Cr)_l$ and $(Cr)_r$ = Courant number at left and right faces of grid cell, respectively, given by:

$$(Cr)_l = \left(\frac{U_l}{h} \right)_l \frac{\Delta t}{\Delta x} \tag{4.16}$$

$$(Cr)_r = \left(\frac{U_l}{h} \right)_r \frac{\Delta t}{\Delta x} \tag{4.17}$$

f_C = value of parameter f at the center of the grid cell, at time n.

f_l and f_r can be determined by the QUICKEST scheme at the left and right faces as follows

$$f_l = f_l^L - \frac{(Cr)_l}{2} GRAD - \left(\frac{1}{6} - \frac{(Cr)_l^2}{6} \right) CURV \tag{4.18}$$

where

$$f_l^L = \frac{f_L^n + f_C^n}{2} \tag{4.19}$$

$$GRAD = f_C^n - f_L^n \tag{4.20}$$

$$CURV = f_C^n - 2f_L^n + f_{LL}^n \text{ for } (Cr)_l > 0$$

$$CURV = f_R^n - 2f_C^n + f_L^n \text{ for } (Cr)_l < 0$$

f_r can be obtained with a similar manner. To eliminate any unphysical oscillations, two normalized variables are introduced for each cell face. For example, if $(Cr)_r > 0$ for the right cell face:

$$\overline{f}_C^n = \frac{f_C - f_U}{f_D - f_U} \tag{4.21}$$

$$\overline{f}_r = \frac{f_r - f_U}{f_D - f_U} \tag{4.22}$$

where

f_C = parameter " f " at center of the grid

f_U = upstream grid center parameter " f "

f_D = upstream grid center parameter " f "

These parameters are described in **Fig. 4.2**.

The oscillation free solution can be obtained when the following conditions are satisfied

$$\overline{f}_r \le \overline{f}_C^n \Big/ (Cr)_r \text{ for } 0 < \overline{f}_C^n \le 1 \tag{4.23}$$

$$\overline{f}_C^n \le \overline{f}_r \le 1 \text{ for } 0 \le \overline{f}_C^n \le 1 \tag{4.24}$$

$$\overline{f}_r = \overline{f}_C^n \text{ for } \overline{f}_C^n < 0, \text{ or } \overline{f}_C^n > 1 \tag{4.25}$$

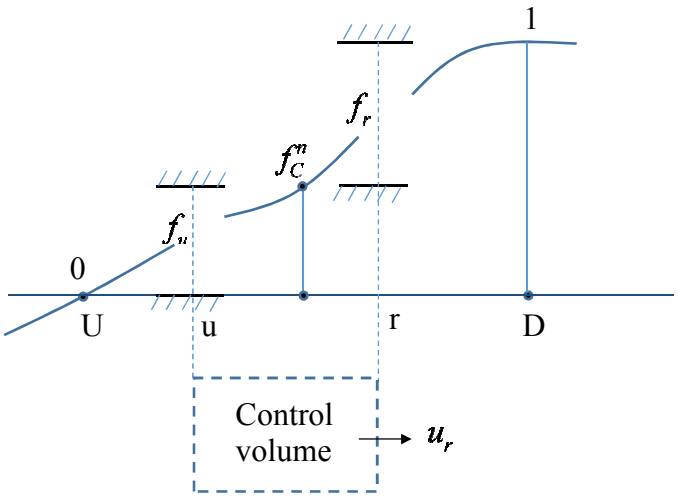

Fig. 4.2 Normalized node-value in case of locally monotonic behavior

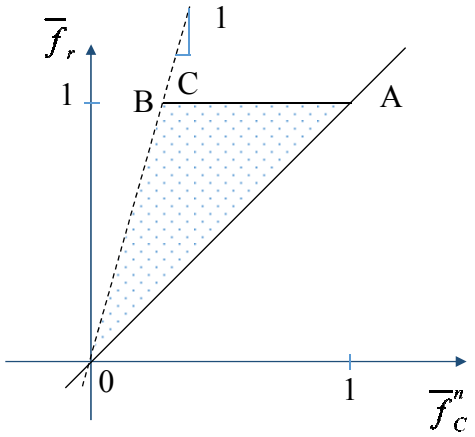

Fig. 4.3 Normalized variable diagram showing universal limiter boundaries

The conditions in Eq. (4.23)-(4.25) can be plotted as the dotted region shown in **Fig. 4.3**. If the point ($\overline{f}_C^n$, $\overline{f}_r$) lies within the dotted region then the unadjusted face value f_r is used to solve Eq. (4.13). If that point lies outside the dotted region, then $\overline{f}_r$ is replaced with the nearest allowable value of $\overline{f}_r$ for the same value of $\overline{f}_C^n$. After that, f_r is reconstructed as

$$f_r = f_U + \overline{f}_r \left(f_D + f_U \right) \tag{4.26}$$

Following this formulation, Eq. (4.13) is now solved using a bounded value of f_r.

c) Non advective-phase differencing

Non-advective phase includes the viscous, diffusion, pressure gradient and external force terms. The viscous and diffusion terms are approximated by using second-order central differencing scheme. For the horizontal velocity

$$\frac{\partial^2 u}{\partial x^2} = \frac{\frac{u_{i+1} - u_i}{\Delta x} - \frac{u_i - u_{i-1}}{\Delta x}}{\Delta x} = \frac{u_{i+1} - 2u_i + u_{i-1}}{\Delta x^2} \tag{4.27}$$

The pressure gradient terms are discretized by using the first-order forward differencing schemes

$$\frac{\partial p}{\partial x} = \frac{p_{i+1} - p_i}{\Delta x} \tag{4.28}$$

d) Pressure treatment

The Poisson Eq. (4.11) is discretized by using the central differencing scheme for two-dimensional case as

$$\frac{p_{i+1,j}^{n+1} - 2p_{i,j}^{n+1} + p_{i-1,j}^{n+1}}{\Delta x^2} + \frac{p_{i,j+1}^{n+1} - 2p_{i,j}^{n+1} + p_{i,j-1}^{n+1}}{\Delta y^2} = \frac{\frac{u_{i+1,j}^n - u_{i,j}^n}{\Delta x} - \frac{v_{i,j+1}^n - v_{i,j}^n}{\Delta y}}{\Delta t} \tag{4.29}$$

$$d_0 p_{i,j}^{n+1} + d_1 p_{i+1,j}^{n+1} + d_2 p_{i-1,j}^{n+1} + d_3 p_{i,j+1}^{n+1} + d_4 p_{i,j-1}^{n+1} = \frac{D_{i,j}}{\Delta t} \tag{4.30}$$

where

$$d_1 = d_2 = \frac{1}{\Delta x^2} \ ,$$

$$d_3 = d_4 = \frac{1}{\Delta y^2}$$

$$d_0 = -d_1 - d_2 - d_3 - d_4$$

$$D_{i,j} = \frac{u_{i+1,j}^n - u_{i,j}^n}{\Delta x} + \frac{v_{i,j+1}^n - v_{i,j}^n}{\Delta y}$$

The SOR method solves the above equation iteratively as follows

$$p_{i,j}^{m+1} = p_{i,j}^m + \omega \left\{ \frac{1}{d_0} \left(\frac{D_{i,j}}{\Delta t} - \left(d_1 p_{i+1,j}^m + d_2 p_{i-1,j}^m + d_3 p_{i,j+1}^m + d_4 p_{i,j-1}^m \right) \right) - p_{i,j}^m \right\} \tag{4.31}$$

where m is the number of iteration and ω is the overrelaxation parameter (it is set at 1.6). If $\left(p_{i,j}^{m+1} - p_{i,j}^{m}\right)$ is smaller than a certain small value, $p_{i,j}^{m+1}$ is considered to be the solution of the Eq. (4.11). The process of computation follows the flow chart as shown in **Fig. 4.4**.

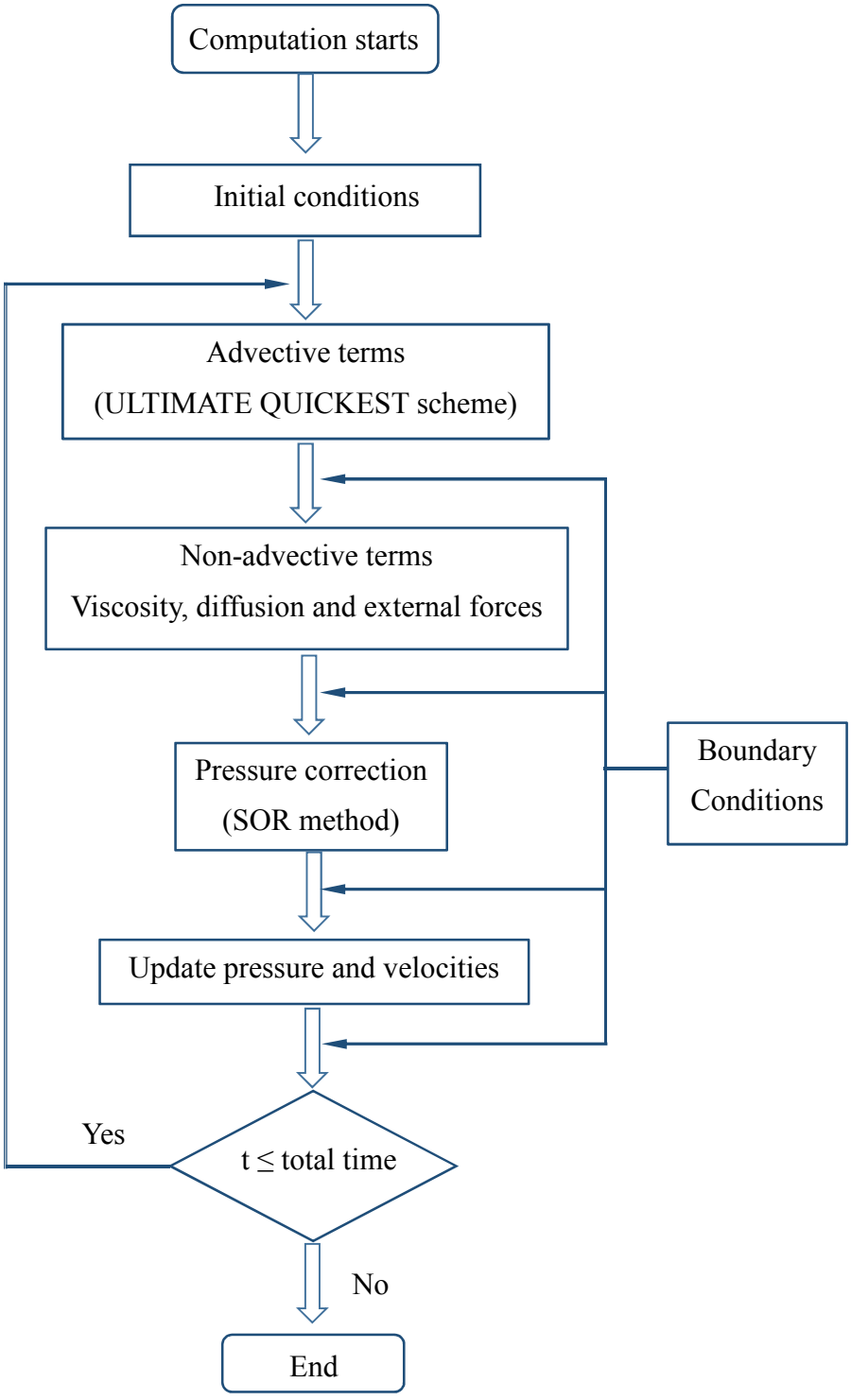

Fig. 4.4 Flowchart of numerical method

4.2.3 Boundary and initial conditions

** Boundary conditions*

In this model, rigid lid and slip conditions were applied at the water surface. The non-slip condition was applied to wall boundaries, including the slope and bottom boundaries. The internal-wavemaker was positioned at one end of the flume. Two periodic fluxes with different directions of movement were applied to the two layers, as shown in **Fig. 4.5**. The flux F varied periodically with time t as

$$F = F_{\max} \sin 2\pi \frac{t}{T} \tag{4.32}$$

where T = specified wave period and $F_{\max}$ = the maximum flux.

** Initial conditions*

During the running time, the temperature was kept constant in whole flume. The initial salinity is set at 40 ppt (ρ = 1028 mg/cm^3) and 0 ppt (ρ = 998 mg/cm^3) in the lower and upper layers, respectively. The initial velocity field is set at 0 cm/s.

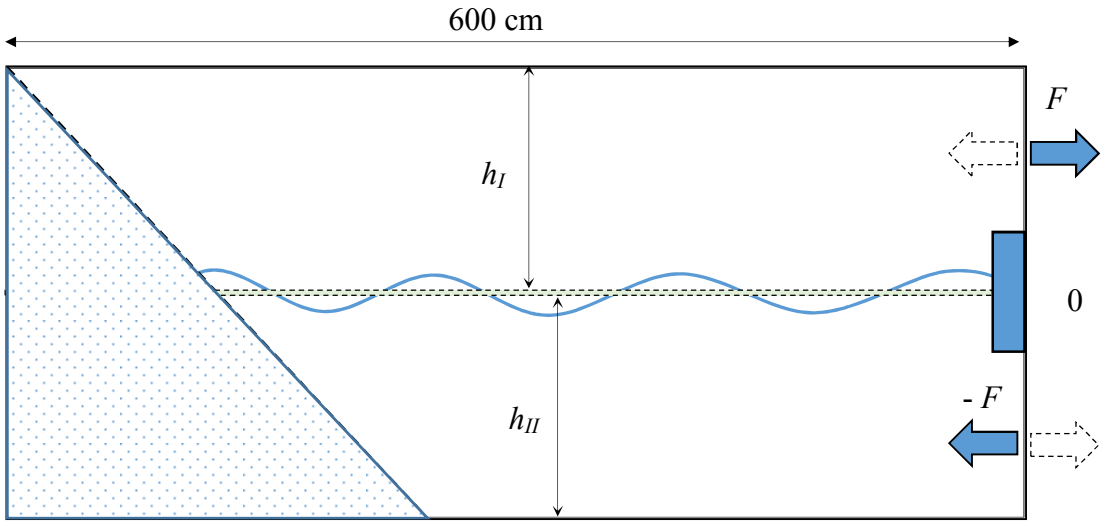

Fig. 4.5 Schematic diagram of computation domain

4.3. Results

4.3.1 Interfacial displacements

The numerical model was calibrated using the wave height estimated at the location of 100 cm from the wave maker. After that, the computed interfacial displacement from the 2D hydrodynamic model was compared with one from the measurement using light attenuation method. For example, in the case of $h_I : h_{II}$ = 15 cm : 15 cm, and T = 7.2 s (Case S4), the measured internal wave height was approximately 2.7 cm at x = 100 cm (**Table 3.1**). **Fig. 4.6** shows a comparison between the measured and computed interfacial displacements at x = 150 cm. The temporal interfacial variation by the 2D model is in good agreement with the measured data. Because it is impossible to avoid the effects of return flow, reflection and higher-order harmonies owing to the closed tank in most experiment, the discrepancy between experimental and computed results sometimes occurs. However, this agreement strongly supports the usefulness of the numerical method for internal waves on a sloping bottom.

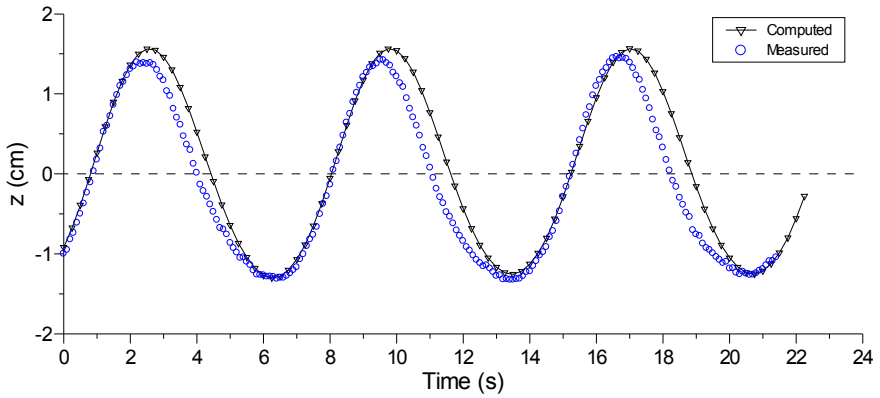

Fig. 4.6 Interfacial displacements at x = 150 cm for Case S4 from the 2D model and the present experiment

4.3.2 Wave celerity

The wave celerity was estimated from spatial wave profiles obtained by light attenuation method at several phases. **Fig. 4.7** and **Fig. 4.8** show the variations of internal wave celerity for the cases of $h_I : h_{II}$ = 15 cm : 15 cm, and $h_I : h_{II}$ = 10 cm : 20 cm, respectively. **Fig. 4.7** (a) depicts the variations of measured and computed celerities with the result of Eq. (3.4) for T = 5.2 s (Case S3) while **Fig. 4.7** (b) show the similar variations for T = 7.2 s (Case 4). The computed and measured data are in good agreement with the theoretical

distribution and they tend to vanish near the origin. **Fig. 4.8** shows similar comparisons in the case of $h_I : h_{II}$ = 10 cm : 20 cm. It is noticed that for the case of T = 7.2 s the computed and measured celerities are smaller than the theoretical celerity from x = 100 cm to x = 200 cm. Near the origin (between x = 0 and x = 40 cm), the computed and measured values are scatter when compared with the values from Eq. (3.4). In this region, breaking, reflection and return flows exist. It seems that near the origin, in the case of T = 7.2 s the measured celerity is larger than computed and theoretical celerities. The numerical model is confirmed to reproduce well the celerity of internal waves propagating over a constant slope in a two-layer density stratified water.

(a) T = 5.2 s

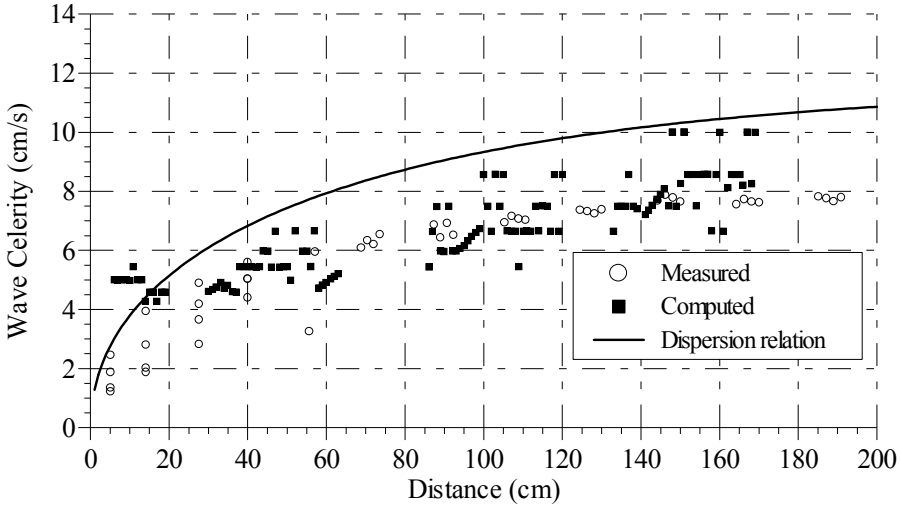

(b) T = 7.2 s

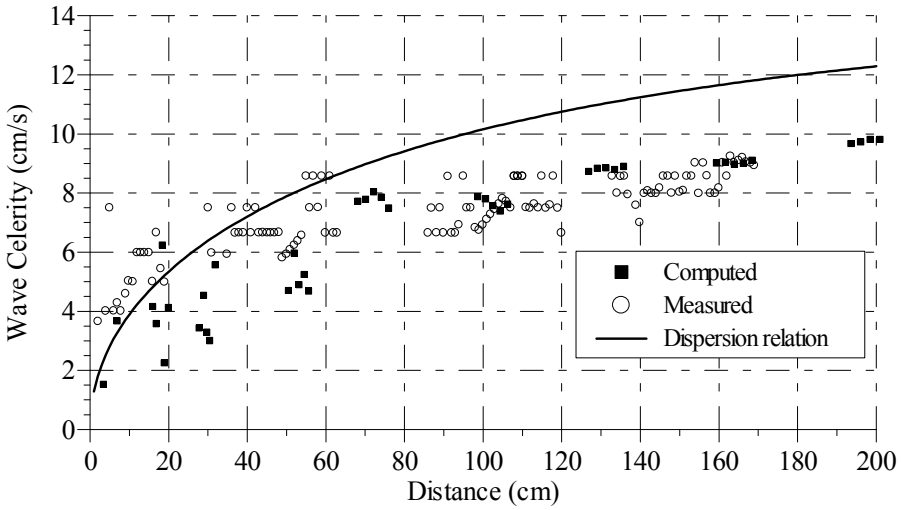

Fig. 4.7 Distributions of wave celerity for Cases S3 and S4

(a) T = 5.2 s

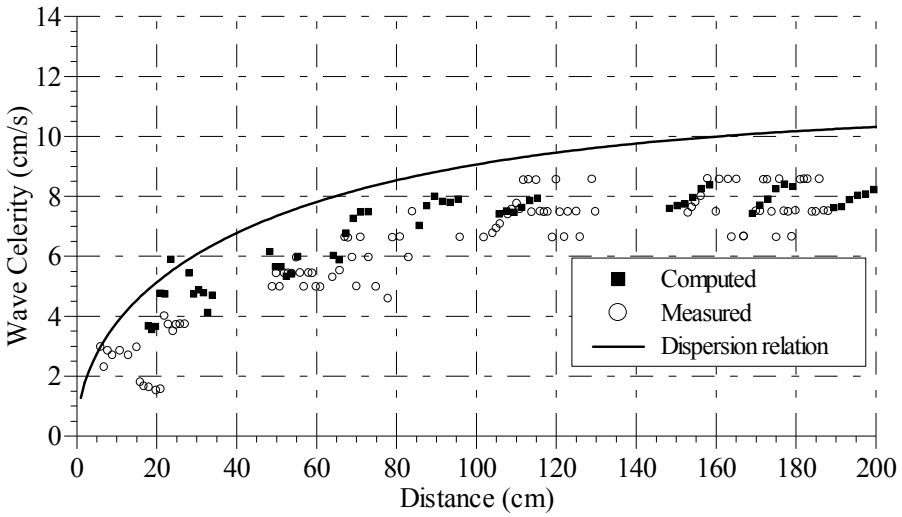

(b) T = 7.2 s

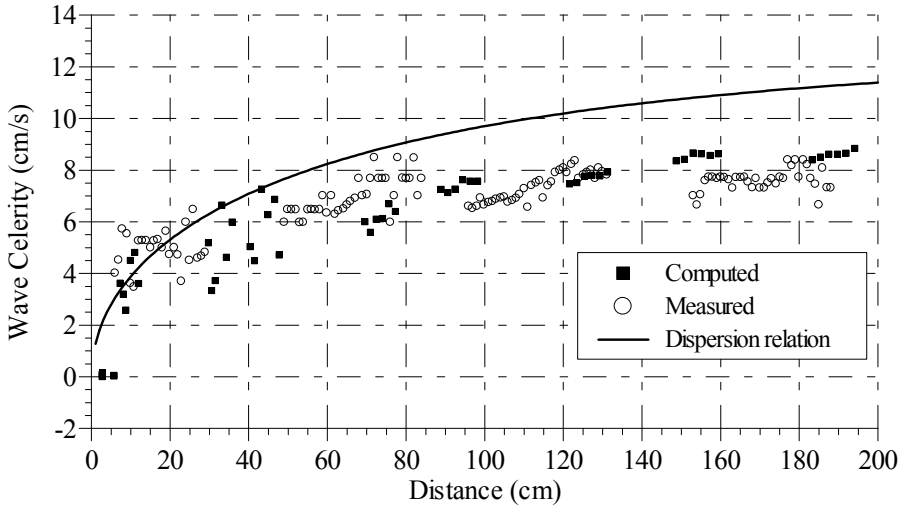

Fig. 4.8 Distributions of wave celerity for Cases S5 and S6

4.3.3 Instantaneous velocity fields

Fig. 4.9 shows the velocity vector fields induced by internal waves in Case S3. The abscissa and ordinate are the horizontal and vertical distances from the origin, respectively. Internal waves propagate from right to left, i.e., in the negative x direction. **Fig. 4.9** (a) depicts the measured instantaneous velocity fields for four different phase values of t/T = 0, 0.25, 0.50, and 0.75. The corresponding wave height is H = 2.6 cm at 100 cm from the wavemaker. Each vector image consists of two pictures taken simultaneously using two high-

definition digital video cameras. There is an imposing array of asymmetric vortices, in which a thicker clockwise vortex alternates with a depressed counterclockwise vortex. The scales of these vortices decrease when the waves propagate along a slope. Near the density interface, the mean velocity in the lower layer appears to be relatively larger than that in the upper layer. As a consequence, the pairs of vortices have been distorted but they still keep the quasi-elliptical shape. In addition, the center of ellipse departs upward from the mean density interface at the wave crest, while it deviates downward slightly from the interface at the wave trough. The particle velocity reaches its maximum near the density interface. The flow converges in the front of the wave crest and diverges behind it. This contributes to creating water particle trajectories in the upper and lower layers, without crossing the density interface. **Fig. 4.9** (b) depicts the corresponding fields computed from the present numerical method. The numerical results show that the vortices gradually become flatter when they travel from offshore to inshore. This tendency is more clearly expressed when the numerical results compared with the PIV result. The numerical model involves the energy dissipation effect due to the instabilities and mixing during the runup event on a slope. As a result, vortices become thinner but velocities increase toward the upper slope.

Fig. 4.10 (a) illustrates the measured velocity fields for one wave cycle with an interval of $T/4$ in the case of h_I : h_{II} = 15 cm : 15 cm and T = 7.2 s (Case S4). The clockwise and counterclockwise vortices are in an orderly line when compared with those in the previous case of T = 5.2 s. This fact suggests that an increase of wave period leads to an increase in the stability of vortices that gradually decrease the size with distance up the slope. From a pair of counterrotating vortices, one can expect the nonlinearity of internal wave, although the difference of two vertical positions for the counterrotating vortices is relatively small. The flow is no more symmetric at the node. **Fig. 4.10** (b) plots the corresponding numerical results. There are approximately three vortices in each panel. The numerical results confirm that the velocities near the density interface in the lower layer are relatively larger than those in the upper layer.

The profiles of velocity components are also compared between the simulation and measurement as shown in **Fig. 4.11** and **Fig. 4.12** at x = 145 cm on the slope. For different phases of one wave cycle, the horizontal and vertical velocity components show the periodic characteristic of the flow induced by periodic internal waves. At the crest of waves, the water flows in the direction due to the incoming vortex (**Fig. 4.11** - a) and the opposed movement occurs as the subsequent vortex arrives (**Fig. 4.11** - c). At crest or trough, the vertical velocity component almost vanishes but at the nodes, the vertical velocity component gets maximum. These profiles confirmed that velocity in the lower layer is higher than that in the upper layer. The vertical velocity gets maximum at the density interface and gradually decreases toward the bottom and surface boundaries. The similar trend can be seen in the **Fig. 4.12** for the Case 4 with wave period of 7.2 s. The numerical model reproduced well the measured velocity

with very high resolutions. It is confirmed that it is reasonable to apply the numerical model to simulate the phenomenon in the wavetank due to the internal waves propagating in a stratified water.

(a) Measured (b) Computed

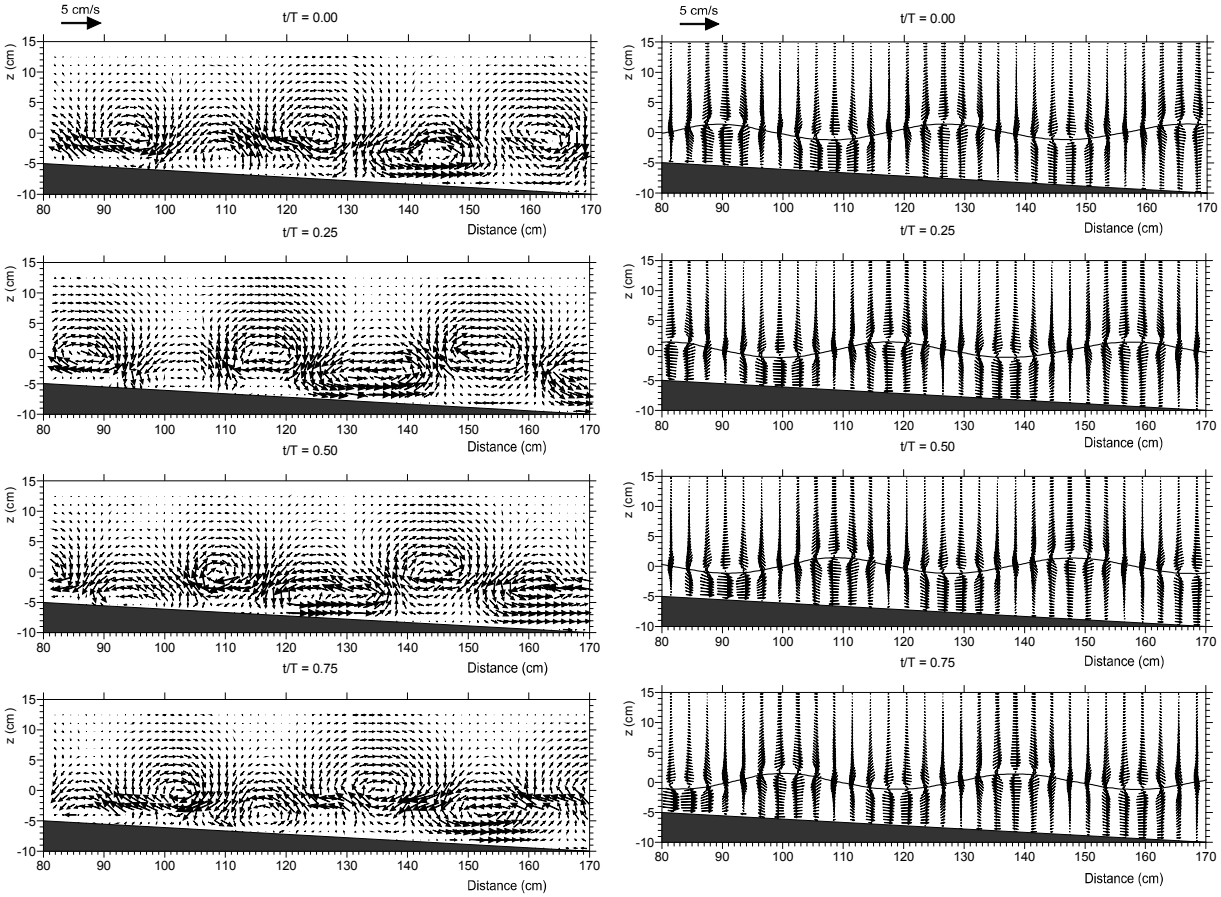

Fig. 4.9 Instantaneous velocity fields of internal waves for Case S3

Fig. 4.13 shows a similar comparison for the generated internal waves in the density-stratified two-layer water when the upper and lower thickness ratio is $h_I : h_{II}$ = 10 cm : 20 cm with T = 5.2 s (Case S5). In **Fig. 4.13** (a) the experimental data points in the range of 135 cm < x < 145 cm are missing due to the flume flange. **Fig. 4.13** (b) show the computed instantaneous velocity fields for t/T = 0, 0.25, 0.50 and 0.75 where the period is 5.2 s. A pair of counterrotating vortices in the experiment shows still a satisfactory pattern. Umeyama and Matsuki (2011) found that the vortex pair turns inconspicuous by changing the thickness rate from $h_I : h_{II}$ = 15 cm : 15 cm to $h_I : h_{II}$ = 5 cm : 25 cm in a fluid of finite depth over a flat bed. The present improvement may be attributed to the replacement of the PIV system from

two frequency-doubled Nd:YAG lasers of 50 mW energy to a frequency-doubled Nd:YAG laser of 8-W energy. It could be confirmed from a series of experiments that the water particle movement in clockwise vortices is stretched in the horizontal direction while the anticlockwise vortices become less elliptical in the longitudinal direction over the slope. **Fig. 4.14** depicts the measured and computed velocity fields for $h_I : h_{II}$ = 10 cm : 20 cm with T = 7.2 s (Case S6). Examining carefully these velocity distributions, the location of vortices and the magnitude of speed in the experiments agree well with these in the calculation.

a) Measured (b) Computed

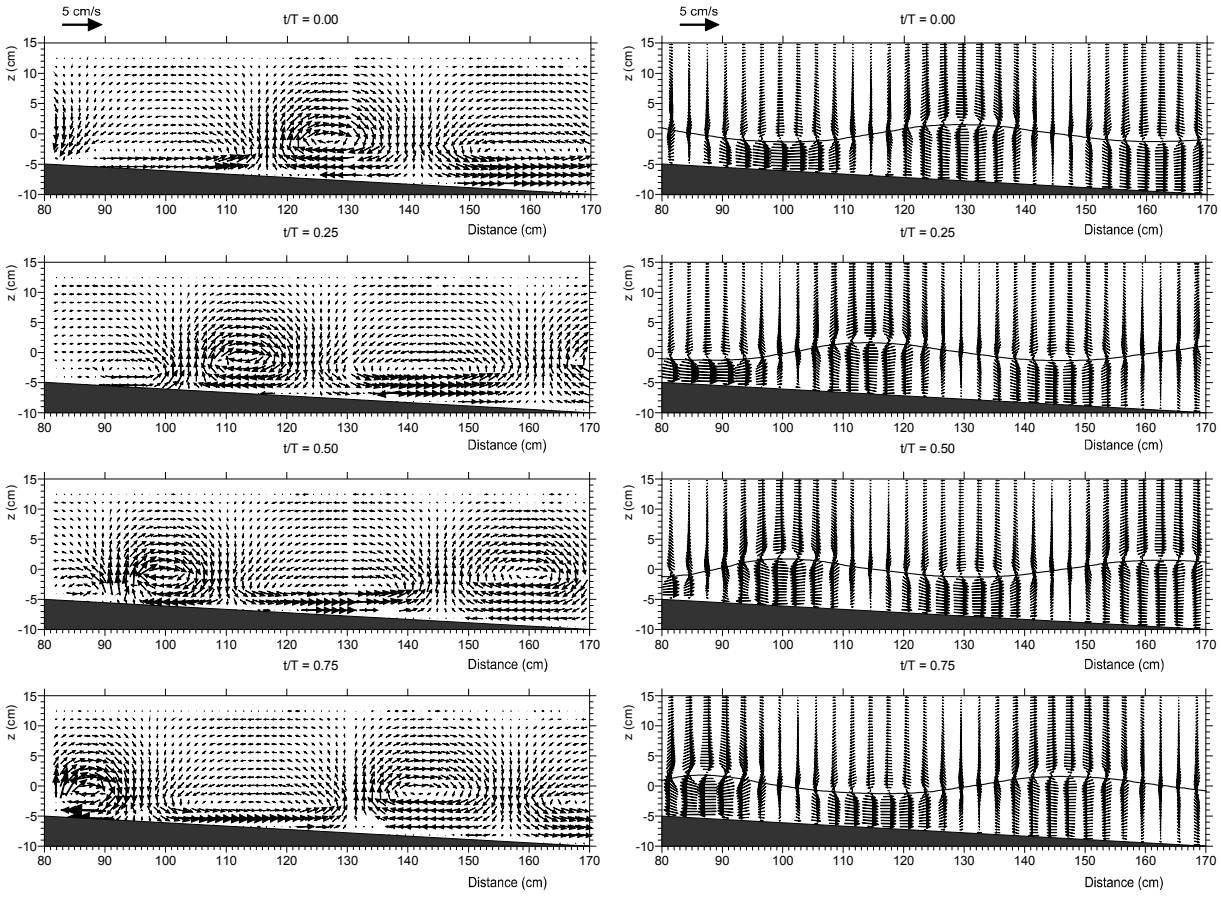

Fig. 4.10 Instantaneous velocity fields of internal waves for Case S4

(a) $t / T = 0.00$

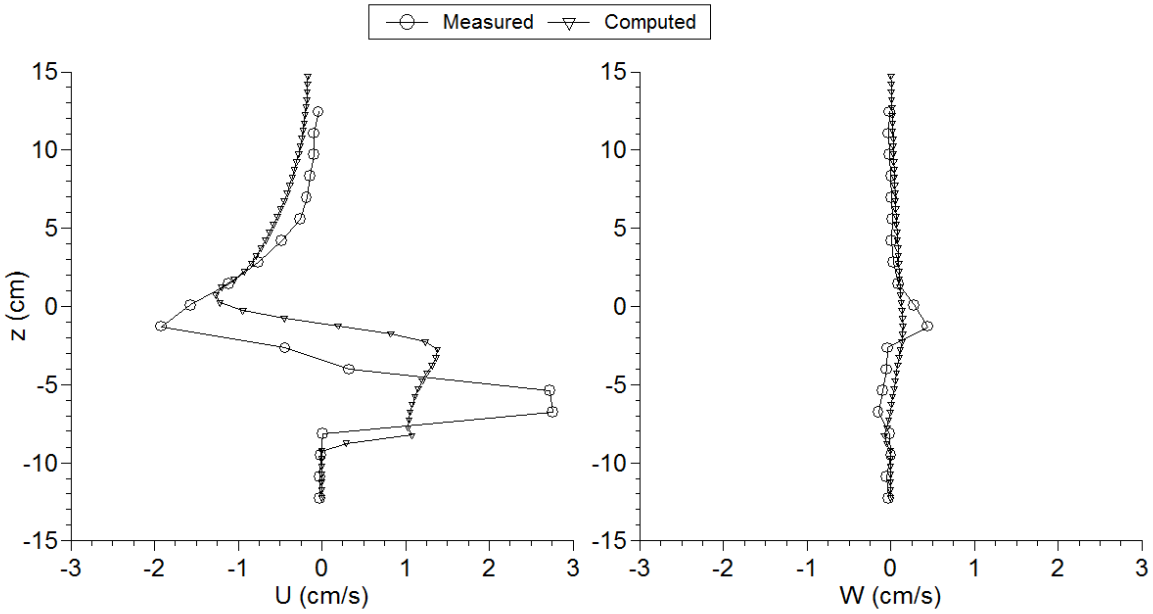

(b) $t / T = 0.25$

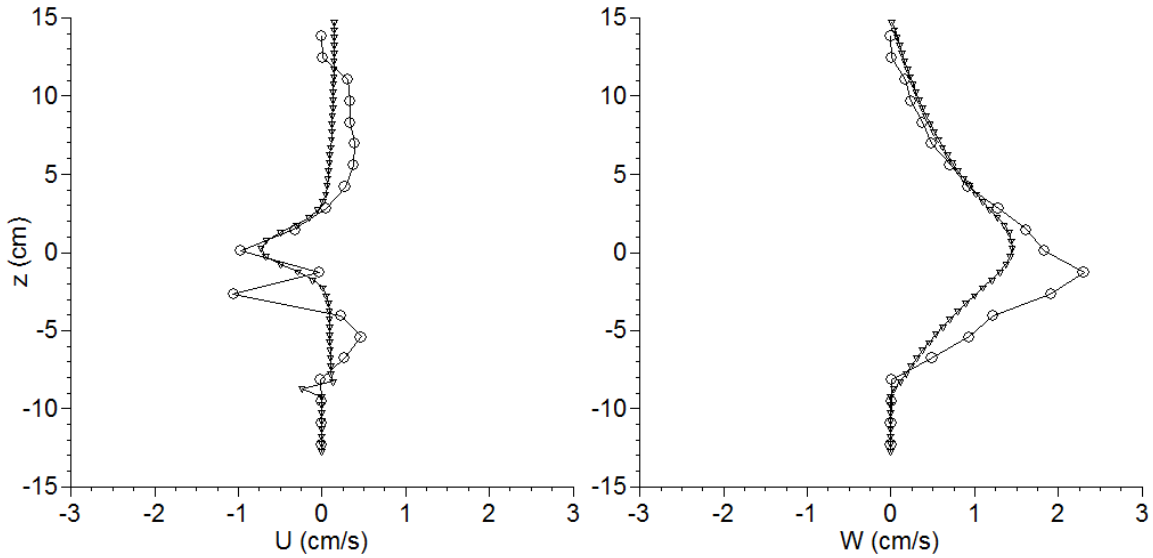

(c) $t / T = 0.50$

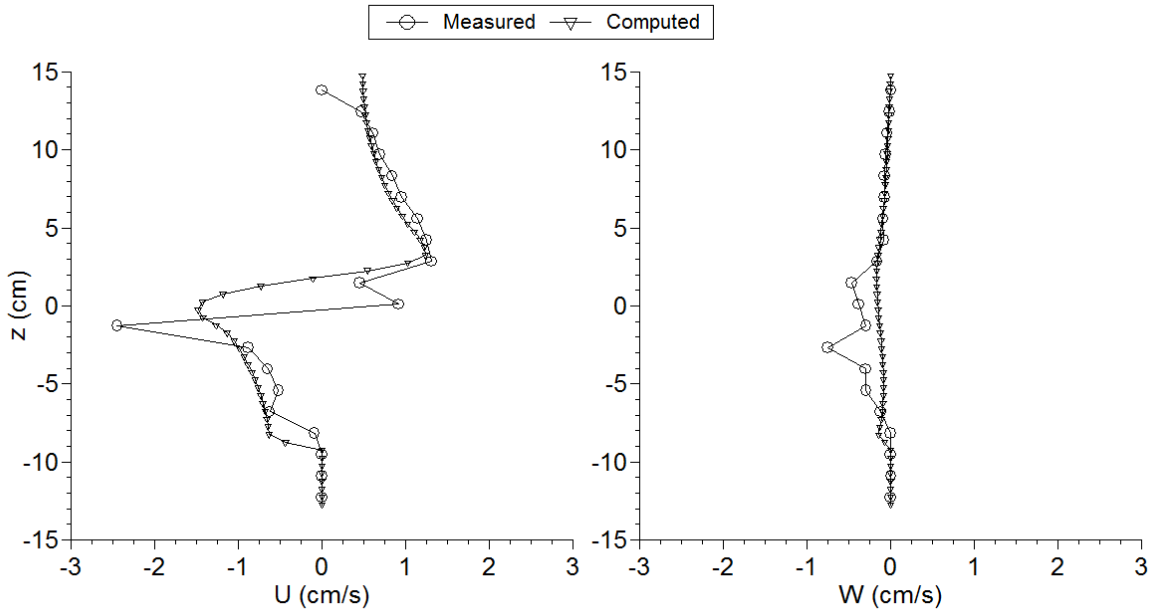

(d) $t / T = 0.75$

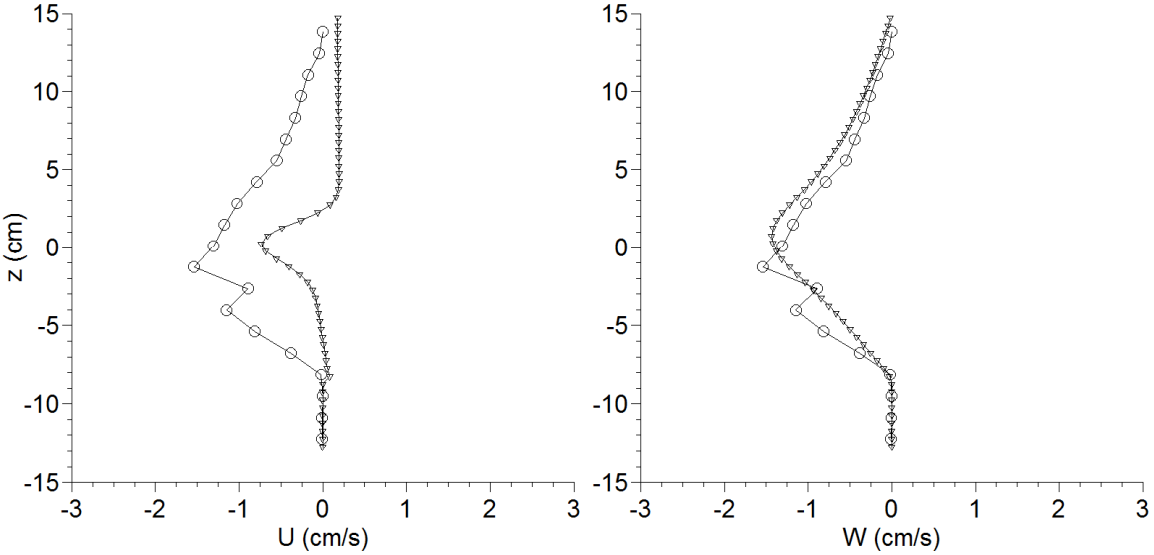

Fig. 4.11 Comparisons between profiles of computed and measured velocity components at x = 145 cm for Case S3; U: horizontal component, W: vertical component of velocity

(a) $t / T = 0.00$

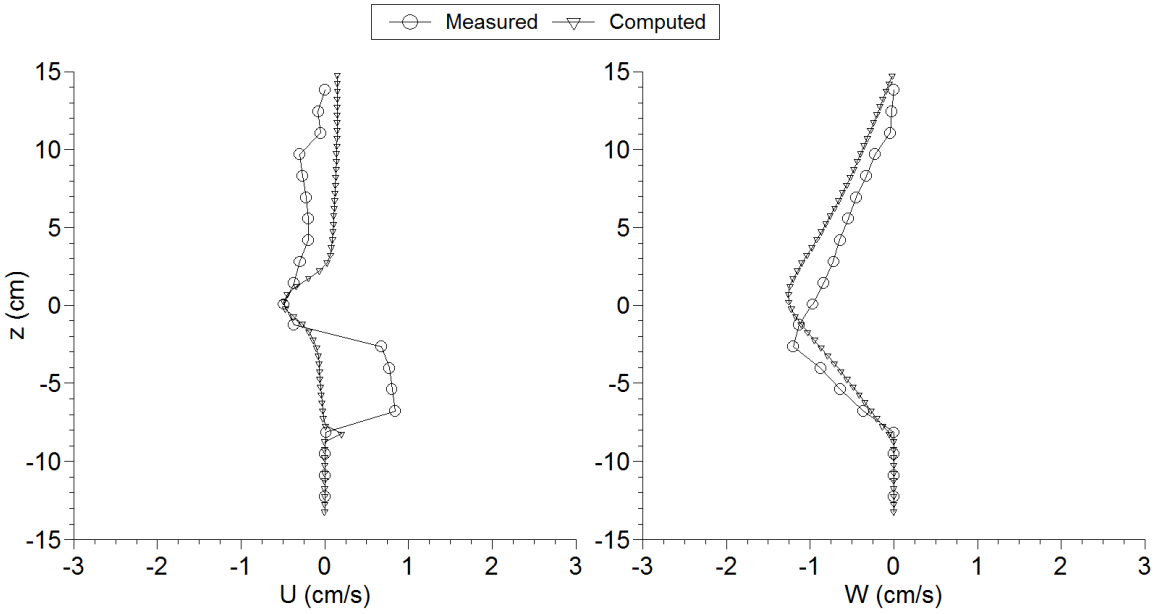

(b) $t / T = 0.25$

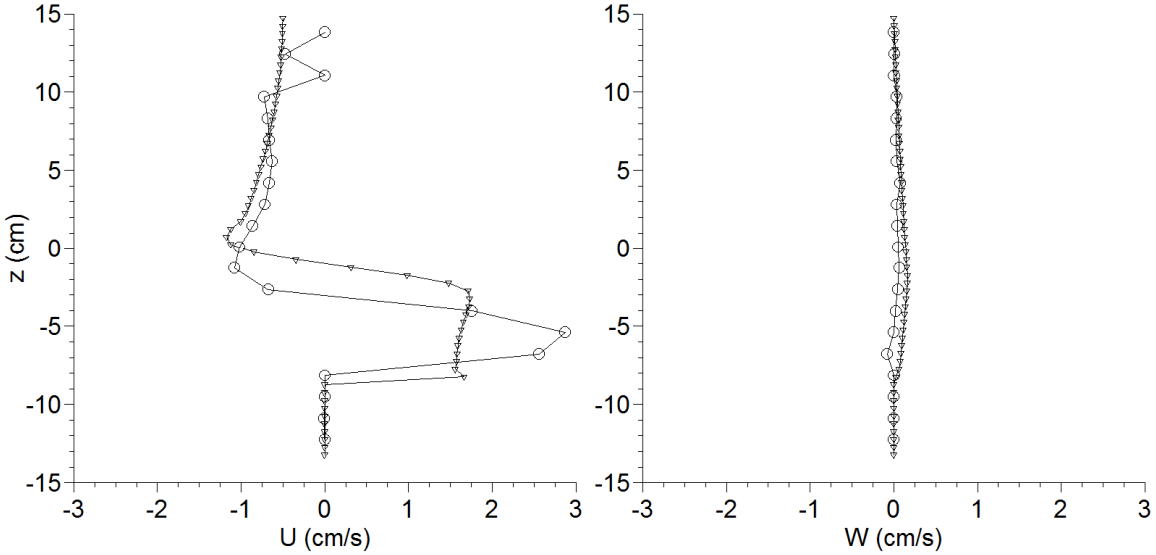

(c) $t / T = 0.50$

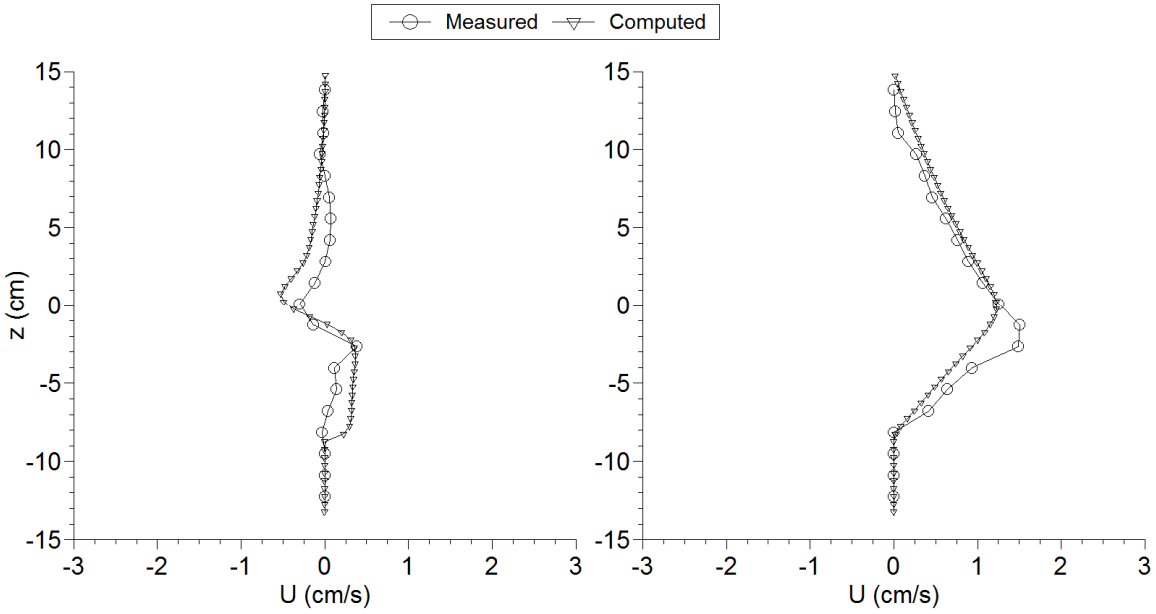

(d) $t / T = 0.75$

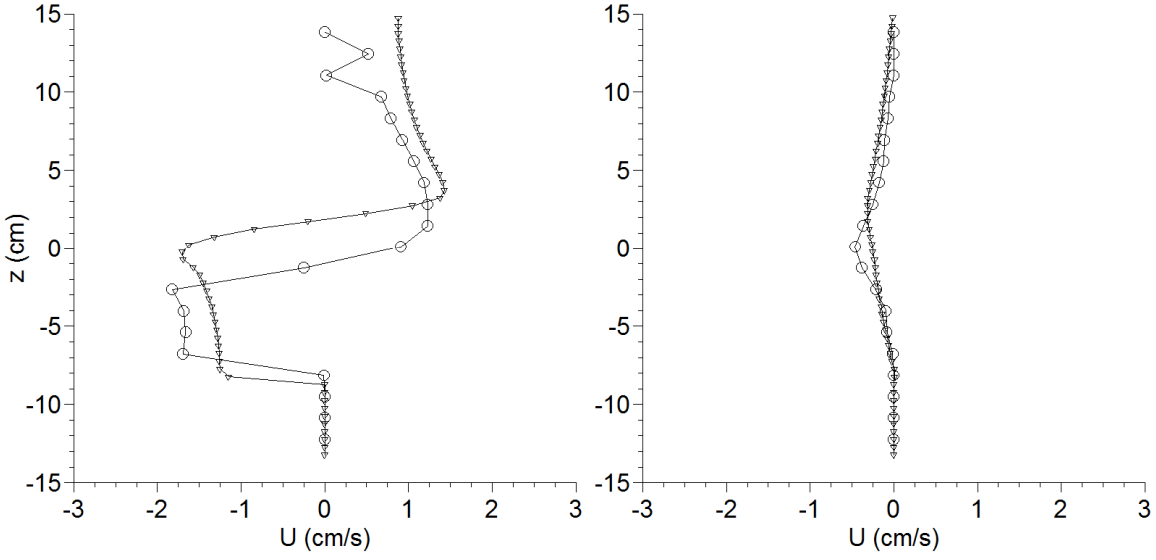

Fig. 4.12 Comparisons between computed and measured velocity components at x = 145 cm for Case S4; U: horizontal component, W: vertical component of velocity

(a) Measured (b) Computed

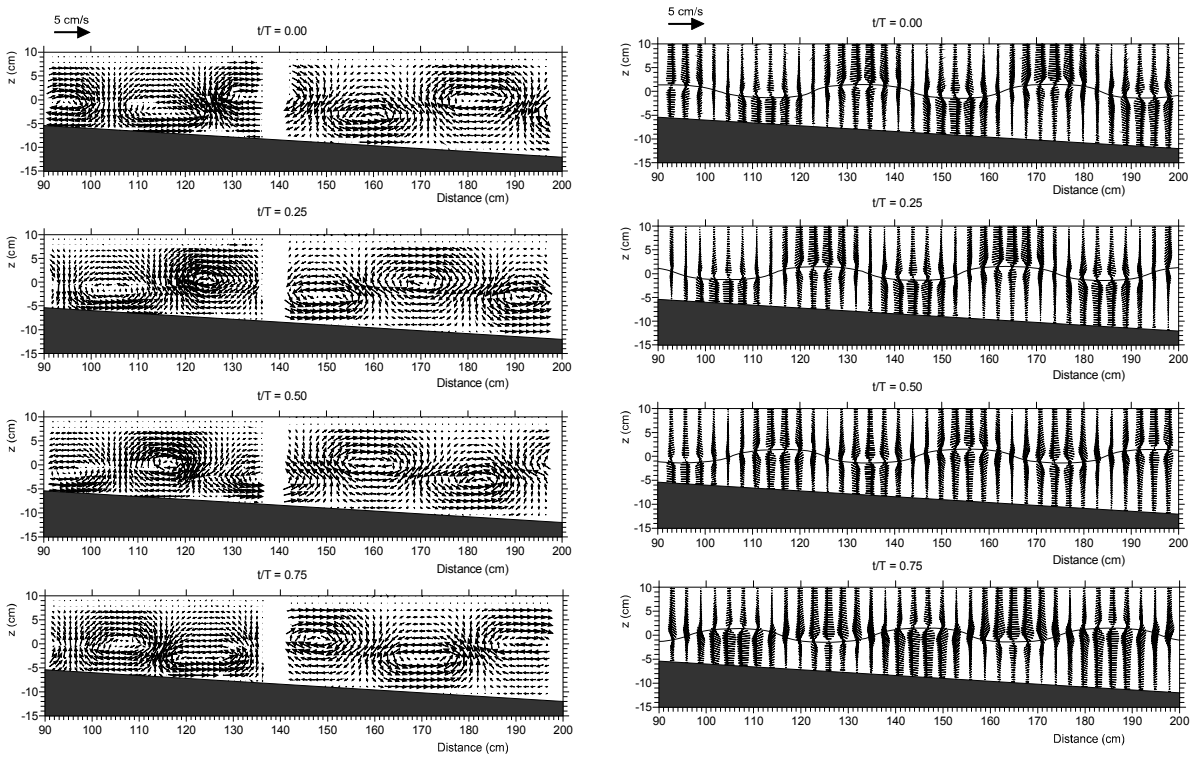

Fig. 4.13 Instantaneous velocity fields of internal waves for Case S5

(a) Measured (b) Computed

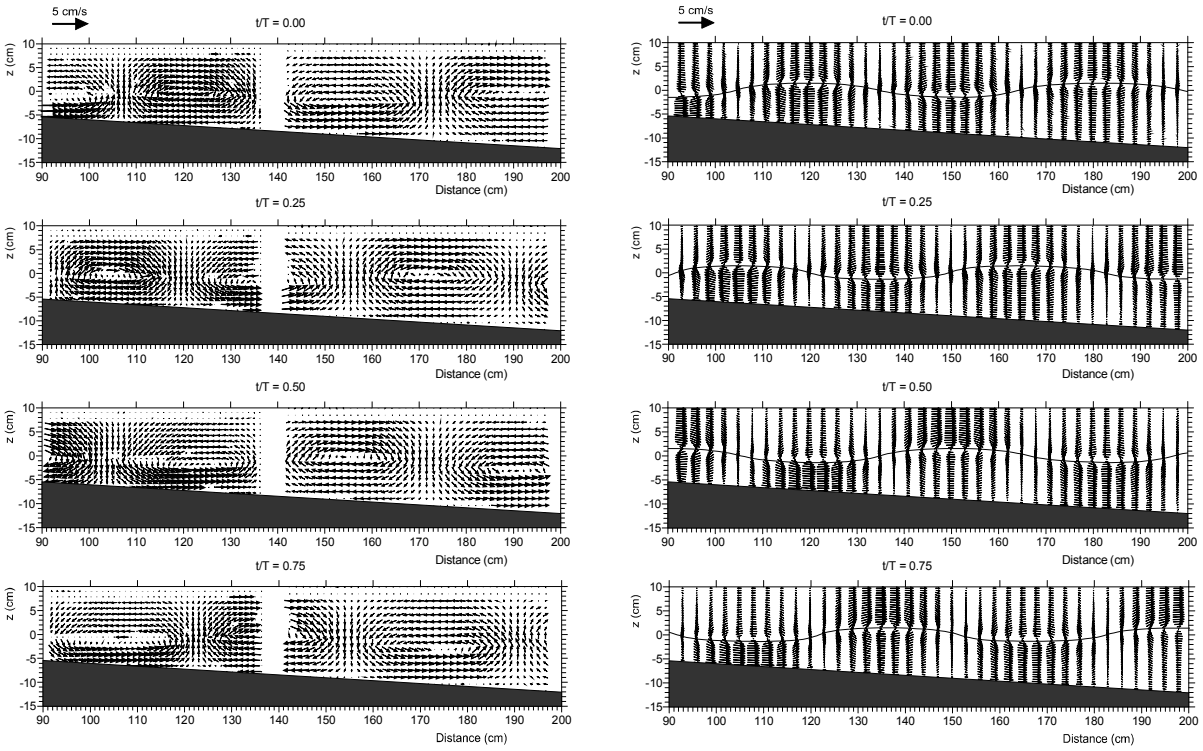

Fig. 4.14 Instantaneous velocity fields of internal waves for Case S6

4.3.4 Water particle trajectory

Fig. 4.15 shows the plots of the measured and computed particle orbit geometries for h_I : h_{II} = 15 cm : 15 cm during three wave cycles for T = 5.2 s (Case S3). **Fig. 4.15 (a)** depicts the water particle trajectories at five elevations at the location of x = 93 cm. The triangle symbol shows a position of water particle estimated from the PIV measurement, and the crossed circle symbol depicts the instantaneous location computed by the numerical model. "h" is the water depth at the given section. In the upper layer, the maximum drift distance of measured particle is about 3 cm while the particle drift near the density interface is approximately 9 cm during three wave cycles. The computed trajectory by the 2D model near the interface is similar to the measured profile. At some elevations in the upper layer, the measured particle path is extended further in the direction opposing to the wave propagation when compared to the computed result. In the lower layer, the computed particle paths are in terrible disorder. Near the interface, the measured particle movement shows a similar trend to the computed one despite the larger drift distance for the experimental once. **Fig. 4.15 (b)** illustrates the water particle trajectories at six elevations at the location of x = 118.5 cm. The water particle moves 3 cm in the offshore direction in the upper layer and 2 cm in the shoreward direction in the lower layer. Near the interface, the drift distance of particle is 7 cm but its rotational direction is opposite to the calculated one. Agreement of PIV data with numerical result supports the existence of the Stokes drift. This result strongly recommends further measures of interfacial displacement in the internal wave tank and calibrated with the numerical model. Water particles move clockwise in the upper layer and anticlockwise in the lower layer. Near the density interface, the horizontal and vertical displacements of the water particle are large relative to those near the surface and bottom regions. The particle marches forward in a large nonclosed loop at the density interface, implying that each particle yields a maximum forward drift.

Fig. 4.16 shows a comparison of measured and computed particle trajectories at x = 106 and 118.5 cm for $h_I : h_{II}$ = 15 cm : 15 cm and T = 7.2 s (Case S4). The water trajectories in the lower and upper layers are predicted well by the numerical model while there is a discrepancy for both particle trajectories near the interface. The measured particle drifts a shorter horizontal excursion compared to that in the lower or upper layer. The computed particles move further in the forward direction near the density interface.

Fig. 4.17 depicts the water particle trajectories in the case of $h_I : h_{II}$ = 10 cm : 20 cm with T = 5.2 s. The initial sections of water particle are x = 114 cm and 169.5 cm. A fair agreement is obtained between experiment and numerical results especially in the pattern of movement. Near the interface at x = 114 cm, the measured particle moves shoreward about 3 cm while the computed particle moves about 4 cm. The particles shift in the offshore direction is noticeable in the lower layer. Near the interface at x = 169.5 cm, the measured

particle moves relatively long distance toward the shore. However, there is a discrepancy between the measured and computed trajectories there. All the particle trajectories are not closed in the total depth. The water particles around density interface tend to move in the direction of the wave propagation while particles in the remaining region travel in the opposite direction because of mass conservation in the closed tank.

Fig. 4.18 illustrates the water particle trajectories for Case S6. **Fig. 4.18** (a) depicts the trajectories at six elevations at x = 126 cm. The measured trajectory shows a discrepancy to the computed ones near the interface. In the upper layer, both computed and measured particles move in the shoreward direction while these in the lower layer move to the offshore direction to maintain the mass balance in the closed tank. In this case, the upper layer is thicker than the lower layer so that the particles near the interface were strongly affected by the interfacial displacement. This trend is not the same as one along the slope. **Fig. 4.18** (b) shows the water particle trajectories at x = 155 cm. At this location, the measured water particles in the upper layer tend to move to the offshore direction while these in the lower layer drift toward the shore. In contrast, the computed particles drift toward the shore in the total lower layer and the offshore in the total upper layer.

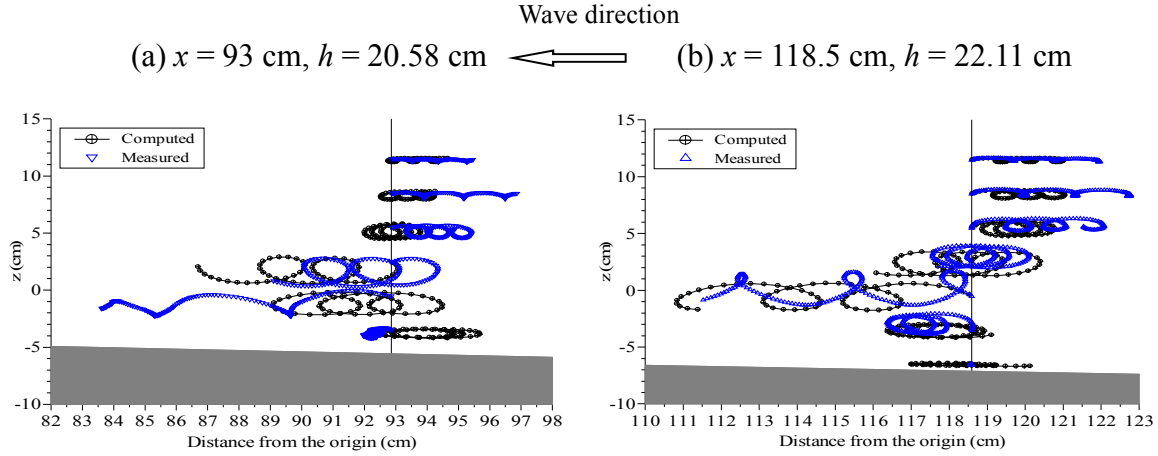

Fig. 4.15 Water particle trajectories for Case S3

(a) x = 106 cm, h = 21.36 cm

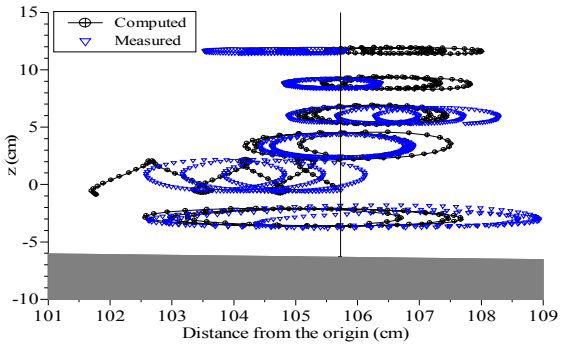

(b) x = 118.5 cm, h = 22.11 cm

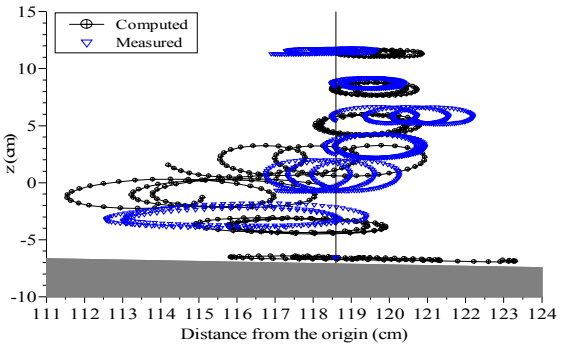

Fig. 4.16 Water particle trajectories for Case S4

(a) x = 114 cm, h = 16.84 cm

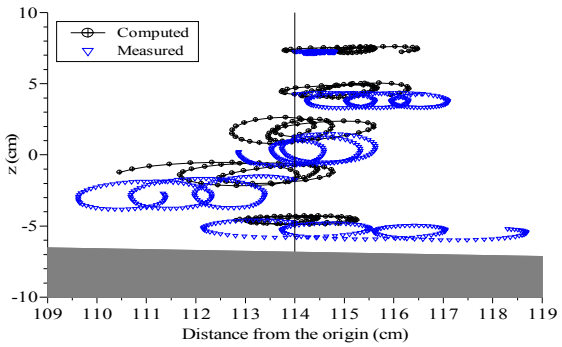

(b) x = 169.5 cm, h = 20.17 cm

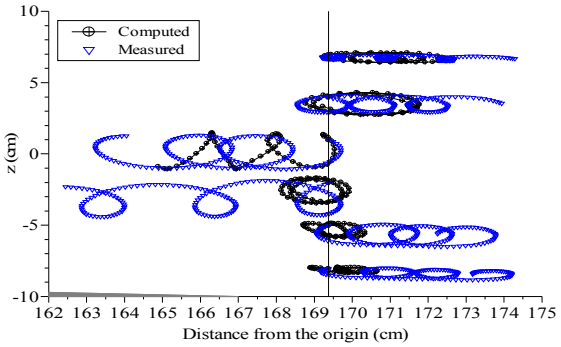

Fig. 4.17 Water particle trajectories for Case S5

(a) x = 126 cm, h = 17.56 cm

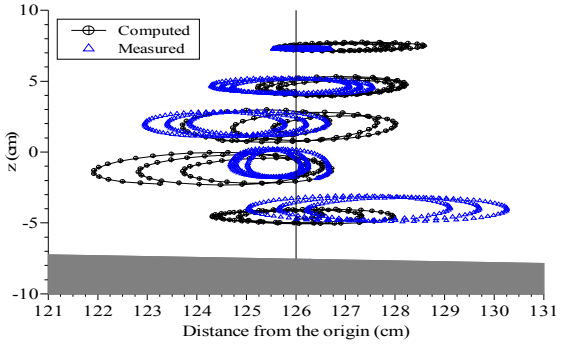

(b) x = 155 cm, h = 19.3 cm

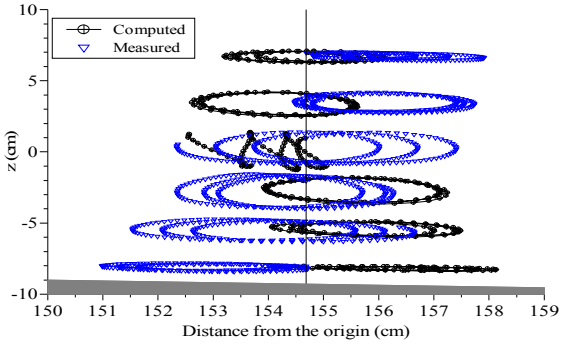

Fig. 4.18 Water particle trajectories for Case S6

4.4. Conclusions

In this chapter, the foundation of numerical method and the experimental and numerical results were presented to understand the physical aspects of internal waves propagating on a sloping bottom in a density-stratified two-layer fluid. The wave celerity was computed using numerical model, light attenuation method based on spatial variations of density interface. The velocity fields have been measured using the PIV technique and computed using 2D numerical model for different wave periods and thickness ratios. The water particle trajectories were investigated using Euler-Lagrangian method that transfers the velocity at the Eulerian grids into the Lagrangian velocity. The agreement between the computed and the measured results was reasonable in interfacial displacement, wave celerity, instantaneous velocity and trajectory. As the result, the numerical model can be applied to investigate the mass transport due to internal waves propagating in a stratified water.

Chapter 5

Mass Transport by Internal Waves Propagating in a Two-Layer Fluid and Effect of Thickness Ratio

Abstract

This chapter presents experimental and numerical investigations for understanding the mechanism of mass transport by internal wave propagation over both a flat bottom and a constant slope in two-layer stratified fluid. The mass transport velocity has been estimated from the horizontal excursion of water particles. The water particle trajectories were obtained from PIV results in a laboratry flume and also computed by a two-dimensional non-hydrostatic numerical model. In this chapter, first the distributions of mass transport velocity for the cases of constant slope are discussed with experimental and numerical results. After that, the numerical model is applied for simulating the mass transport phenomenon in the case of flat bottom. It is confirmed that the numerical model reasonably reproduce the measured wave profile as well as the measured mass transport of the internal waves. A series of numerical experiments showed the dependency of mass transport on layer thickness ratio and wave height. Furthermore, the maximum forward mass transport velocity was found to be highest when the upper and lower layer thicknesses are equal, and it reduces as the thickness of lower layer exceeds that of the upper layer. For all thickness ratios, the mass transport velocity gets larger with increase of internal wave height.

5.1. Introduction

Many field observations prove the ability to transport the mass due to internal wave propagations. When internal waves propagate from offshore to inshore areas, non-linear effects include the advection of fluid particles along with suspended mass such as sediment, nutrients, larvae, as well as contaminants in the direction of wave propagation. Inall et al. (2001) estimated a sustained transport of approximately 0.3 m^2/s due to nonlinear internal waves at the Malin Shelf edge in summer. Wang et al. (2007) observed the frequent drop in daily water temperature up to 8°C due to the intrusion of large nonlinear internal waves at Dongsha Atoll. They highlighted the effect of internal waves on nutrient circulation in a tropical reef ecosystem. Shroyer et al. (2010) conducted observations over New Jersey's shelf and estimated the month-averaged daily onshore transport by nonlinear internal wave propagation to be approximately 0.3 m^2/s. The distribution of mass due to the transportation by internal waves from offshore to onshore waters is still not well documented. Therefore, the mass transport along a constant slope is discussed in the first part of this Chapter.

As described in Chapter 2, the phenomenon of transport due to internal wave propagation has been analytically considered by Dore (1970). He introduced an analytical solution for the mass transport velocity due to small amplitude oscillatory waves and found that the velocity at the interface is in the direction of progressive wave propagation. Dore (1973) also got the same result by using the curvilinear coordinate system to describe the motions in the interfacial boundary layers. Later, Wen and Liu (1995) investigated the mass transport with the effect of viscous damping which was ignored in both of Dore's papers (1970, 1973) for a two-layer fluid system. They found that the effect of the viscous damping plays an important role in estimating mass transport velocities. There are some studies related to mass transport due to internal waves that confirmed that mass is transported inshore mostly at the interface (Dore, 1970; Nguyen et al., 2012). In oceans and lakes, it is possible to assume the density structure as a two-layer system. However, the thickness of well mixed upper layer is changing due to the magnitude of Sun radiation and surface conditions. **Fig. 5.1** shows an example of the change of temperature profiles monthly in the Northern Hemisphere. In the middle latitudes, the thickness ratio of upper layer to lower layer decreases from winter to summer. From offshore to onshore water, this ratio increases due to the shallow of lower layer. Although the fundamental property of the mass transport is relatively recognized, the effects of layer thickness ratio and nonlinearity of internal waves on the mass transport are not investigated so far. These effects are essential for understanding the transport process and distribution of suspended particles in real situation.

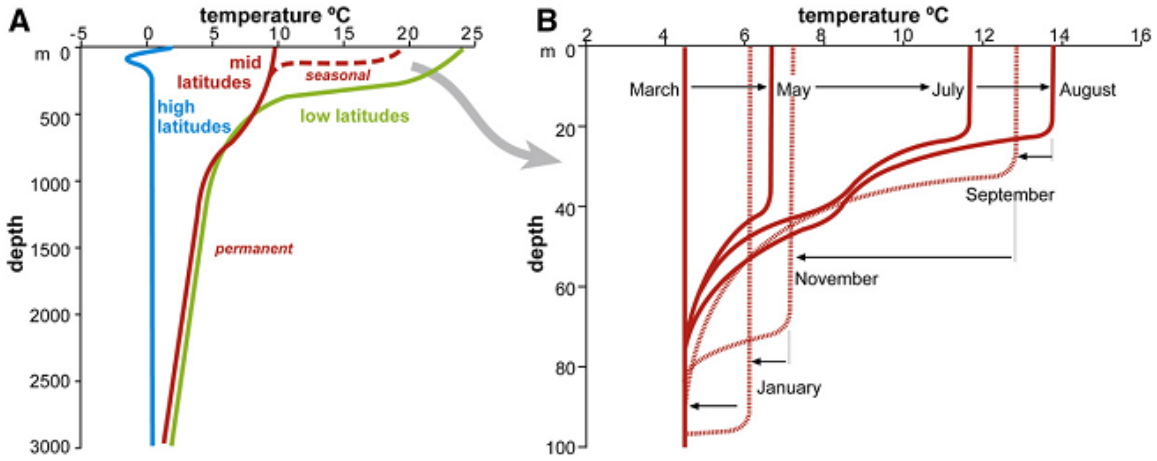

Fig. 5.1 Typical temperature/depth profiles in open oceans (From Pomar et al, 2012): (A) Mean temperature profile for different latitudes; (B) Succession of temperature profiles showing the growth and decay of seasonal thermocline in the Northern Hemisphere

5.2. Mass transport due to the propagation of internal waves over a constant slope

The mass transport velocity can be estimated from the horizontal movement of the water particle within one wave cycle. The mass transport velocity is computed from the excursion of particles. These particles are added to the computing process as the wave profile becomes stable as follows:

$$U_m = \frac{1}{T}\int_0^T u(x(t), y(t))dt \tag{5.1}$$

where U_m is the mass transport velocity; T is the wave period; $u(x(t), y(t))$ is the instantaneous velocity; t is time; $x(t)$ and $y(t)$ are horizontal and vertical coordinates, respectively.

The displacement of particle is computed as

$$x(t) = x_0 + \int_0^\tau u(x(t), y(t))dt \tag{5.2}$$

$$y(t) = y_0 + \int_0^\tau v(x(t), y(t))dt \tag{5.3}$$

where x_0 and y_0 are initial horizontal and vertical coordinates, respectively.

Finally, Eq. (5.1) can be written as

$$U_m = \frac{x(T) - x_0}{T} \tag{5.4}$$

Fig. 5.2 and **Fig. 5.3** show the vertical distributions of averaged mass transport velocity for Cases S4 and S6, respectively. **Fig. 5.2** (a) depicts profiles of measured mass transport velocity at x = 93, 106, 119, 133.5, 147, and 160 cm for T = 7.2 s. The internal waves tend to transport water in the direction of wave propagation in the upper part of the interface. In the lower layers, the waves transport water in the opposed direction to conserve the mass and due to the return gravity current. When the internal waves propagate on a slope, they might break and generate the boluses of dense water. These boluses continue run up to slope due to inertia. At a level, they stop and go down the slope due to the gravity. The maximum value of shoreward mass transport velocities is approximately 0.25 cm/s. This velocity is 10-30% of the water particle velocity. The transport velocity profiles are varied along a slope without an apparent tendency. **Fig. 5.2** (b) depicts the corresponding mass transport velocity computed by the 2D model. It should be noted that patterns of computed mass transport velocity doesn't show a similar trend. The maximum shoreward velocity is also approximately 0.25 cm/s. The computed maximum shoreward values agree well with the measured data. However, the profiles of computed and measured velocity are especially different in the lower layer. Inspecting the measured data, it appears that the effect of returning flow was significantly large whereas in the computed results, it was quite small. The computed profiles are similar to those as per theoretical distributions by Dore (1970).

(a) Measured (b) Computed by 2D model

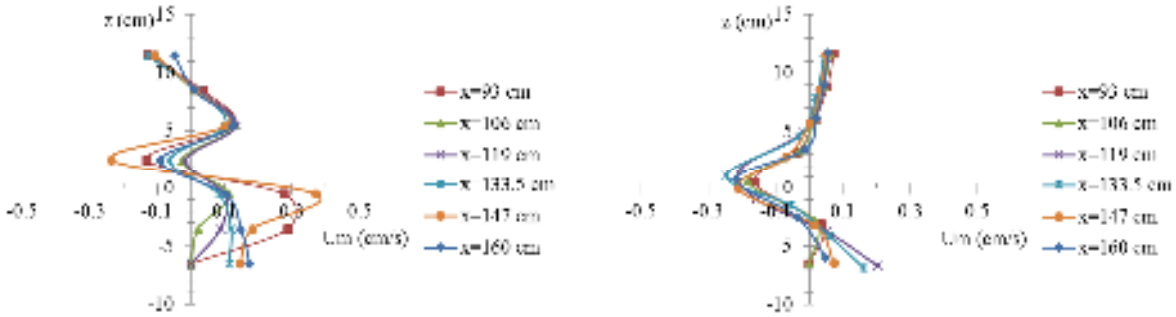

Fig. 5.2 Profiles of mass transport velocity for Case 4

(a) Measured (b) Computed by 2D model

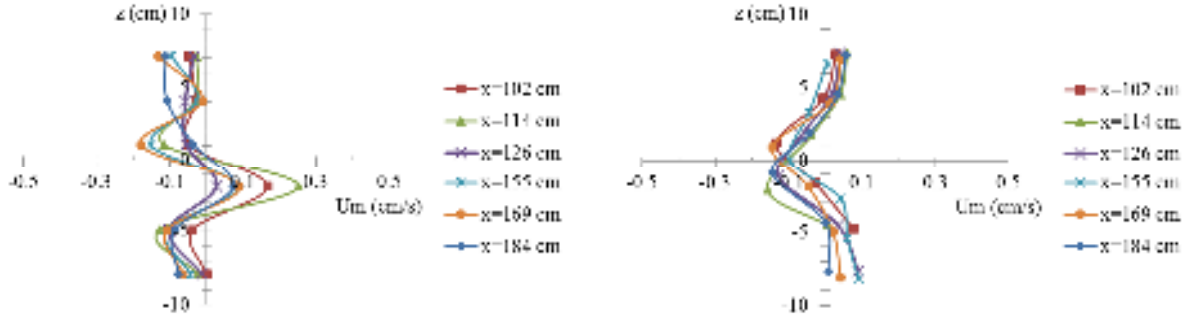

Fig. 5.3 Profiles of mass transport velocity for Case 6

Fig. 5.3 (a) depicts similar profiles of measure mass transport velocity for $h_I : h_{II}$ = 10:20 cm with T = 7.2 s at six locations. In this case, the measured mass transport velocity is negative in the upper part of lower layer. These values are negative at z = 0 cm and z = -4 cm but positive in the remaining regions. **Fig. 5.3** (b) shows the computed mass transport velocity for the same locations. The elevation of computed maximum velocity varies along the slope. Once again, the computed results agree with data measured in the maximum shoreward mass transport velocity. The measured and computed results confirm that the mass is transported to the shoreward direction near the density interface. However, the difference between the distributions of mass transport velocity profile is quite noticeable. Although the numerical model can simulate the interfacial displacement very well, wave celerity, instantaneous velocity and the order of maximum shoreward mass transport velocity but the tendency of mass transport is still not satisfactory. This discrepancy suggests and motivates the author to consider the effect of the diffusive transition layer. In the numerical method, it is possible to control the interfacial layer thickness but in the experiments it is not so easy owing to the diffusive nature of fluid. Further investigation of this difference is presented in Chapter 6.

The spatial distributions of mean mass transport velocity are considered for different thickness ratios and wave periods. Mass transport velocity was computed at seven locations, x = 200, 160, 120, 80, 40, 20, and 0 cm. **Fig. 5.4 - 5.7** depict the profiles of mass transport velocity for cases S3–S6, respectively. In the deeper part, i.e., x > 100 cm, the velocity is negative in the range of z = –5 to 5 cm. This means that internal waves transport the mass shoreward around the interface. This velocity is 10 - 30% of the maximum particle velocity at the same location. In this case, the vertical profiles of mass transport velocity vary toward the

origin. Near the origin, the water particle has long excursion because of the backwash from the upper slope. It seems that in the upper part of interface the mass transfers up the slope while in the lower part it flows along the sloping bottom. This movement is quite similar to gravity currents or bolus that are generated after breaking (Venayagamoorthy and Fringer, 2007). In the offshore region on the slope, the profiles of mass transport are quite similar to the theoretical profile which proposed by Dore (1970) (**Fig. 2.4**). However, it should be noted that the mass transport at the interface does not get maximum value as Dore's result. They apparently transport with smaller velocity at the interface than the adjacent regions. This strange phenomenon led the author to pay more attention to the transition layer between two homogeneous layers.

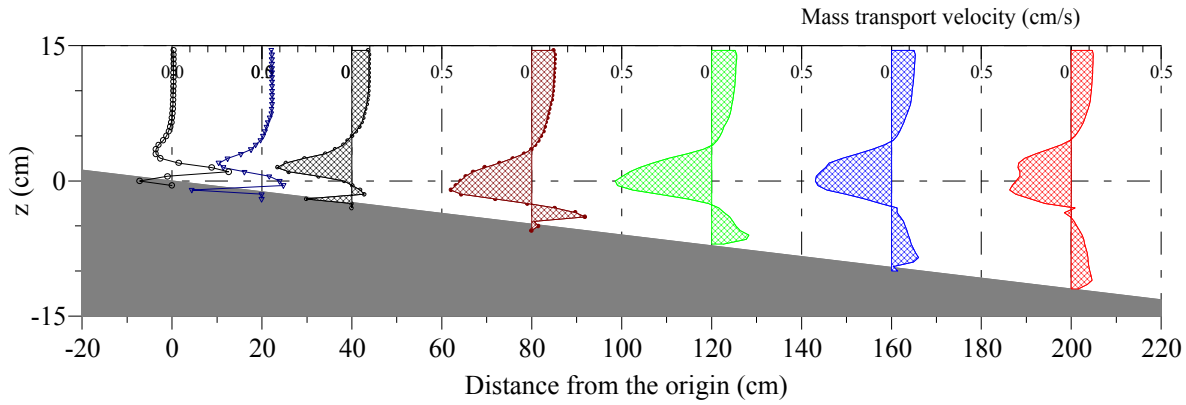

Fig. 5.4 Distributions of mass transport velocity along the slope for Case S3

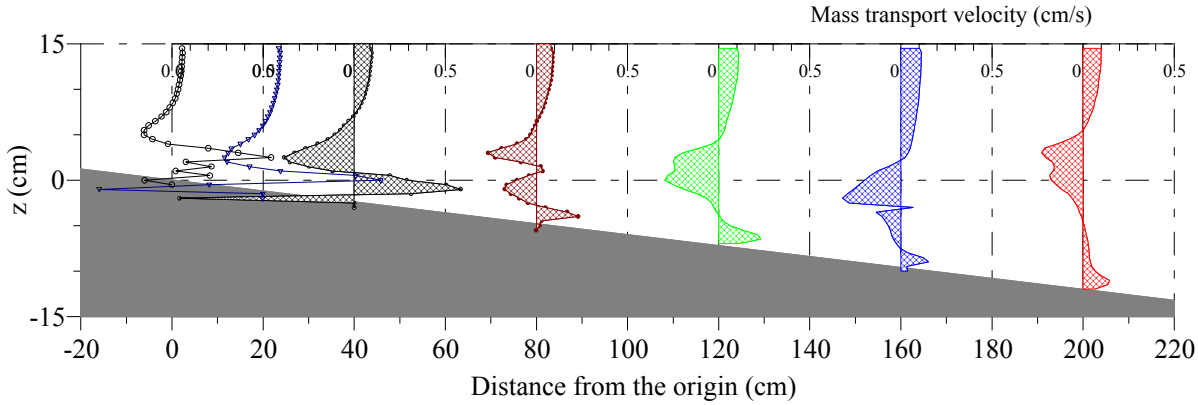

Fig. 5.5 Distributions of mass transport velocity along the slope for Case S4

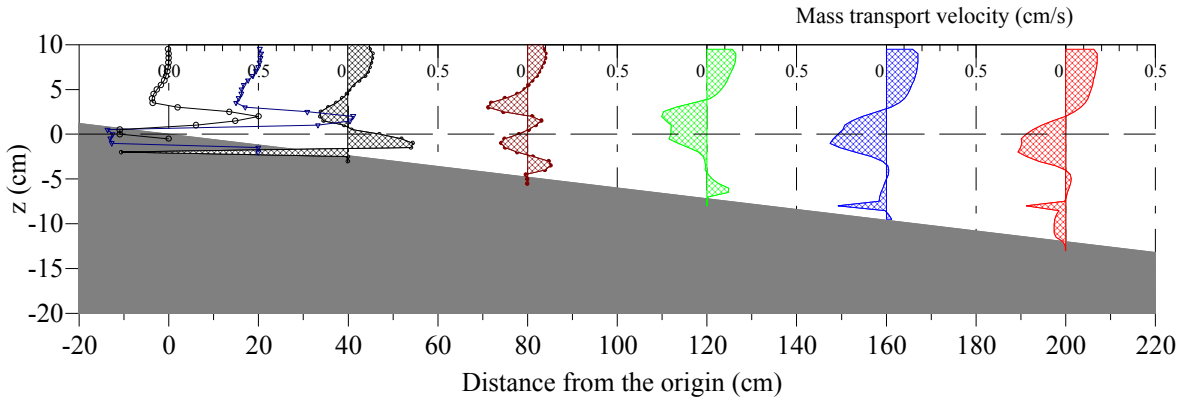

Fig. 5.6 Distributions of mass transport velocity along the slope for Case S5

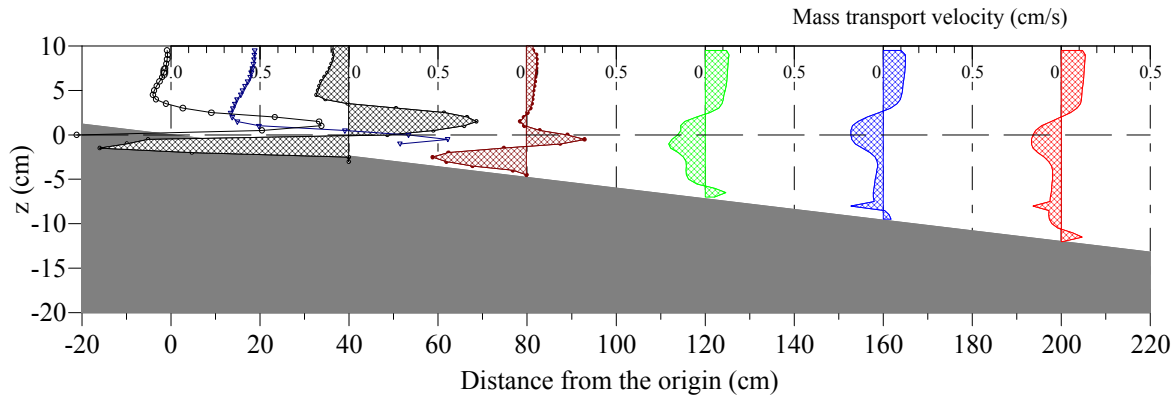

Fig. 5.7 Distributions of mass transport velocity along the slope for Case S6

While wave celerity decreases gradually toward the origin, the effect of bathymetry on wave height and wavelength increases. For deep water, wave steepness is indicative of wave transformation and a criterion for wave breaking. For shallow water, many authors have conveniently expressed the fictitious surface wave steepness as the ratio of the local wave height and wavelength (Heineke and Verhagen, 2007). In this study, a similar definition will be applied to internal waves. The fictitious steepness (γ) of an internal wave is defined as the ratio of the instantaneous wave height (h) and wavelength (L) over the slope (as shown in **Fig. 5.8**). Battjes (1974) discussed it, combining the fictitious wave steepness with the bottom slope to describe the surface wave breaking. The aim of the present approach is to discuss how wave steepness affects mass transport. **Fig. 5.9** shows the distributions of fictitious steepness in the cases S3 and S4. In **Fig. 5.9** (a), the steepness is maintained at 0.065 from x = 120 cm to x = 180 cm, and then it gradually increases to 0.08 at x = 32 cm. The wave steepness increases abruptly from γ = 0.042 to 0.11 in **Fig. 5.9** (b). A different tendency can

be seen in **Fig. 5.10** that depicts the wave steepness distributions for the case of $h_I : h_{II}$ = 10 cm : 20 cm. The tendency of the steepness is very clear in the case S5. In this case, wave steepness is almost constant $\gamma = 0.05$ in the range $x > 100$ cm, increases to $\gamma = 0.12$ at $x = 40$ cm, and then starts to decrease toward the origin. The maximum fictitious steepness might give a criterion to determine an interfacial breaking point. Note that the maximum mass transport velocity becomes faster where the fictitious steepness starts to decrease.

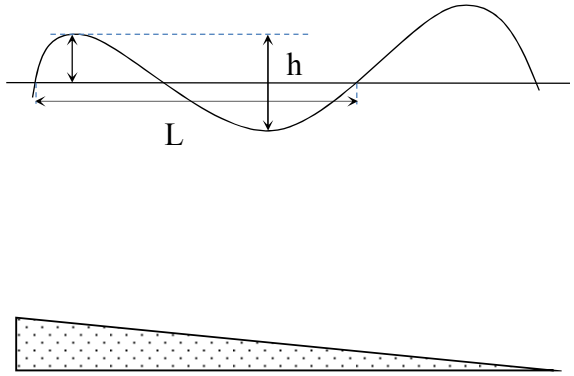

Fig. 5.8 Internal wave height and wavelength

(a) T = 5.2 s (b) T = 7.2 s

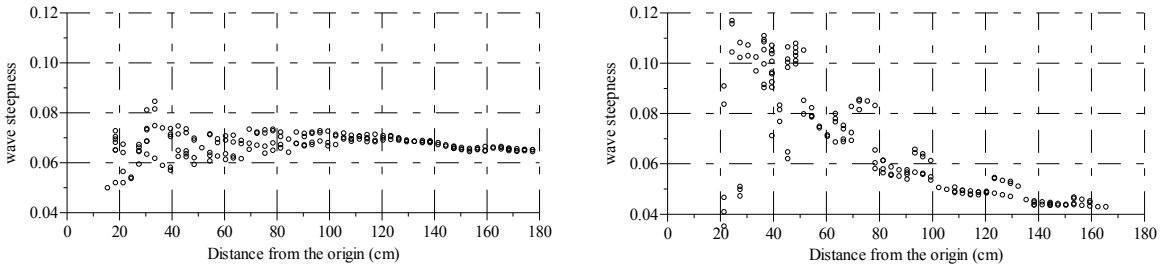

Fig. 5.9 Distributions of fictitious internal wave steepness for Cases S3 and S4

(a) T = 5.2 s (b) T = 7.2 s

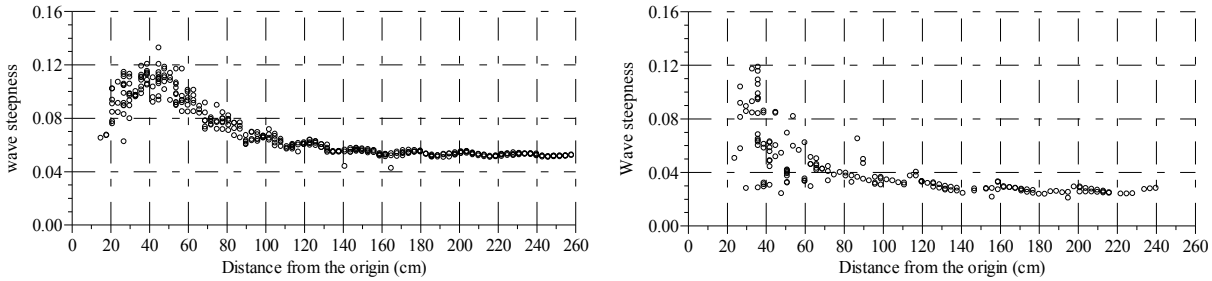

Fig. 5.10 Distributions of fictitious internal wave steepness for Cases S5 and S6

5.3. Effect of thickness ratio on mass transport due to internal waves propagating over a flat bottom

To investigate the effect of thickness ratio between upper layer to lower layer on mass transport, laboratory experiments and numerical simulations having different thickness ratios, wave heights and periods (**Table 2**) have been carried out in two-layer density stratified water. The numerical model was used to simulate the particle trajectory and the mass transport for flat bottom case. A series of numerical experiments (**Table 3**) were employed to investigate the dependency of mass transport to wave height then consider the effect of thickness ratio.

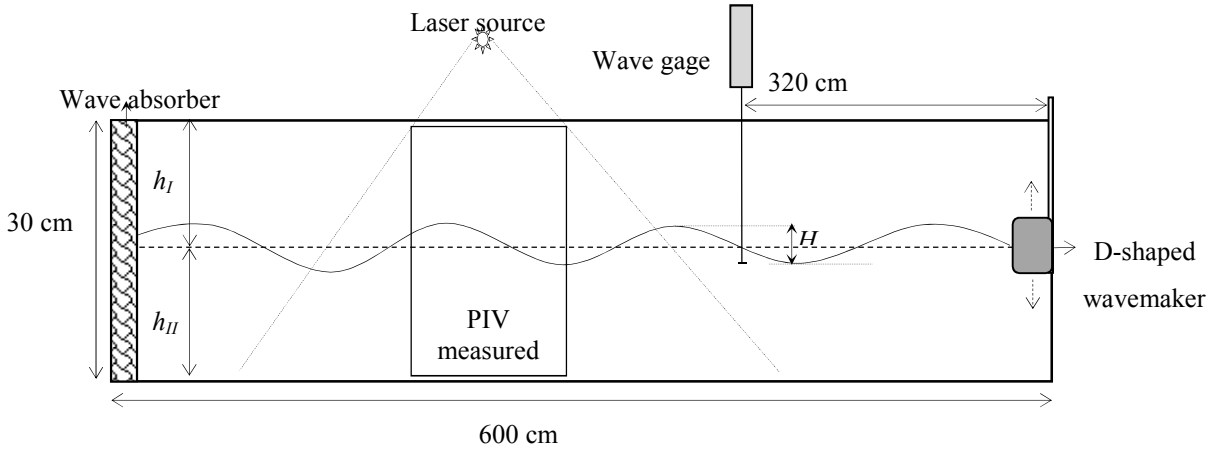

Fig. 5.11 Sketch of experimental setup

The same procedures and techniques for the constant slope were applied to the experiments with a flat bottom. An internal-wave gauge was set at 320 cm from the wavemaker to measure interfacial displacement. A wave absorber was placed at the other end of the flume to diminish the reflected wave (**Fig. 5.11**).

Before discussing the mass transport using measured and computed results, the accuracy of the numerical model was tested using experimental results. **Fig. 5.12** shows a comparison between the computed and measured interfacial displacements for the case F3. In experiments, the wave absorber at the one side of wave flume dissipates the wave energy to avoid the reflected wave. However, in the numerical computations, no wave absorber was designed, therefore the waves were considered before the reflected wave propagated back to the center of the flume. Inspecting **Fig. 5.12**, the computed results are in good agreement with the measured data. It shows that the 2D model could reproduce well the internal wave mechanics in laboratory wave tank. As the accuracy of the present numerical model was confirmed, numerical experiments have been carried out for understanding the kinematics of internal waves in two-layer system. **Fig. 5.13** depicts computed and measured water particle trajectories at x = 300 cm for the case F3. The internal waves propagate from right to left. The blue triangle and open circle symbols show the measured and computed data for three wave cycles, respectively. The particles at the interface move in the direction of wave propagation while those in remaining parts move in the opposing direction. This tendency coincides with the measurement by Umeyama and Matsuki (2011). Water particles in the upper layer move clockwise whereas those in the lower layer move anti-clockwise. The computed and measured particle orbits are quite similar at all elevations in magnitude and tendency. The computed results show that particles near the interface skip in the propagating direction with the longest distance. It means that the mass has been transported significantly near the interface. Near the interface the particles travel with unclosed elliptic orbits and the minor radius of these elliptic orbits become smaller toward the free surface and bottom. Close to these boundaries, the particles slip back and forth with smaller excursions than those near the interface.

Fig. 5.14 plots a comparison between measured and computed mass transport velocities for the same case with **Fig. 5.13**. The mass transport velocity is calculated as a ratio of horizontal excursion and travel time of the particles. In the experiment, internal waves transport the mass toward the propagating direction in the range $z = -2$ cm to 6 cm while in the numerical simulations they transports from $z = -2$ cm to 3 cm. The measured mass-transport velocities near the surface and bottom are faster than the computed ones. The maximum values of transport velocities can be seen for other laboratory experimental cases as shown in **Fig. 5.15**. Internal waves transport the mass significantly near the interface between two layers. Now, we concentrate on the relation of maximum mass transport near the

interface with the thickness ratio. The relationship between mass transport and wave height was also considered.

Fig. 5.16 is a sketch depicting the movement of a particle and its corresponding parameters. Variable a denotes for maximum forward horizontal excursion of initial particle near the interface (z = 0 cm) after three wave cycles. H is the height of internal wave. To investigate the relationship between the maximum mass transport velocity near the interface and the wave height, a series of numerical experiments have been carried out with different wave heights for the period of T = 5.2 s. **Fig. 5.17** shows the computed results of maximum shoreward mass transport velocity versus wave height. The velocity increases almost linearly with the wave height for all thickness ratios. As the mass transport velocity should be vanished in the case of H = 0, the relationship $V_{mass} = f(H) = kH$ could be found from the computed results. Where $V_{mass} = a/(3T)$ is the maximum mass transport velocity near the interface, k is a proportional constant. The trend is quite similar for other thickness ratios. It confirms that the maximum mass transport velocity near the interface strongly depends on wave height although it might be affected by density difference, wave period etc. Based on this relationship, the effect of thickness ratios to the mass transport can be further investigated without amplitude effect by considering the ratio of $a/H \sim f(H)/H$. **Fig. 5.18** depicts the relations between a/H and the value of thickness ratio (h_I / h_{II}) for different wave periods. The solid dot symbols show the computed results for the wave period of T = 7.2 s, while the solid triangle symbols depict for T = 5.2 s. The solid and dash lines show the trend of the data with corresponding regression equations. Please note that, in deeper parts of oceans and lakes, thickness of the upper layer is usually smaller than that of the lower layer. Therefore, in this investigation the thickness ratios are smaller or equal to 1 ($h_I / h_{II} \le 1$). For different periods, the ratio a/H increases with increasing of thickness ratio. It proves that the maximum mass transport velocity is larger for the linear case ($h_I = h_{II}$) and decreases as thickness of lower layer (h_{II}) increases.

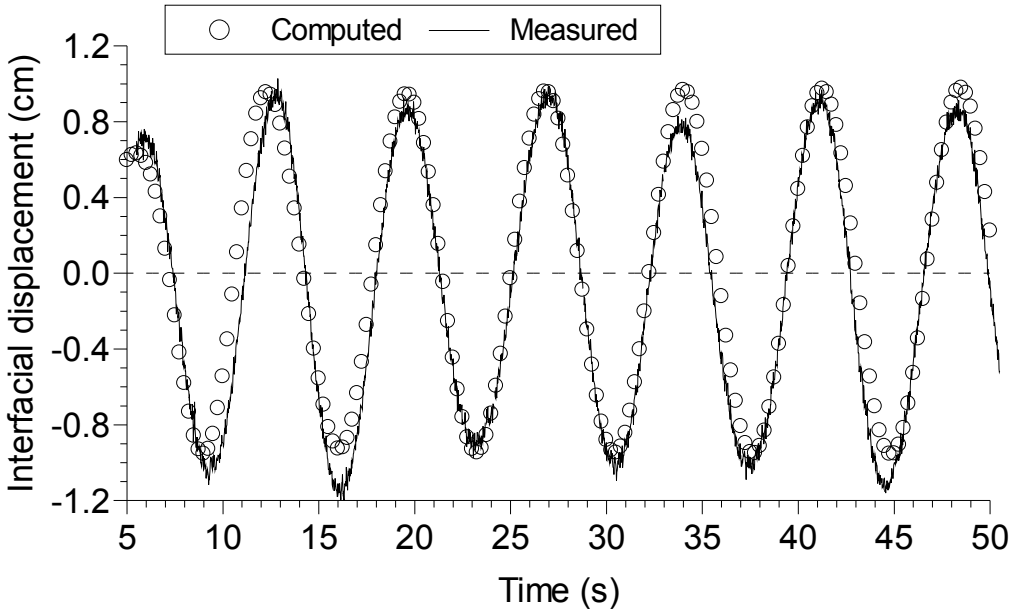

Fig. 5.12 Comparison between computed and measured interfacial displacements for Case F3

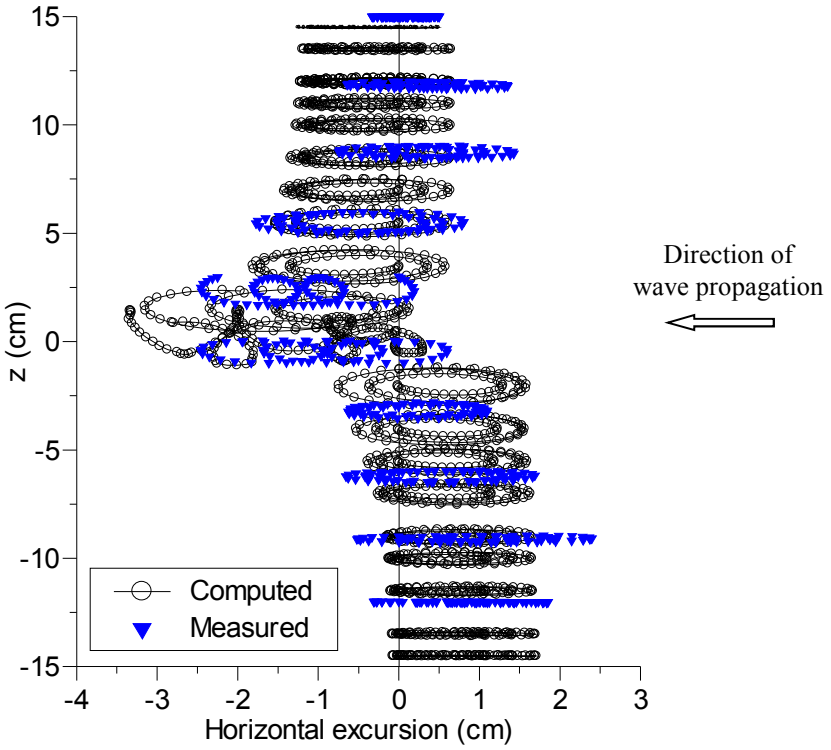

Fig. 5.13 Particle trajectories for Cases F3 and CF3

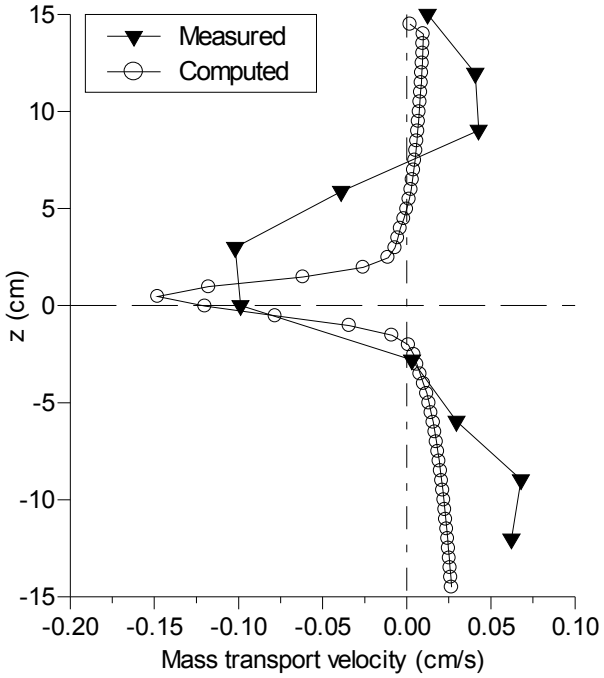

Fig. 5.14 Profiles of mass transport velocity for the Cases F3 and CF3

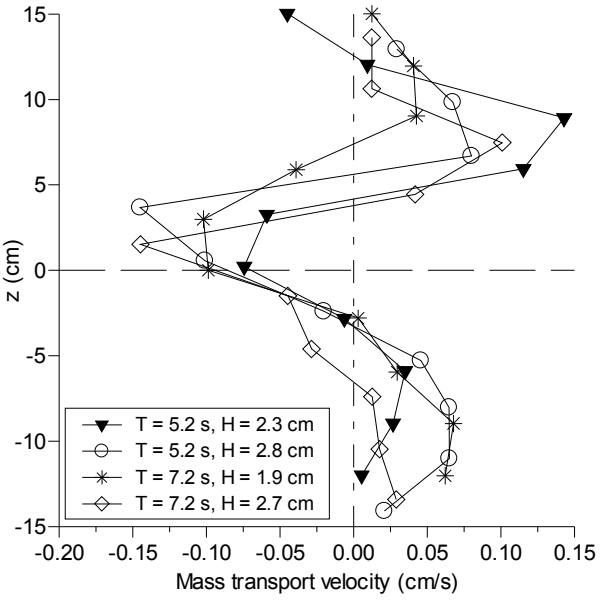

Fig. 5.15 Measured mass transport velocities for the Cases F1-F4

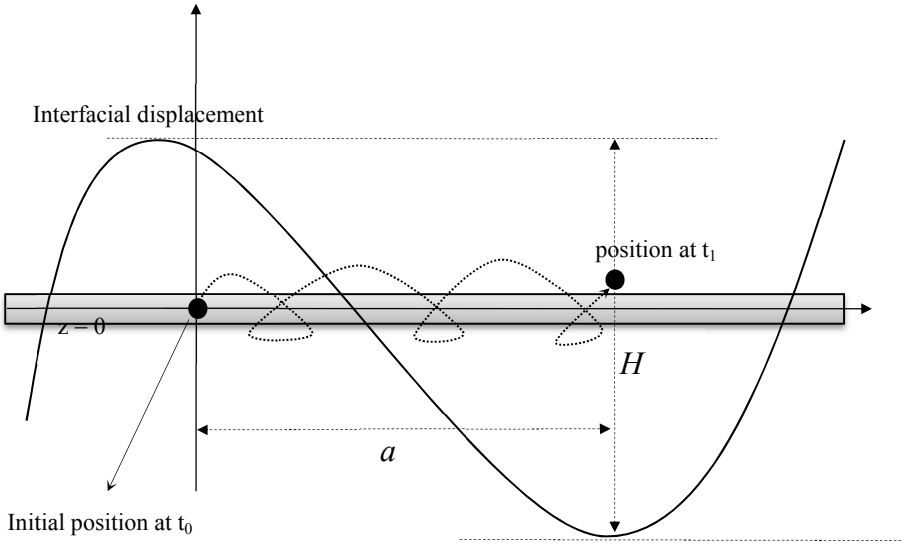

Fig. 5.16 Sketch of water particle movement

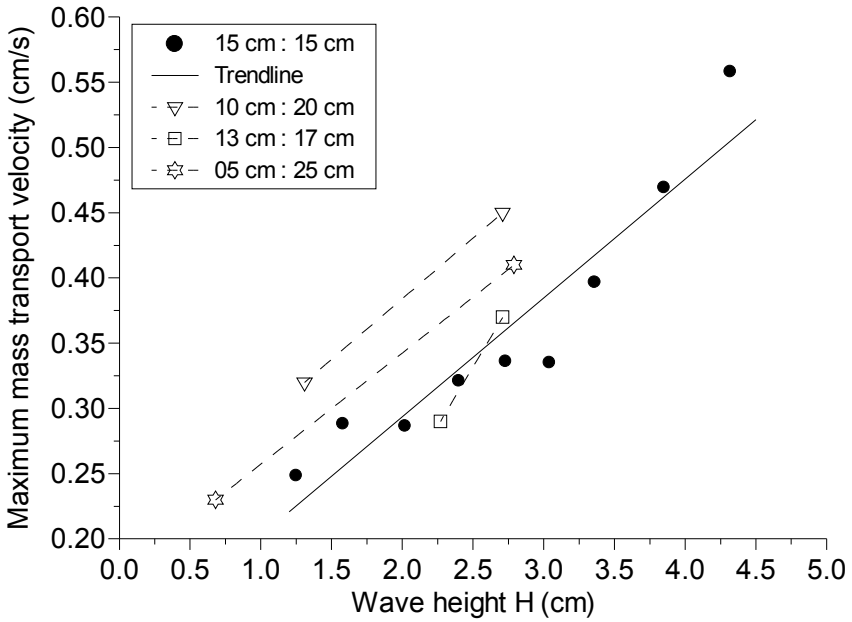

Fig. 5.17 Variation of maximum shoreward mass transport velocity near the interface with internal wave height (H) for T = 5.2 s

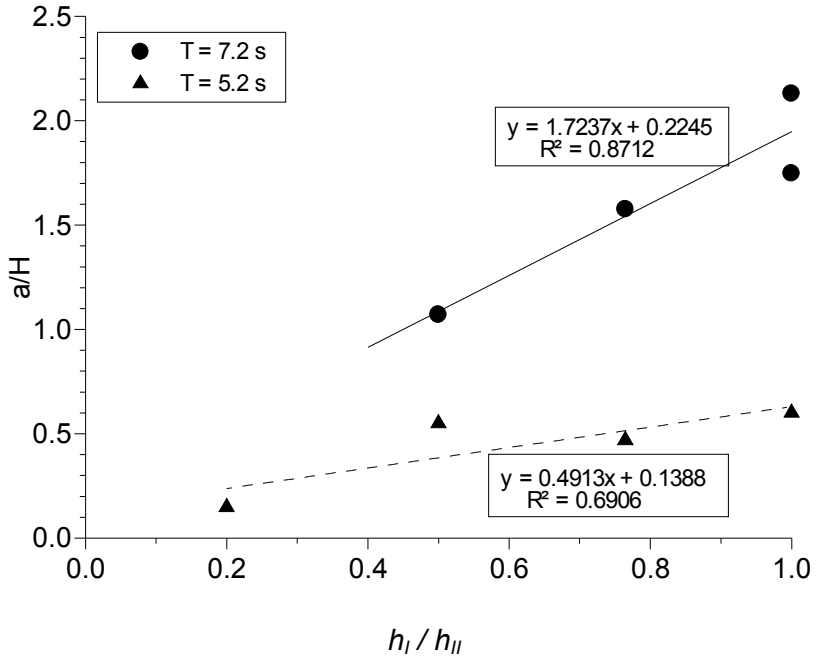

Fig. 5.18 Variations of the ratio of maximum horizontal excursion and wave height for different thickness ratios.

5.4. Conclusions

This chapter presented an investigation of mass transport due to the propagation of internal waves over a gentle slope and a flat bottom in a two-layer fluid system. For the cases of a constant slope, the internal waves transport mass with maximum forward velocity in the shore direction near the density interfacial layer. The mass transport velocity decreases toward the sloping bottom or surface. The fictitious wave steepness, originally defined for surface waves, was adapted to internal waves. The fictitious wave steepness increases along the slope, becomes a peak at a certain point, and decreases toward the origin. In the region where the steepness decreases, mass transport velocity becomes stronger. It can be confirmed that the internal waves play an important role in mass transfer especially in the interfacial region. For the cases of a flat bottom, numerous experimental and numerical investigations have been carried out for understanding the relationship between maximum mass transport velocity near the interface and wave height and thickness ratio. This study confirmed that the internal waves transport the mass in the direction of wave propagation near the interface and in the opposing direction in the remaining elevations. The mass transport by internal waves increases with the increase of the thickness ratio between two layers in the stratified fluid. The mass transport gets its maximum value when the thicknesses of two layers are equal.

This conclusion is very important for understanding the mass transport in the offshore water where density structure was assumed as a two-layer system. The mass transport velocity varies proportionally with the wave height for each thickness ratio. However, more measurements and numerical simulations should be examined to find the universal relationship between the mass transport and the wave height, water depth, and wave period.

Chapter 6

Effects of Diffusive Transition Layer on Mass Transport by Internal Waves Propagating in a Density-Stratified Water

Abstract

This chapter presents results from numerical and experimental investigations into mass transport driven by periodic internal waves in a two-layer fluid system. The experiments concentrate on particle transport inside the interface and its adjacent regions. A series of numerical experiments were carried out for different interfacial thicknesses. The mass transport velocity was found that it does not reach a maximum at the center of the interface but at the two boundaries between the interface and the layers. For a thin interface, particles near the interface travel in the direction of propagating waves. However, as the interfacial thickness increases, particles in the interfacial layer might remain stationary or they may move back offshore, against propagating waves. Experiments with dye-streak method were designed and performed to verify the computational results and quantify the mass transport. These experiments enabled to visualize the tendency of mass transport and provided the temporal and spatial variations of mass transport in the laboratory tank.

6.1. Introduction

With the development of recent measurement techniques, observations of internal waves have revealed their ability to transport and redistribute nutrients, sediments, and larvae as the internal waves propagate into near-shore waters. According to Shanks (1983, 1985,

1986, and 1987), Jillett and Zeldis (1985), Kingsford and Choat (1986), and Shanks and Wright (1987), internal-waves transport the larvae of coastal invertebrates, flotsam, and fishes toward shore. Shanks (1985) observed a mechanism for the onshore migration of planktonic larvae of coastal organisms by shoreward internal-wave transport. The field measurements of Leichter et al. (1996) on Conch Reef, Florida Keys, recorded temperature drops of up to 5.4°C and salinity increases of up to 0.6‰ in 1–20 min owing to the arrival of internal bores. Later, Lamb (1997) considered the transport of water particles under nonbreaking solitary internal waves. It was found that significant particle transport occurs only when the waves are near the breaking amplitude or when they are very long.

Recently, Inall et al. (2001) estimated a sustained transport of approximately 0.3 m^2/s due to an attack of nonlinear internal waves at the edge of the Malin Shelf in summer. Wang et al. (2007) observed frequent drops in daily water temperature of up to 8°C due to intrusions of large nonlinear internal waves at the Dongsha Atoll. They highlighted the effect of internal waves on nutrient circulation in a tropical reef ecosystem. Shroyer et al. (2010) estimated the month-averaged daily onshore transport of about 0.3 m^2/s by nonlinear internal-wave propagation over New Jersey's shelf.

When internal waves propagate from offshore to onshore waters, they affect the advection of fluid particles, suspended sediments, nutrients, larvae, and contaminants. Mass transport driven by propagation of internal waves in a two-layer fluid system has been studied analytically by Dore (1970, 1973). Dore's solution for the mass transport velocity was based on small-amplitude oscillatory waves. At the interface, water particles moved in the same direction as that of wave propagation. Later, Wen and Liu (1995) investigated mass transport with viscous damping, which was ignored in both of Dore's papers for a two-layer fluid system. They found that viscous damping plays an important role in estimating mass transport velocities.

Nguyen et al. (2012) considered the transport of particles along a constant slope by experiment using a 6-m-long wave tank and by calculations using a 2D numerical model. We found that the trend in the vertical mass-transport distribution is very similar to that of Dore (1970, 1973). Both results show that mass transport reaches a maximum near the interface. However, the elevation at which the mass transport velocity reaches maximum was not the same in each run. In contrast, several investigations and observations have assumed a water column that consists of a well-mixed upper layer, a homogeneous bottom layer, and a thin region between the two (Wessels and Hutterm 1996; Michallet and Ivey, 1999). It should be noted that in oceans and lakes, there is a diffusive interface of finite thickness between two homogeneous layers. Huttermann and Hutter (2001) discussed how the thickness of the interfacial layer affects solitary wave height and speed. A finite interfacial thickness might play an important role in the transport of suspended mass, such as nutrients, phytoplankton,

and larvae, and it might explain why the maximum in mass transport velocity may sometimes not occur at the interface elevation. Therefore, in this study, the transport of water particles inside the interfacial layer and adjacent regions is investigated using a numerical model having very high resolution. The author have applied the model to mass transport in periodic internal waves over a flat bottom and a bottom with uniform slope. After that, the series of experiments were performed with the dye-streak method to confirm the computed results in tendency and quantity of mass transport.

6.2. Computational model and procedures

In the model, rigid lid and slip conditions were applied at the water surface. The non-slip condition was applied to wall boundaries, including the slope and bottom boundaries. The internal-wavemaker was positioned at one end of the flume. Two periodic fluxes with different directions of movement were applied to the two layers, as described in Chapter 4. The computational domain was 600 cm in the x-direction and 30 cm in the z-direction. The velocity and density distributions were computed in the entire flume with spatial resolutions of Δx = 1.5 cm and Δz = 0.25 cm and a time step of Δt = 0.001 s. In all cases, the water depth was maintained constant at $h_I + h_{II} + d =$ 30 cm. Mass transport was analyzed based on Lagrangian tracking of particles distributed across the interface with a resolution of 0.1 cm. Mass transport was estimated from computed data as the ratio of horizontal particle excursion to its travel time. Particle excursion was taken to be the horizontal distance between initial and final positions after three wave cycles. In these calculations, we ignored the vertical effect because it was much smaller than the horizontal effect. In this study, particles were added every three wave periods from $z = -3$ cm to $z = 3$ cm with a 1-mm resolution. Particles were added across the interface at 200 cm from the wavemaker. To estimate mass transport at a certain depth, the vertical location of the particle relative to the center of the interfacial layer must be known. The vertical locations for initially fed particles were simply computed as the distances between particles and the undisturbed interface. However, for particles fed during the computation, the vertical location must be evaluated from the distance between a particle and the tentative interface distorted by the internal waves.

In the numerical experiments, the upper layer was fresh water and the lower layer was salt water. The density difference between the two layers was $\Delta\rho / \rho_0 = 0.03$, where $\rho_0 = 1000\, kg / m^3$ is a reference density. The transition thickness d measures how far salt has been able to diffuse into the fresh water. A sharp interface can be mathematically obtained in the limit $d \to 0$, but in reality, the interface will always be diffusive. For each run, a linear profile was always used as the initial condition of the density field, as shown in **Fig. 6.2** (blue line). The thickness of the interface layer increases from its initial thickness. The finite

thickness was assumed to change insignificantly during every three wave cycles. However, mixing always occurred near the interface, and so finally a sigmoidal profile of density (red line) was obtained (**Fig. 6.2**).

This model and techniques were applied to study transport of water particles near the interface in 11 cases: eight for a flat bottom and three for a bottom having a constant slope (**Table 4**). The fresh-water and salt-water layers had the same thicknesses ($h_I = h_{II}$), and the periodic fluxes were the same for the different cases of flat bottom and uniform slope. In this study, the origin of the axes was set at the intersection between the middle of the undisturbed interface and the wall where the wavemaker was placed (**Fig. 6.1**).

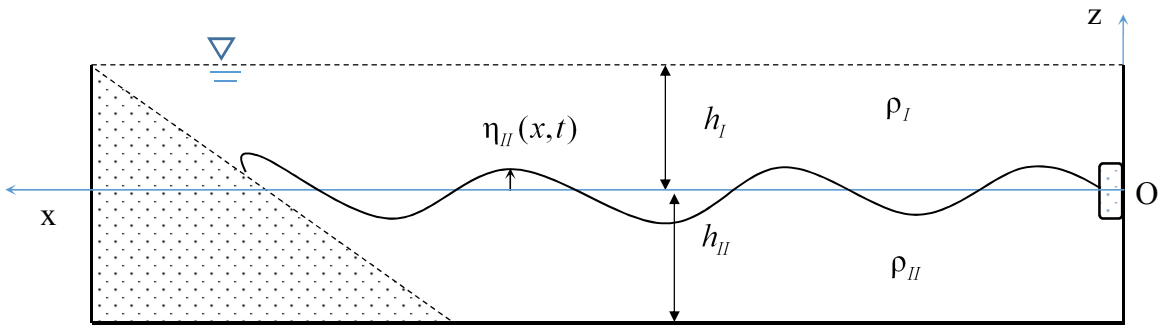

Fig. 6.1 Schematic diagram of computation domain

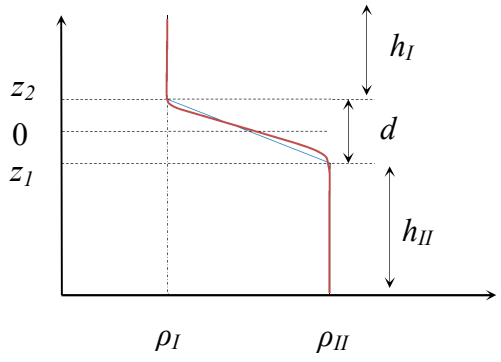

Fig. 6.2 Initial linear profile of density

6.3. Effect of diffusive transition layer on mass transport in a stratified water

6.3.1 Mass transport near the interface over a flat bottom

In this section, the effect of finite interfacial thickness on internal-wave propagation and mass transport is discussed using a numerical model that reproduced the kinematics of internal waves generated in a laboratory flume. With continuous wave generation, the thickness of the diffusive transition layer increases gradually due to mixing in the flume; however, in this investigation, it is assumed that this increase is not significant to consider the trend of mass tranport. To examine interfacial developments, the author compares the time series of interfacial displacements for cases having different initial interfacial thicknesses (Cases 1 and 4). **Fig. 6.3** shows the temporal displacements of the middle of the interfacial layer for the first 75 s at 200 cm from the wavemaker. The abscissa indicates the time from the start of wave generation and the ordinate indicates the displacement from the initial interface level. The wave increases during the first six wave cycles (~43.2 s), reaching stable state for the next four wave cycles (43.2-72.2 s). After 10 wave cycles, the interfacial displacement was disturbed owing to reflection of internal waves from the vertical wall at the opposite side of the wavemaker. The wave-arriving time for the thicker interfacial layer was delayed by about 1 s compared to that for the thinner layer. The author attributes the decrease in the wave celerity to the increase in interfacial thickness. Hutterman and Hutter (2001) verified this fact by measuring the speed of internal solitary waves. They found that wave speed decreases with increasing thickness of the diffusive interface. In this study, the author confirmed a similar tendency for periodic internal waves. In each computation, the same energy was applied; however, the displacement of the middle of the interfacial layer increases when the initial thickness was larger.

Fig. 6.4 shows variations of the density profiles for Cases 2 and 6 in which the initial interface thickness was 1.25 cm. The black and blue lines are for T = 5.2 s and 7.2 s, respectively. With an increase of mixing, the profiles change from linear to sigmoidal distributions. The mixing region was mostly concentrated on both boundaries between the interfacial layer and the two homogeneous layers. Inspecting carefully the differences between these two cases, the mixing for the shorter wave period is seen to be stronger than that for the longer wave period.

To understand mass transport inside and adjacent to the interfacial layer, water particle paths were compared for cases with different interfacial thicknesses. **Fig. 6.5** depicts vertical profiles of particle excursions after three wave cycles for Cases 1–4. As seen in the figure, each profile of computed particle excursion near the interfacial center differs from that assumed in the two-layer theory (Dore, 1970, 1970; Wen and Liu, 1995). The profiles of excursion in Cases 1 and 2 show moving directions that are identical to those in previous studies in the two-layer water. In those cases, water particles near the interface region move

in the wave direction, and the mass transport velocity reaches a maximum near the edge of the interfacial layer. When the interfacial thickness increases, particle excursions inside the zone tend to be smaller. For Case 3 ($d = 2.25$ cm), particles at the middle of the interfacial layer did not move much after three wave cycles. However, for Case 4 ($d = 3.25$ cm), particles near the interfacial center moved in the opposite direction to the wave propagation. This tendency becomes clearer in **Fig. 6.6**, which plots the relation between thickness and minimum excursion of particles in the middle of the interfacial layer. Minimum excursion is inversely proportional to interfacial thickness.

Fig. 6.7 depicts vertical profiles of particle excursions after three wave cycles for Cases 5–8. In Cases 5 and 6, particles near the interface were transported in the wave direction. These computed results show that in the interfacial layer, mass is transported over smaller distances as the layer becomes thicker. In the case of a sharper halocline ($d = 1$ cm), particle excursions do not reach maxima at $z = 0$ cm, but at $z = -1.5$ cm. Inside the interfacial layer, particles tend to move opposite to the offshore direction. This tendency also occurs for thicker layers, such as for the case of $d = 2.25$ cm. With increasing thickness of the interface, particles inside the halocline were transported in the direction opposite to wave propagation. Excursion of particles strongly depends on the thickness of the diffusive interface.

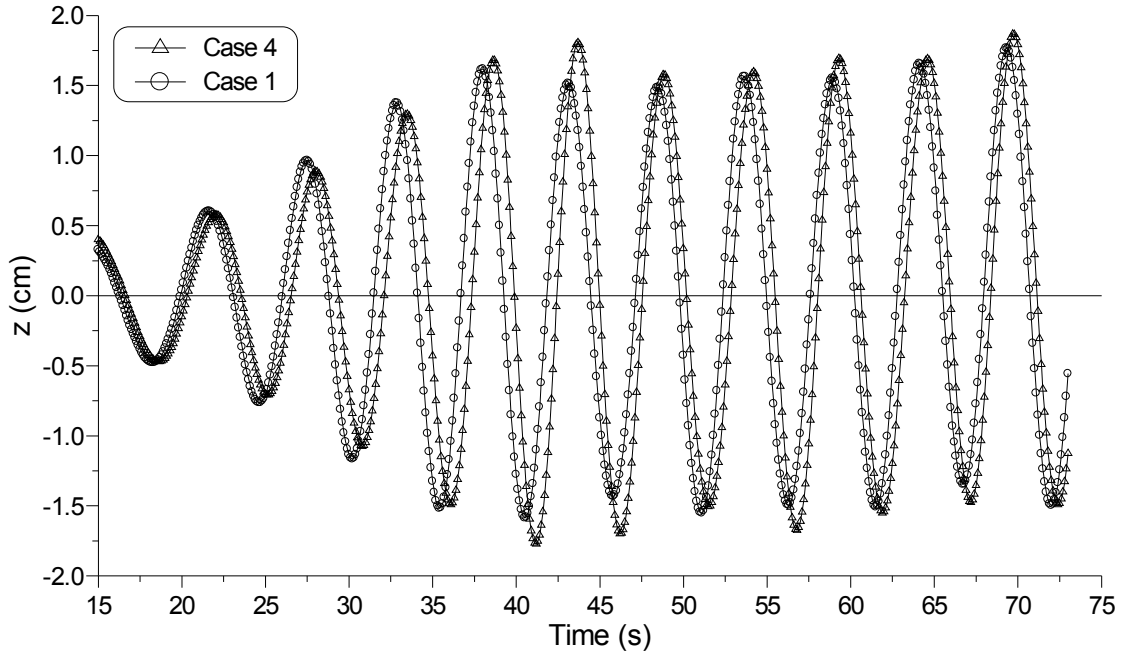

Fig. 6.3 Interfacial displacements for Cases 1 and 4 at 200 cm from the wavemaker

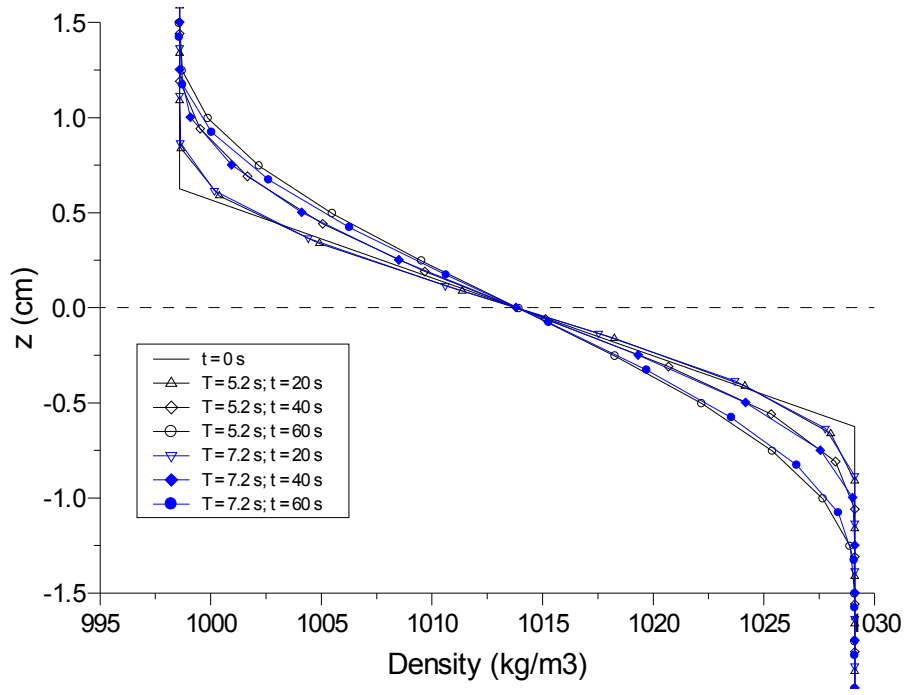

Fig. 6.4 Variations of density profiles for Cases 2 and 6 during first 60 s

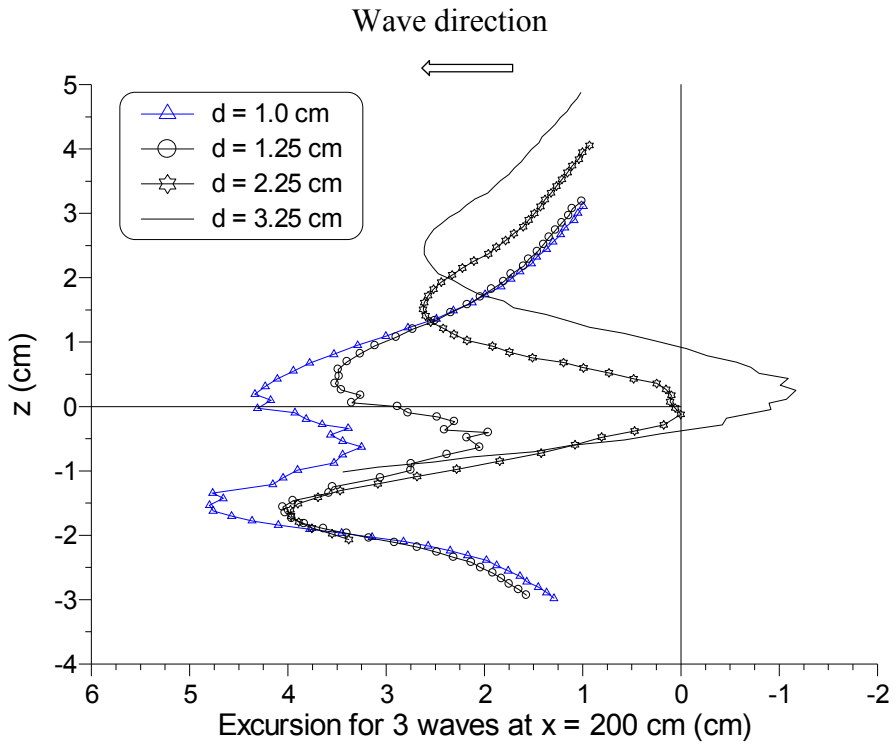

Fig. 6.5 Profiles of horizontal excursions for different interfacial thicknesses for Cases 1, 2, 3, and 4.

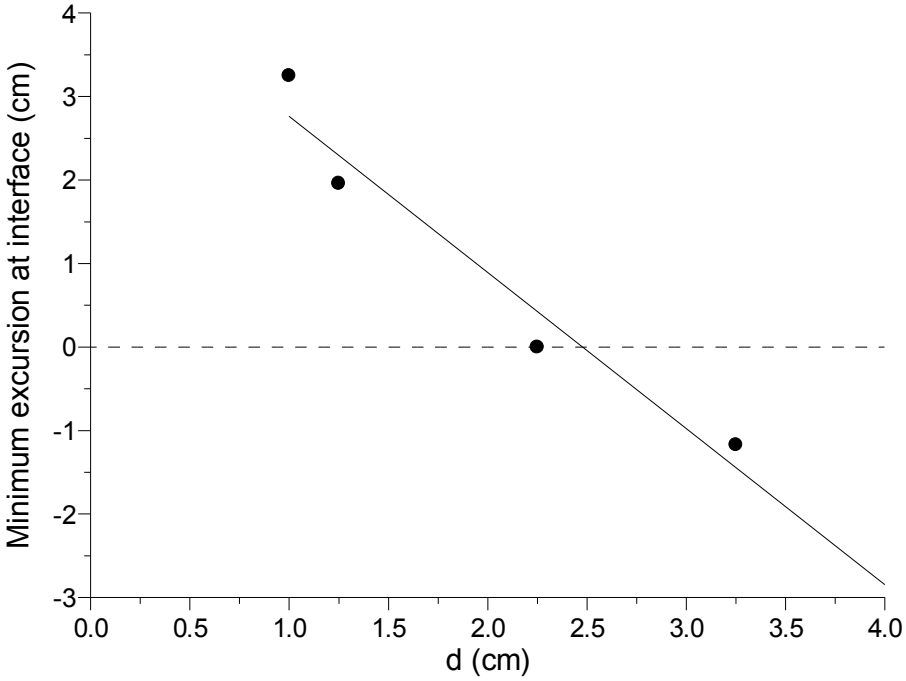

Fig. 6.6 Relationship between the minimum excursion at interface and interfacial thickness for Cases 1, 2, 3, and 4.

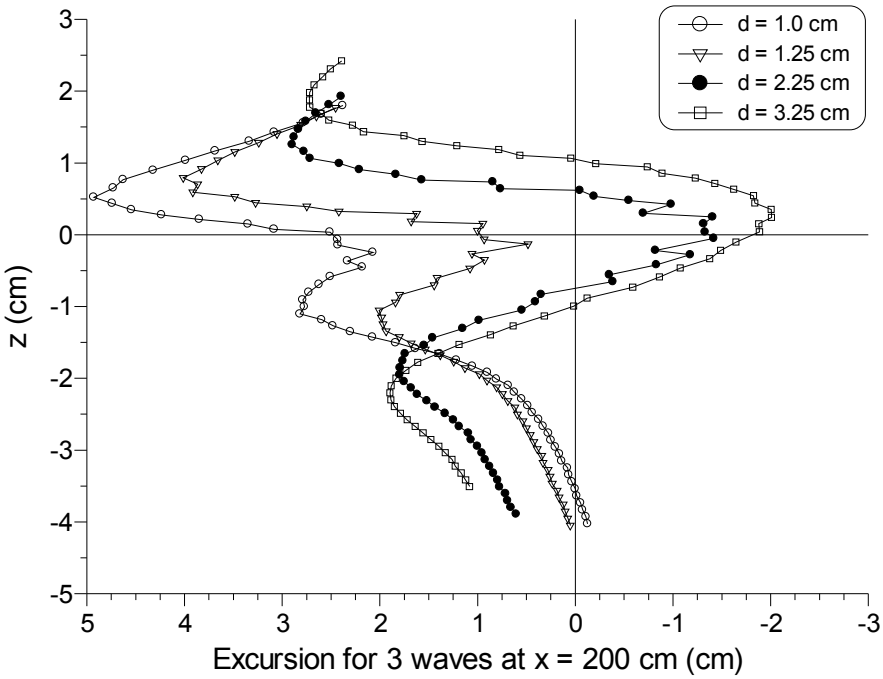

Fig. 6.7 Profiles of horizontal excursions for different interfacial thickness for Cases 5, 6, 7, and 8.

6.3.2 Mass transport near the interface over a bottom with a constant slope

In this part of the investigation, mass transport was studied before internal waves break over a constant slope (γ = 3/50). Three numerical experiments (Cases 9, 10, and 11) were carried out with different initial density profiles in the interfacial layers. For flat bottoms, reflected waves return only from the vertical wall, but for bottoms with a uniform slope, reflection occurs at all positions along the slope. The return flow from the upper slope affected mixing and mass transport. **Fig. 6.8** shows the vertical variation in density for an initial thickness of d = 2.25 cm. After 60 s of internal-wave generation, the density profile did not significantly change, except in the boundary region between the interfacial layer and the lower layer. Mixing in this region was stronger than that in the boundary region near the upper layer. The return flow is the main reason for this mixing because as can be seen in the figure, mixing is stronger with an increased lifetime of internal waves. Thickening of the interfacial layer in the lower layer might affect mass transport near both boundary regions.

Fig. 6.9 depicts horizontal profiles for excursions of particles near the interface after three wave cycles in the case of T = 7.2 s. The maximum mass transport velocity occurred under the lower boundary. This means that mass is transported faster in the boundary region of the lower layer when internal waves propagate over a slope in a two-layer fluid system. With increasing the thickness of the interfacial layer, the maximum mass transport velocity in the wave propagation direction decreases. The tendency of mass transport inside the linear stratified interface is very similar to the case of a flat bottom. The particles tend to move offshore as the thickness of the interface increases. As discussed above on the mixing induced by return flows, differences between the maximum horizontal excursions in two layers for cases over a slope are larger compare to those over flat bottoms.

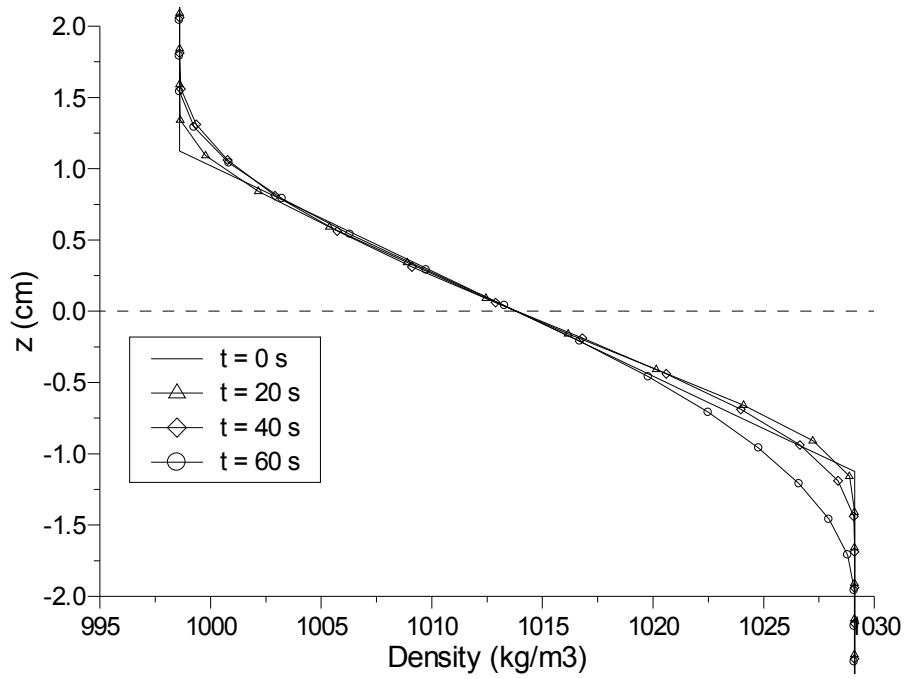

Fig. 6.8 Temporal variations of density profile for Case 10.

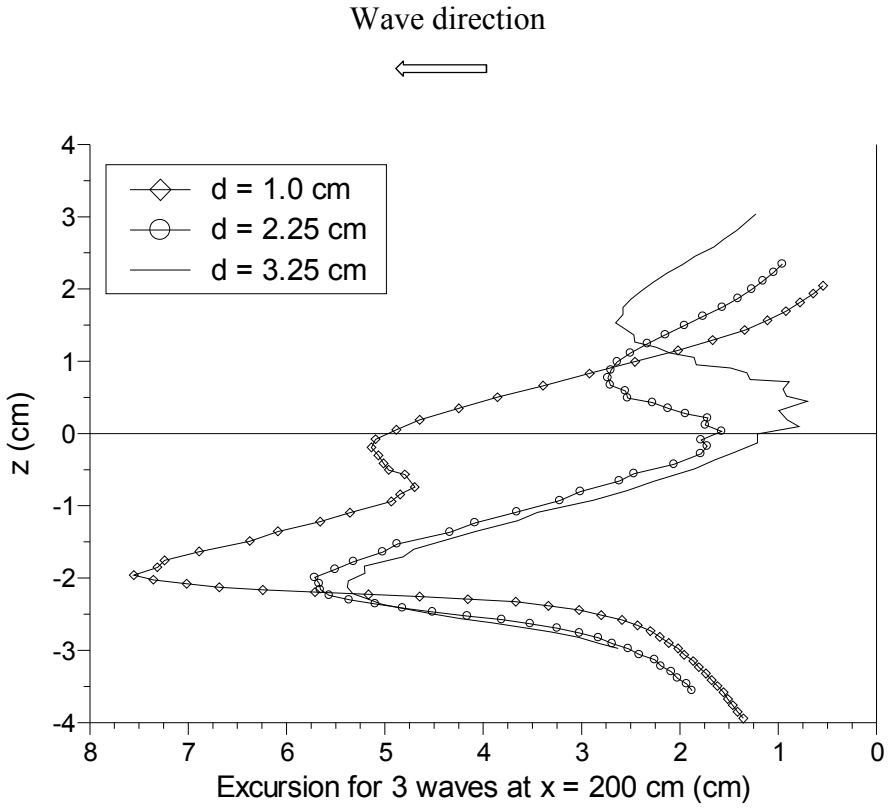

Fig. 6.9 Profiles of horizontal excursions for different interfacial thicknesses for Cases 9, 10, and 11.

6.4. Experimental investigations of effect of diffusive transition layer on mass transport

This section presents the experimental results of dye-streak method to verify the computational results and quantify the mass transport for both cases of flat bottom and slopping boundary. Firstly, the measurements of mass transport by internal waves in cases of flat bottom are presented using dye visualization photos taken in a laboratory tank. Due to the measurements, the similar conditions are used to input the numerical model to reproduce the phenomena of mass transport. Then, the similar visualization for the cases of slopping boundary is presented to confirm the tendency of mass transport which was found in the previous section.

6.4.1 Experiments of mass transport in the wave tank with a flat bottom

The experiments were conducted in the same laboratory wave tank described in the previous chapter. The basics of stratification generation and dye-streak method were presented in Chapter 3. For a wave tank with a flat bottom, four experimental cases were conducted with different interfacial thicknesses and wave heights (**Table 5**).

Electronic conductivity meter was used to measure the vertical distribution of salinity at 2 mm intervals. Sigmoidal profiles of salinity can be observed in **Fig. 6.10**. In the experiments, salinity varied from 0 ppt in the upper layer to 40 ppt in the lower layer. After measurement of salinity, the hyperbolic tangent profile was used to fit with the measured data. This distribution was used to interpolate values, used as input to the numerical model for estimating the resulting mass transport due to internal waves. The sigmoidal transition function is:

$$S = S_0 - \frac{\Delta S}{2}\tanh(\alpha z)$$

where S is the salinity; $S_0 = \frac{S_I + S_{II}}{2}$ is the average salinity; S_I, S_{II} are the salinity in the upper and lower homogeneous layers, respectively; z is the vertical level; and α is a constant. Troy and Koseff (2005) used a similar distribution for density to fit the density profile. The measurements of salinity show that the fit by the hyperbolic tangent profile is reasonable (**Fig. 6.10**). The thickness of transition layer is defined by creating a piecewise linear profile that is tangential with the measured profile.

The dye-streak method was used to visualize and measure mass transport in the laboratory tank. When a grain of dye was injected from the surface into the water column, a significantly straight profile of dye was created (**Fig. 6.11**). The dye streak was distorted by water movement due to the internal wave propagation. After recording the temporal variations of the dye streak, the video was converted into a series of images. The dye-streak

profiles were digitized in subsequent images with the same coordinates. Mass transport velocity could be estimated by the distance of dye-streak displacement in its traveling time.

Figs. 6.11 and **6.12** show the movements of dye streaks after 8 wave cycles. Despite the shape of the initial dye streaks, after some wave cycles, all dye streaks inside the diffusive transition layer had the same shape. It can clearly be observed that mass is transported toward offshore inside the transition layer. Thus, the phenomenon of transport observed in the numerical results in the previous section is confirmed.

Mass transport velocity due to interfacial displacement was averaged in 3 wave cycles to discuss the profile shape and the order of mass transport velocity. **Fig. 6.13** depicts the measured and computed results of mass transport velocity. The velocity profiles prove the tendency of mass transport discussed in Chapter 2 and observed in the computed results in the previous section. In the density-stratified water separated by a diffusive transition layer, mass was transported in the direction of wave propagation in the adjacent regions of the interfacial layer, while it was transported in the opposite direction in the remaining layers. Focus was given to mass transport velocity inside the interfacial layer. It should be noted that in the diffusive transition layer, the tendency of mass transport is in complete contradiction with the result of Dore (1970). Compared to Al-zanaidi and Dore (1976), mass transport velocity in the transition layer agrees with their argument, but it is opposite in the remaining layers. The tendency of mass transport is a combination of the phenomenon in the two-layer and linearly continuous stratification. The measured profiles of mass transport velocity reproduced well by the numerical model, in particular, in the direction of mass transport. However, the computed data underestimated the excursion of particle inside the diffusive transition layer. This discrepancy may be caused by the numerical model, where the wave absorber was not designed so that the reflected waves could affect the profiles of mass transport. The numerical diffusion due to the resolution in interfacial layer may also the reason of this discrepancy. The agreement in direction of mass transport velocity suggests that it is necessary to consider about the effect of diffusive transition layer on theory of mass transport.

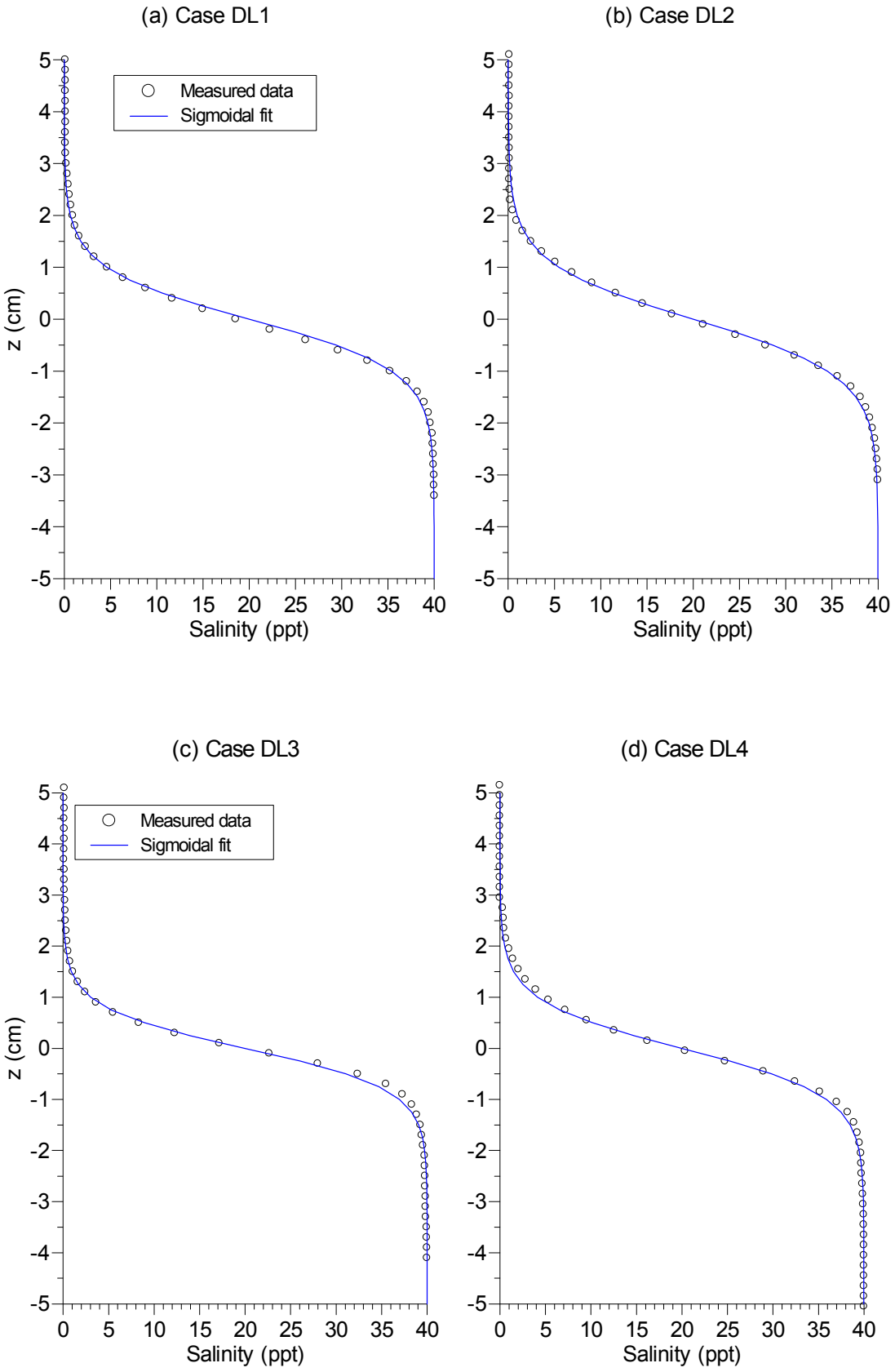

Fig. 6.10 Profiles of salinity for experiment cases for Cases DL1-DL4

(a) The initial dye streaks

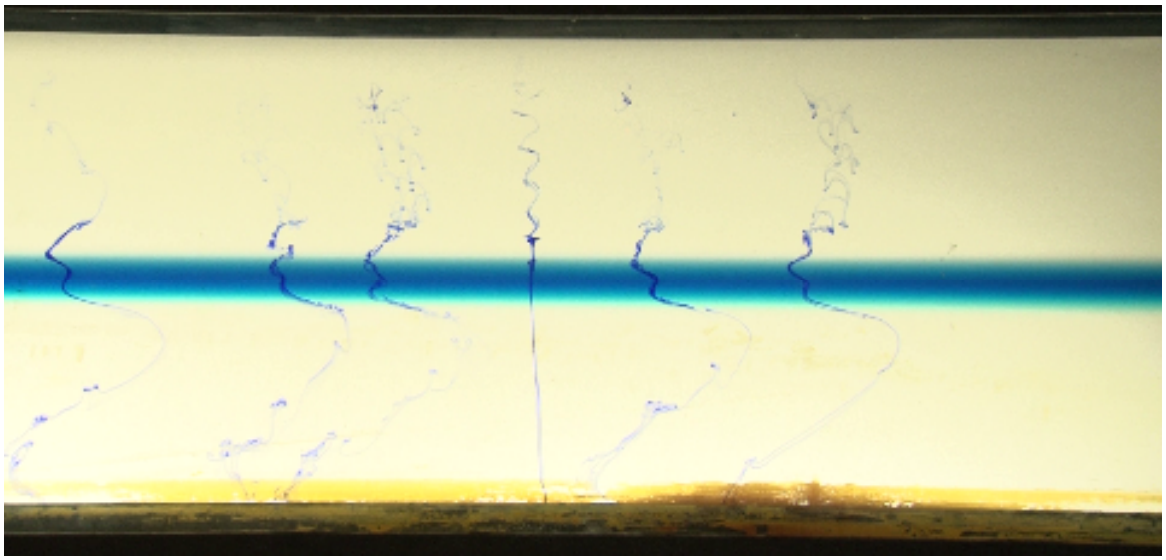

(b) The dye streaks after 8 wave cycles

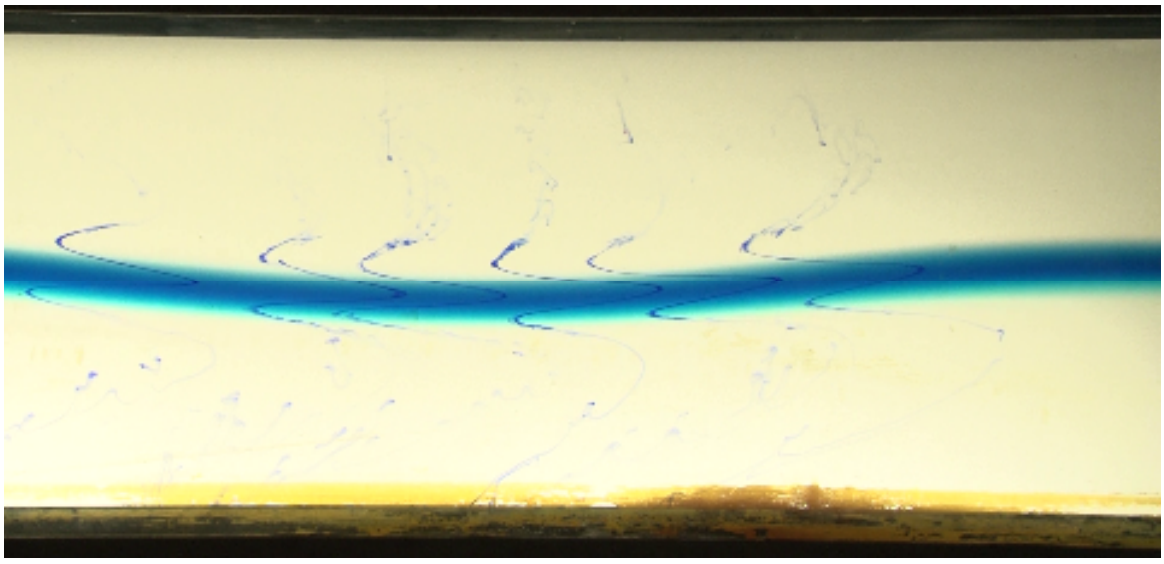

Fig. 6.11 The movement of dye streaks after several wave cycles for Case DL2. Internal wave propagation is from right to left

(a) The initial dye streaks

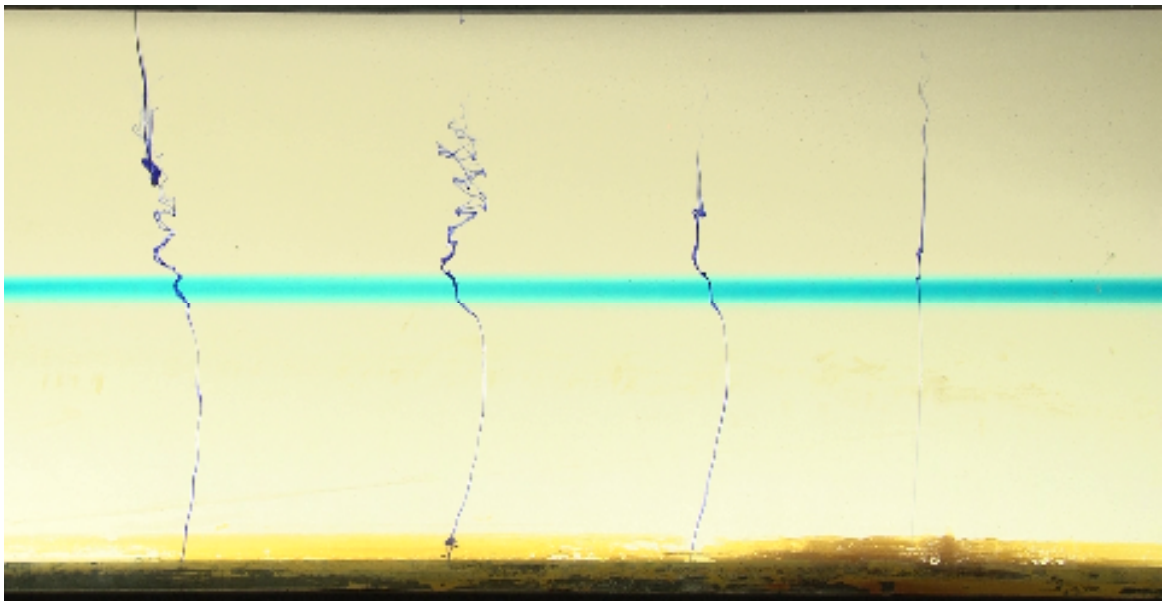

(b) The dye streaks after 8 wave cycles

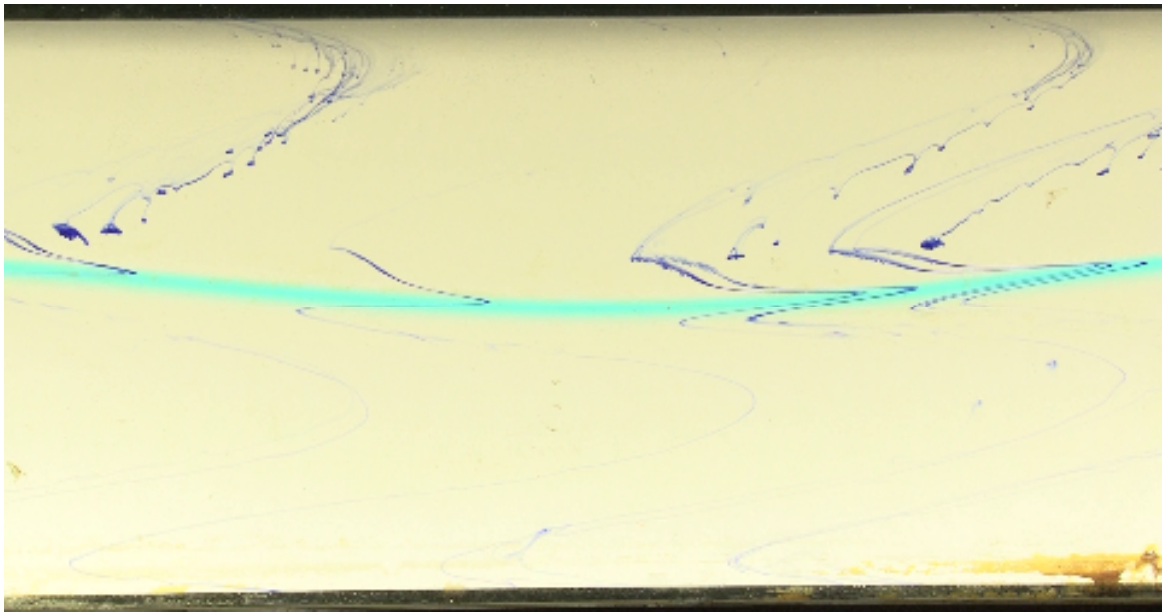

Fig. 6.12 The movement of dye streaks after several wave cycles for Case DL4

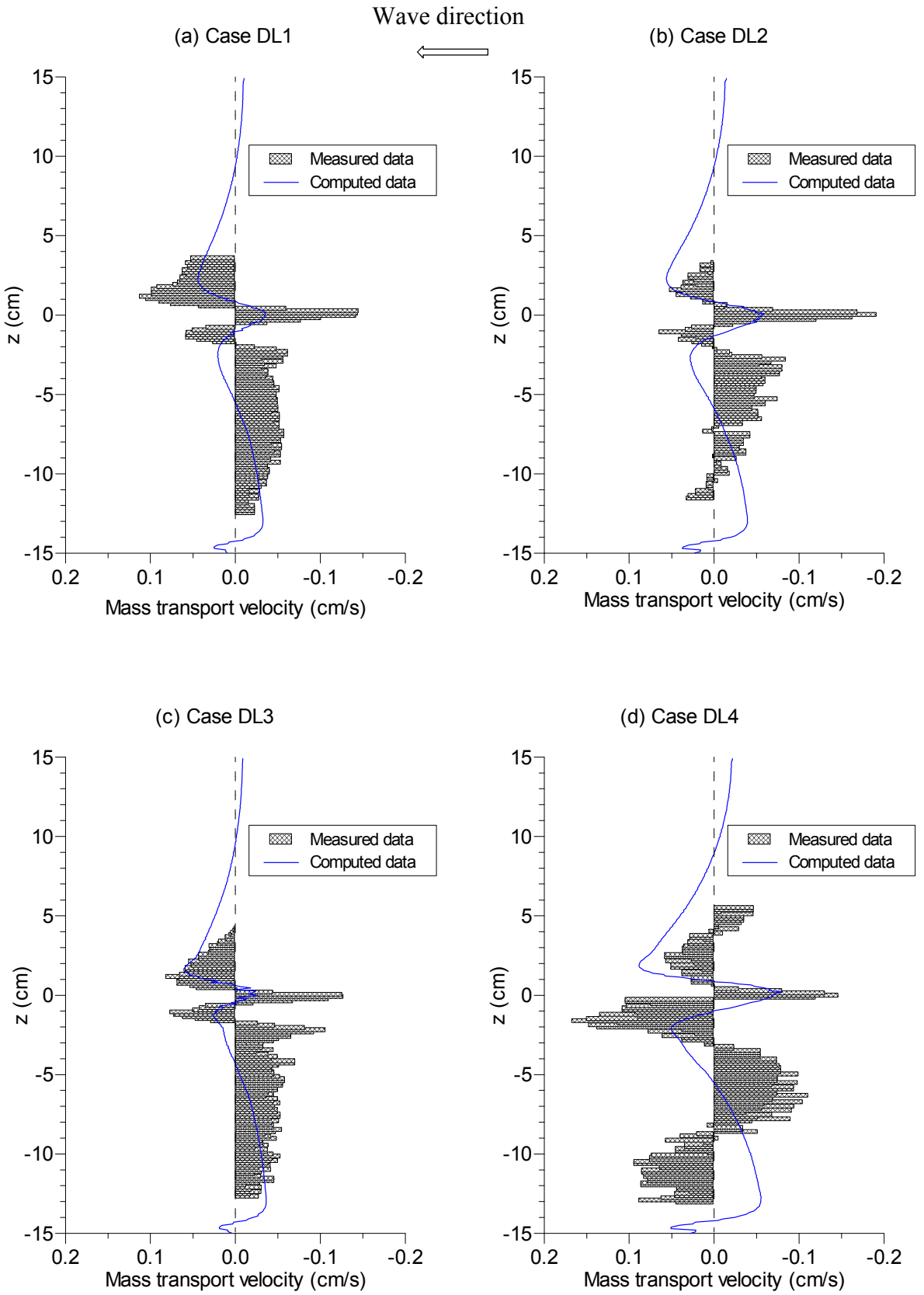

Fig. 6.13 Profiles of average mass-transport velocity for Cases DL1-DL4

6.4.2 Experiments of mass transport in the wave tank with a constant slope

The finding of tendency of mass transport in the wave tank with flat bottom was confirmed with dye-streak method. In this section, the similar experiment was carried out to confirm the direction of mass transport in the wave tank with a constant slope. A slope of γ = 3/50 was placed at the bottom of the tank. During the experiment, the water level was maintained constant at 30 cm.

Fig. 6.14 compares the initial density profile with the profile averaged over the first 60 s. Differences in the two profiles mainly occur near the edges of the interfacial layer; no substantial differences were found in the main body of the interfacial layer. Therefore, we conclude that in these computational cases, the diffusion process does not alter the mass transport mechanism inside the layer.

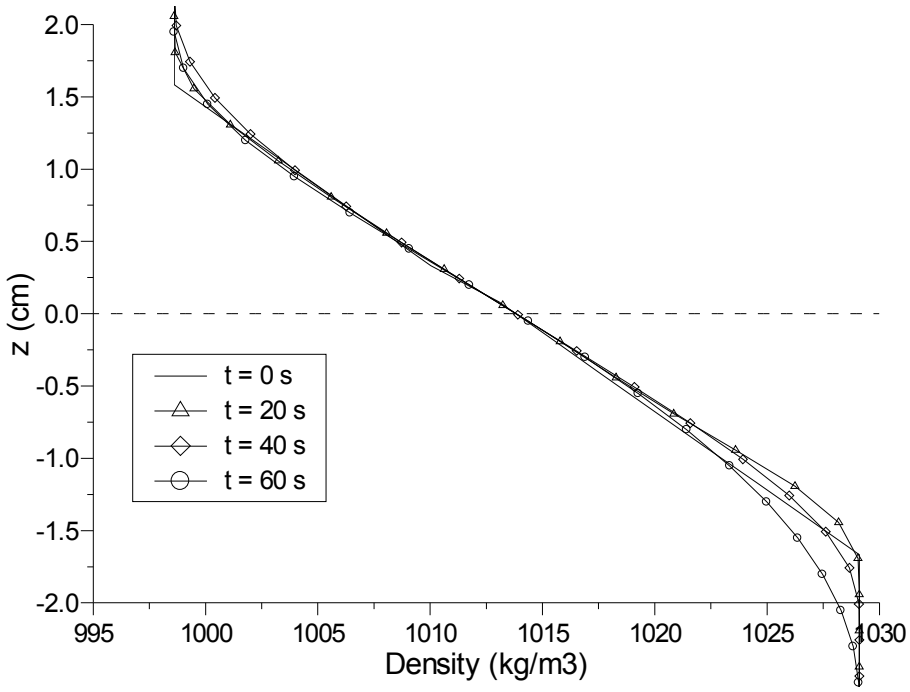

Fig. 6.14 Variation of density profile at x = 200 cm for Case 11

Before the wavemaker movement, several dye particles were injected into the water column to create vertical streaks, as shown in **Fig. 6.15 (a)**. When the wavemaker started, internal waves with heights of 3.5 cm and T = 7.2 s were generated and propagated up the slope. The dye streaks were distorted owing to the mass transport velocity. After 28.8 s, the vertical distributions of dye were captured, as shown in **Fig. 6.15 (b)**. The excursions of dye streaks in the lower layer show a large transport in the direction of the internal waves. A

similar trend of transport toward shore can be observed in the upper layer, though with less movement. The most noticeable tendency is the excursions of dye near the interface. Near the interface, the dye was transported in the direction opposite to the wave direction.

Although this measurement is only qualitative, it helps confirm the computed results discussed in Section 6.3.2. To obtain more quantitative experimental results, it is necessary to control density stratification inside the interfacial layer. If this can be done, we will be able to more correctly understand the phenomenon of mass transport by internal waves. The key difference between the experiments in this section and those in Section 6.3.2 is that in Section 6.3.2, particles were added every three wave cycles, but in this section, particles were added and maintained over 10 wave cycles (T = 7.2 s).

The mass transport of particles at a given location (x = 200 cm) is shown for the first 10 wave cycles in **Fig. 6.16**. An initial vertical distribution of particles (blue line) was added with a resolution of 1 mm and a length of 3 cm to both sides of the undisturbed interface. At t = *7.2 s*, the particles started moving owing to the action of the wavemaker. The particles in the upper and lower layers move in opposite directions. During the next 7.2 s, particles in both the upper and lower zones move in the wave direction, except for particles around the undisturbed interface (from z = −1.5 cm to z = 1.0 cm). This tendency continues with the passing of internal waves. It is also possible to observe the development of interface thickness. After t = 28.8 s, the distance between two maximum excursions in each layer increases. The excursion of particles in the lower zone is larger than that in the upper zone. The difference in mass might be a reason for this difference. The heavier fluid in the lower zone might have larger kinetics than in the upper zone, even for the same disturbance in each layer.

In this investigation, a new finding regarding the effect of interfacial thickness on mass transport in a two-layer fluid with a transitional thin layer is presented based on computed results using the two-dimensional model. This result may contribute to field observations of suspended-sediment transport due to internal waves in oceans and lakes.

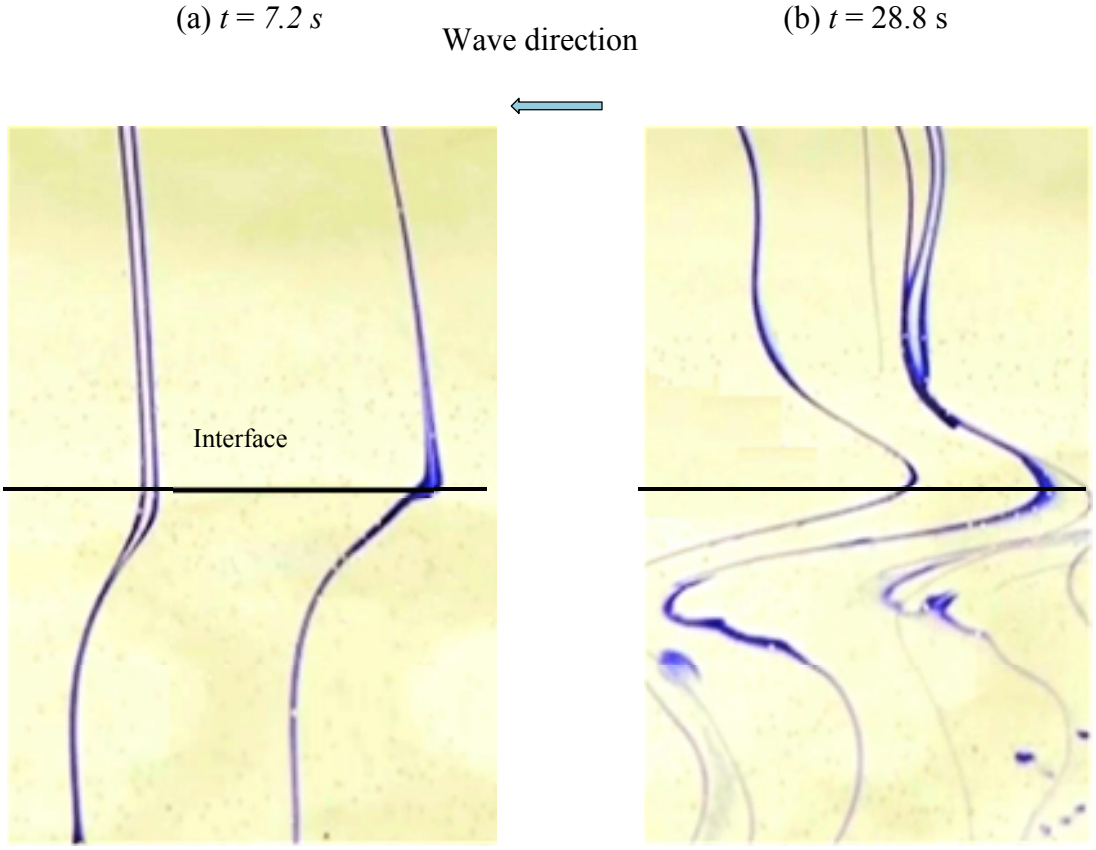

Fig. 6.15 The movement of dye streak after three wave cycles (T = 7.2 s)

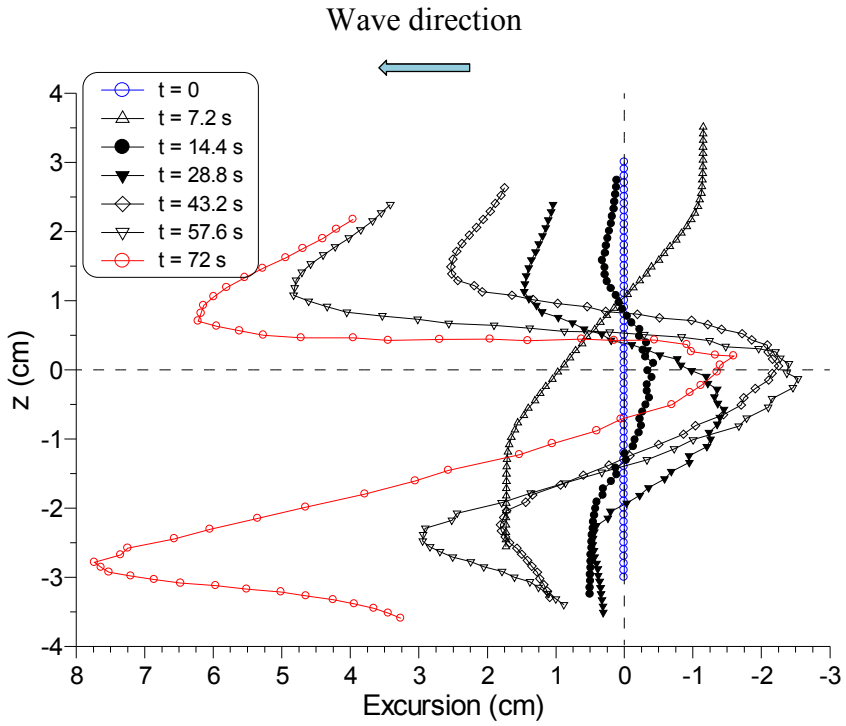

Fig. 6.16 Temporal variations of profiles of particle movements at x = 200 cm for Case 11

6.5. Conclusions

This chapter presents a new finding about the tendencies of mass transport in a density-stratified water separated by a diffusive transition layer. A two-dimensional nonhydrostatic model was used to simulate mass transport for both flat bottoms and bottoms with constant slopes. Mass is transported toward shore with a maximum velocity that is not at the interface. Inside the stratified interface, mass is transported in the direction opposite to the wave direction as the interfacial thickness increases. The maximum mass transport velocity inside the transition layer decreases with an increase of interfacial thickness. As a result, with a thick interface, particles near the interface will be transported farther offshore. This tendency was confirmed by conducting experiments in a wave tank for both flat bottom and constant slope. By using the dye-streak method, the mass transport velocity was estimated and quantified for different thicknesses of diffusive transition layer.

Chapter 7

Conclusions and Recommendations

7.1. Conclusions

This thesis presents experimental and numerical studies on the internal wave kinematics with focus on water particle trajectory and resulting mass transport due to the propagation of internal waves in density-stratified water.

A series of experiments were performed for different wave heights, periods, and thickness ratios between two layers using different measuring methods to examine the internal wave kinematics. In the laboratory experiments, particle image velocimetry (PIV) was used to measure the two-dimensional velocity field in an internal wave tank. Internal-wave profile and celerity were measured using the light attenuation method. The technique to transfer from Eulerian velocity field obtained by PIV to Lagrangian velocity of arbitrary water particles was applied. Therefore, the water particle trajectory in the laboratory can be obtained. Then, the Stokes drift was computed by integrating the particle velocity in time. The resulting mass transport by water particle movement was estimated from PIV measurements and numerical method, and was confirmed using the dye-streak method.

The two-dimensional hydrodynamic model was applied to simulate the phenomena owing to the propagation of internal waves in a wave tank scale. The results were in reasonable agreement with related laboratory results and showed similar variations of velocity field, interfacial displacement, celerity, and particle trajectory. The model was also applied to investigate the relationship of mass transport with different thickness ratios between the two layers and stratifications. Mass transport considering wave characteristics and the thickness ratios of upper and lower layers was investigated.

The temporal variations of velocity field were measured along a constant slope. The two-dimensional nonhydrostatic model reproduced the measured instantaneous velocity field well. Both the measured and computed velocity fields were used to compute the particle trajectory. The trajectory of water particles is not elliptical and not closed for all cases. Water particles move clockwise in the upper layer, and anticlockwise in the lower layer. Near the

density interface, the horizontal and vertical displacements of water particles are large relative to those near the surface and bottom regions. The particles march forward with a large nonclosed loop near the density interface, implying that each particle yields a maximum drift. In general, the vertical excursion of the particle is much smaller than its horizontal excursion, especially around the density interface.

The distributions of mass transport velocity along a uniform slope were also numerically and experimentally estimated for different wave characteristics. Mass transport and return flow from the shore side on the sloping boundary were clearly observed in the results. The internal waves transported the mass with maximum velocity in the shore direction near the density interface in the two-layer water. Mass transport velocity decreases toward the sloping bottom or surface. The fictitious wave steepness, originally defined for surface waves, was adapted to internal waves. The fictitious wave steepness increases along the slope, reaches to a peak at a certain point, and decreases toward the origin. In the region where the steepness decreases, mass transport velocity becomes stronger. It can be confirmed that the internal waves are important for the mass transfer especially near the interface.

For the cases of flat bottom, mass transport by internal waves increased with the thickness ratios between the upper and lower layers in the stratified fluid. The maximum mass transport velocity near the interface is the highest when the upper and lower layer thicknesses are equal, and it becomes smaller as the thickness of the lower layer exceeds that of the upper layer. In addition, mass transport velocity varies proportionally with the wave height for each thickness ratio.

A special attention is paid to the effect of the diffusive transition layer between two homogeneous layers on mass transport. The role of this layer is normally ignored in investigation of internal wave kinematics and mass transport with the assumption of two-layer or linearly continuous stratifications. The numerical and experimental results for mass transport in the fluid, which consists of two homogeneous layers separated by the diffusive transition layer, revealed that its profile is quite similar to that of the superposition of linear stratification and purely two-layer cases. Mass transport velocity does not reach a maximum at the center of the interfacial layer but at the two boundaries between the interfacial layer and the remaining layers. As the interfacial thickness increases, particles in the interfacial layer might remain stationary or even move against the propagation direction. With a thick interface, particles near the interface will be transported farther offshore. A series of experiments were conducted with dye-streak method in both flat bottom and constant slope. The experimental results for mass transport in the fluid, which consists of two homogeneous layers separated by a diffusive transition layer, confirmed the new finding in the profile of mass transport velocity. The diffusive transition layer is to be considered when investigating mass transport in density-stratified water.

7.2. Recommendations

In this investigation, the author presented numerical and experimental results of celerity distribution along a constant slope. The formulae for computing wave celerity in the flat bottom derived by Lamb (1932) and in the constant slope by method of characteristics were applied to compare the computed and measured data. The comparison showed that the theoretical formulae of wave celerity are overestimated. In both formulae, the stratification is assumed as two layers for convenience of mathematical treatment. However, in oceans or lakes, the diffusive transition layer always has a significant thickness. The effect of diffusive transition layer thickness on celerity should be considered in the theoretical formula.

In this thesis, the experiments and related computations were conducted for different thickness ratios, wave heights, and periods. However, the density difference between the two homogeneous layers was always fixed at 30 g/cm^3. In closed lakes or oceans, the density difference depends strongly on the change of temperature between seasons. The dependence of mass transport on the density difference between upper and lower layers should be investigated to understand the transport phenomenon.

The importance of mass transport due to internal wave propagation and the role of diffusive transition layer were confirmed. The transition layer affected not only magnitude but also the direction of mass transport velocity. Several experiments were conducted to prove this phenomenon. However, the quantification and scaling of mass flux inside the interfacial layer, which is transported backward compared to the forward fluxes in the two layers, has still not been studied. The study also should be extended to mass transport in real stratification in oceans or lakes, where the thickness of thermocline can reach tens to hundreds meters. Mass transport inside the pycnocline (metalimnion or thermocline) should be investigated with observed data. The result might change our understanding of the transport of sediments, nutrients, larvae, or contaminants. It is very advance and important progress on mass transport investigation.

In the diffusive transition layer, the mass is always transported in the opposite direction of wave propagation. It seems that the resulting flow inside the interfacial layer always exists and is the driving force of mass transport. The effect of viscosity and mixing due to internal waves are necessary to quantify the contribution to mass transport inside the interfacial layer. From that, the nature of transport can be explained clearly to obtain a united theory of mass transport.

Appendix

Tables of Experimental and Computational Cases

This appendix shows a series of the tables for experimental and computational cases in this dissertation. **Tables 1** and **2** present the experimental cases for both a flat bottom and a constant slope. **Tables 3, 4** and **5** show the cases for simulations by non-hydrostatic numerical model. The results of experimental cases in **Table 1** were presented in Chapter 3, 4 and 5 while those in **Tables 2** and **3** were discussed only in Chapter 5. The computational and experimental cases in **Tables 4** and **5** were used to discuss about the effect of diffusive transition layer on mass transport in Chapter 6.

Table 1. Experimental cases for a constant slope

Case	Slope	Density in lower layer (mg/cm^3)	h_I : h_{II}	Wave height* H (cm)	Period (s)
S1	3/50	1,028	12 cm : 18 cm	2.2	5.2
S2				2.1	7.2
S3		1,028	15 cm : 15 cm	2.6	5.2
S4				2.7	7.2
S5		1,028	10 cm : 20 cm	2.8	5.2
S6				2.4	7.2
* Wave height was measured using a wave gauge at 100 cm from the wavemaker					

Table 2. Experimental cases for flat bottom

Case	Density in lower layer (mg/cm^3)	h_I : h_{II}	Wave height* H (cm)	Period (s)
F1	1,028	15:15	2.3	5.2
F2			2.8	5.2
F3		15:15	1.9	7.2
F4			2.7	7.2

Table 3. Computational cases for flat bottom

Case	Density in lower layer (mg/cm^3)	$h_I : h_{II}$	Wave height H (cm)	Period (s)
CF1	1,028	15:15	1.94	5.2
CF2			1.9	7.2
CF3			1.9	7.2
CF4		10:20	1.26	5.2
CF5			2.0	7.2
CF6		5:25	0.64	5.2
CF7			0.60	7.2
CF8		13:17	2.75	5.2
CF9			2.48	7.2

Table 4. Computational cases for different interfacial thicknesses

Case	Angle of slope (γ)	Wave period (s)	Interfacial thickness d (cm)
1	π/2	5.2	1.0
2			1.25
3			2.25
4			3.25
5		7.2	1.0
6			1.25
7			2.25
8			3.25
9	0.06	7.2	1.0
10			2.25
11			3.25

Table 5. Experimental cases for different interfacial thicknesses

Case	Wave height (cm)	Wave period (s)	Interfacial thickness d (cm)
DL1	2.29	7.2	2.4
DL2	2.51		2.5
DL3	2.31		1.5
DL4	3.26		2.0

References

1. Adrian R.J. (1991). Particle-imaging techniques for experimental fluid mechanics. Annu. Rev. Fluid Mech., Vol. 23, pp. 261-304.
2. Afanasyev, Y. D. and Peltier, W. R. (2001). On breaking internal waves over the sill in Knight Inlet, Proceedings of the Royal Society of London A, 457, pp. 2799–2825.
3. Al-Zanaidi, M. A. and Dore, B. D. (1976). Some aspects of internal wave motion, Pure Appl. Geophys., 114, pp. 403-414.
4. Anthoni J. F. (2000). Oceanography: special waves, at:

   www.seafriends.org.nz/oceano/waves.htm.
5. Apel, J. R., Byrne, H. M., Proni, J. R., and Charnell, R. L. (1975). Observations of oceanic internal and surface waves from the Earth resources technology satellite. J. Geophys. Res., Vol.80, No.6, pp.865–881.
6. Apel, J. R., Byrne, H. M., Proni, J. R., and Sellers, R. L. (1976). A study of oceanic internal waves using satellite imagery and ship data. Remote Sens. Environ., Vol.5, pp.125–135.
7. Apel, J. R., Holbrook, J. R., Liu, A. K., and Tsi, J. (1985). The Sulu Sea internal soliton experiment. J. Phys. Oceanogr., Vol.15, No.12, pp.1625–1651.
8. Bagnold, R. A. (1947). Sand movement by waves: some small-scale experiments with sand of very low density, J. Inst. Civil Engrs., 27, pp. 447-469.
9. Battjes, J.A. (1974). Computation of set-up, longshore currents, run-up and overtopping due to wind generated waves, Comm. on Hydraulics, Report 74-2, Dept. of Civil Eng., Delft University of Technology, Delft.
10. Benjamin, T. B. (1966). Internal waves of finite amplitude and permanent form, J. Fluid Mech., 25, pp. 241–270.
11. Benjamin, T. B. (1967). Internal waves of permanent form of great depth. J. Fluid Mech., 29, pp. 559–592
12. Benney, D. (1966). Long nonlinear waves in fluid flows, J. Math & Phys., 45, pp. 52-63.
13. Boehm, A. B., Sanders, B. F., and Winant, C. D. (2002). Cross-shelf transport at Huntington Beach. Implications for the fate of sewage discharged through an offshore ocean outfall, Environ. Sci. Technol, 36, pp. 1899-1906.

14. Bogucki, D. and Garrett, C. (1993). A simple model for the shear-induced decay of an internal solitary wave. J. Phys. Oceanogr., 23, pp. 1767–1776.

15. Bourgault, D. and Kelley, D. E. (2007). On the reflectance of uniform slopes for normally incident interfacial solitary waves, J. Phys. Oceanogr., 37, pp. 1156-1162.

16. Brown, B. E. (1997). Coral bleaching: Causes and consequences, Coral Reefs, 16, pp. S129–S138.

17. Cacchione, D. A. and Southard, J. B. (1974). Incipient sediment movement by shoaling internal gravity waves, J. Geophys. Res., Vol. 79, pp. 2237-2242.

18. Cacchione, D. A., and Wunsch, C. (1974). Experimental study of internal waves over a slope, J. Fluid Mech., 66, 223–329.

19. Cacchione, D. A., Pratson, L. F., and Ogston, A. S. (2002). The shaping of continental slopes by internal tides, Science, 296, pp. 724-727.

20. Choi, W. and Camassa, R. (1996). Weakly nonlinear internal waves in a two-fluid system, J. Fluid Mech., 313, pp. 83-103.

21. Choi, W. and Camassa, R. (1999). Fully nonlinear internal waves in a two-fluid system, J. Fluid Mech., 396, pp. 1–36.

22. Chorin, A. J. (1968). Numerical solution of the Navier-Stokes equations, Math. Comput., 22, pp. 745–762.

23. Cummins, P. F. (2000). Stratified flow over topography: time-dependent comparisons between model solutions and observations. Dynam. Atmos. Oceans, 33, pp. 43–72.

24. Davies, A. M. and Xing, J. (2005). The effect of a bottom shelf front upon the generation and propagation of near-inertial internal waves in the coastal ocean, J. Phys. Oceanogr., 35, pp. 976–990.

25. De Silva, I.P.D., Imberger, J., and G.N. Ivey. (1997). Localized mixing due to a breaking internal wave ray at a sloping bed, J. Fluid Mech., 350, pp. 1–27.

26. Defant A. (1961). Physical Oceanography, Vol. II, Pergamon, 598 pp.

27. Dore, B. D. (1970). Mass transport in layered fluid systems, J. Fluid Mech., Vol. 40, pp. 113-126.

28. Dore, B. D. (1973). On mass transport induced by interfacial oscillations at a single frequency. Proc. Camb. Phil. Soc., Vol. 74, pp. 333-347.

29. Fringer, O. B. and Street, R. L. (2003). The dynamics of breaking progressive interfacial waves, J. Fluid Mech., Vol. 494, pp. 319-353.

30. Fu, L. L. and Holt, B. (1982). SEASAT views oceans and sea ice with synthetic aperture radar, NASA/JPL Publ. 81-120, Calif. Inst. Technol., Pasadena, 204 pp.

31. Gil, G. T. C. and Fringer, O. B. (2011). Lagrangian- and Eulerian-mean effects in progressive internal gravity waves, Manuscript submitted to Phys. Fluid.

32. Gill, A. E. (1982). Atmosphere-Ocean Dynamics, Academic Press, New York.

33. Gross, M. G. (1990). Oceanography, Prentice Hall, p. 205.

34. Grue, F., Jensen, A., Rusas, P.-O. and Sveen, J.K. (1999). Properties of large-amplitude internal waves. J. Fluid Mech., 380, pp. 257-278.

35. Grue, J. (2006). Very large internal waves in the ocean-Observations and nonlinear models, in: Grue J. and Trulsen K. (Eds), Waves in geophysical fluids: Tsunamis, rogue waves, internal waves and internal tides, SpringerWien, NewYork.

36. Haidvogel, D. B. (2005). Cross-shelf exchange driven by oscillatory barotropic currents at an idealized coastal canyon, J. Phys. Oceanogr., 35, pp. 1054–1067.

37. Halpern, D. (1971). Observations of short period internal waves in Massachusetts Bay, J. Mar. Res, Vol. 29, pp. 116-132.

38. Harleman, D. R. F. (1961). Stratified flow. In: Streeter (ed.), Handbook of fluid mechanics, New York, McGraw Hill, Chapter 26, 21p.

39. Harlow, F. and Welch, E. (1965). Numerical calculation of time-dependent viscous incompressible flow of fluid with free surface, Phys. Fluids 8, pp. 2182–2189.

40. Haury, L. R., Briscoe, M. G. and Orr, M. H. (1979). Tidally generated internal wave packets in Massachusetts Bay, Nature, 278, pp. 312-317.

41. Heineke, D. and Verhagen, H. J. (2007). On the use of the fictitious wave steepness and related surf similarity parameter in methods that describe the hydraulic and structural response to waves, Proc. 5th Coastal Structures Conference, Venice, Italy, pp. 1057-1066

42. Helfrich, K. R. (1992). Internal solitary wave breaking and run-up on a uniform slope, J. Fluid Mech., 243, pp. 133-154.

43. Helfrich, K. R. and Melville, W. K. (2006). Long nonlinear internal waves, Annu. Rev. Fluid Mech., Vol. 38, pp. 395-425.

44. Helland-Hansen, B., and Nansen F. (1909). The Norwegian Sea. Norwcg. Fish. and Marine Invest. Rep., 2(2) Pt. 1.

45. Hill, D. F. (2002). General density gradients in general domains: the 'two-tank' method revisited, Exp. Fluid, No. 32(4), pp. 434–440.

46. Holloway, P. E. (1987). Internal hydraulic jumps and solitons at a shelf break region on the Australian North West shelf, J. Geophys. Res., 92, pp. 5405–5416.

47. Hosegood, P. and van Haren, H. (2004). Near-bed solibores over the continental slope in the Faroe-Shetland Channel, Deep Sea Res., 51, pp. 2943-2971.

48. Hunkins, K. and Fliegel, M. (1973). Internal undular surges in Seneca Lake: a natural occurrence of solitons, J. Geophys. Res, 78, pp. 539-548.

49. Huthnance, J. M. (1989). Internal tides and waves near the continental shelf edge, Geophys. Astro. Fluid, 48, pp. 81-106.

50. Huttemann, H. and Hutter, K. (2001). Baroclinic solitary water waves in a two-layer fluid system with diffusive interface, Exp. Fluid, No. 30, pp. 317–326.

51. Inall, M. E., Shapiro, G. I. & Sherwin, T. J. (2001). Mass transport by non-linear internal waves on the Malin Shelf, J. Cont. Shelf. Res., Vol. 21, pp. 1449-1472.

52. Jackson, C. R. (2007). Internal wave detection using the Moderate Resolution Imaging Spectroradiometer (MODIS), J. Geophys. Res., 112, C11012.

53. Jillett, J. B. and Zeldis, J. R. (1985). Aerial observations of surface patchiness of a planktonic crustacean, Bull. Mar. Sci., No. 37, pp. 609-619.

54. Kao, T. W., Pan, F.-S., and Renouard, D. (1985). Internal solitons on the pycnocline: Generation, propagation, and shoaling and breaking over a slope. J. Fluid Mech., Vol.169, No.19–53.

55. Katsumata, K. (2006). Two- and three-dimensional numerical models of internal tide generation at a continental slope, Ocean Modelling, 12, pp. 32–45.

56. Kim, J. and Moin, P. (1985). Application of a fractional step method to incompressible Navier-Stokes equations, J. Comp. Physics, 59, pp. 308–323.

57. Kingsford, M. J. and Choat, J. H. (1986). Influence of surface slicks on the distribution and onshore movements of small fish, Mar. Biol. (Berl.), No. 91, pp. 161-171.

58. Knowlton, N. and Jackson, J. B. C. (2001). The ecology of coral reefs. Marine Community Ecology, M. D. Bertness, S. D. Gaines, and M. E. Hay, Eds., Sinauer Associates, Inc., pp. 395-422.

59. Kubota, T., Ko, D. R. S., Dobbs, L. D. (1978). Propagation of weakly nonlinear internal waves in a stratified fluid of finite depth. AIAA J. Hydrodyn., 12, pp. 157–165.

60. LaFond E. C. (1959). Slicks and temperature structure in the sea, USNEL Report No. 937, pp. 1-35.

61. Lamb, H. (1932). Hydrodynamics, Dover, pp. 370-372.

62. Lamb, K. G. (1997). Particle transport by nonbreaking, solitary internal waves, J. Geophys. Res., Vol. 102, No. C8, pp. 18,641-18,660.

63. Launder, B. E. and Spalding, D. B. (1972). Lectures in mathematical models of turbulence, Academic Press.

64. Legg, S. and Adcroft, A. (2003). Internal wave breaking at concave and convex continental slopes, J. Phys. Oceanogr., 33, pp. 2224–2246.

65. Leichter, J. J., Shellenbarger, G., Genovese, S. J. and Wing, S. R. (1998). Breaking internal waves on a Florida (USA) coral reef: a plankton pump at work?, Mar. Ecol. Prog. Ser., Vol. 166, pp. 83-97.

66. Leichter, J. J., Stewart H. L., and Miller S. K. (2003). Episodic nutrient transport to Florida coral reefs, Limnol. Oceanogr., 48, pp. 1394-1407.

67. Leichter, J. J., Wing, S. R., Mille, S. L., and Denny, M. W. (1996). Pulsed delivery of subthermocline water to Conch Reef (Florida Keys) by internal tidal bores, J. Limnol. Oceanogr., No. 41 (7), pp. 1490-1501.

68. Leonard, B. P. (1979). A stable and accurate convection modelling procedure based on quadratic upstream interpolation. Comput. Methods Appl. Mech. Eng. 19, pp. 59–98.

69. Lin, B. and Falconer R. A. (1997). Tidal flow and transport modeling using ULTIMATE-QUICKEST scheme, J. Hydraul. Eng.-ASCE, Vol. 123, No. 4, pp. 303-314.

70. Longuet-Higgins, M. S. (1953). Mass transport in water waves, Philo. Trans. Royal Soc. London, Series A, Vol. 245 (903), pp. 535-581.

71. Longuet-Higgins, M. S., and Stewart, R. W. (1964). Radiation stress in water waves: A physical discussion, with applications. Deep-Sea Res., 11, pp. 529–562.

72. Love, A. E. H. (1891). Wave-motion in a heterogeneous heavy liquid. Proc. London Math. Soc., 22, pp. 307-316.

73. MacKinnon, J. A. and Gregg, M. C. (2003). Mixing on the late summer New England shelf-Solibores, shear, and stratification, J. Phys. Oceanogr., 33, pp. 1476–1492.

74. Mathur, M. (2011). Laboratory and analytical modeling of internal waves in uniform and non-uniform stratifications, PhD thesis, Massachusetts Institute of Technology.

75. Meyer H. (1904). Totwasser. Ann. Hydr. Mar. Met. 32, 20.

76. Michallet, H. and Ivey, G. N. (1999). Experiments on mixing due to internal solitary waves breaking on uniform slopes, J. Geo-phys. Res., Vol. 104, No. C6, pp. 13, 467-13, 477.

77. Nansen, F. (1904). North Polar Exped. 1893-1896, vol. 5, p. 562.

78. Nguyen, K.-C., Umeyama, M. and, Shintani T. (2012). Water Particle Trajectory and Mass Transport of Internal Waves Propagating Over A Constant Slope, J. Applied Mech., JSCE, Vol. 62, pp. 653-660.

79. Noda, H. (1968). A study on mass transport in boundary layers in standing waves, Coastal Engineering Proceedings, 1(11), doi: 10.9753/icce.v11.

80. Osborne, A. R. and Burch T. L. (1980). Internal solitons in the Andaman Sea, Science 208, 451.

81. Patankar, S. V. and Spalding, D. B. (1972). A calculation procedure for heat, mass and momentum transfer in three-dimensional parabolic flows. Int. J. Heat Mass Tran., 15, pp. 1787–1806.

82. Perry, N. R. and Schimke, G. R. (1965). Large amplitude internal waves observed off the north-west coast of Sumatra, J. Geophys. Res., Vol. 70, pp. 2319-2324.

83. Phillips, O. M. (1966). Dynamics of the upper ocean, Cambridge University Press, pp. 261.

84. Pineda, J. (1991). Predictable upwelling and the shoreward transport of planktonic larvae by internal tidal bores, Science, Vol. 253, No. 5019, pp. 548-551.

85. Pineda, J. (1994). Internal tidal bores in the nearshore: Warm-water fronts, seaward gravity currents and the onshore transport of neustonic larvae, J. Mar. Res., No. 52, pp. 427-458.

86. Pinet, P. R. (1992). Oceanography, West Publ. Comp., 576 pp.

87. Pomar, L., Morsilli, M., Hallock, P. and Badenas, B. (2012). Internal waves, under-explored source of turbulence events in the sedimentary record, Earth-Sci. Rev., 111, pp. 56-81.

88. Rayleigh, L. (1883). Investigation of the character of the equilibrium of an incompressible heavy fluid of variable density. Proc. London Math. Soc., 14, pp. 170 - 177.

89. Sandstrom, H., and Elliott, J. A. (1984). Internal tide and solitons on the Scotian shelf: A nutrient pump at work, J. Geophys. Res., 89, pp. 6415–6426.

90. Shand, J. A. (1953). Internal waves on Georgia Strait. Trans., AGU, Vol.34, No.6, pp. 849–856.

91. Shanks, A. L. (1983). Surface slicks associated with tidally forced internal waves may transport pelagic larvae of benthic invertebrates and fishes shoreward. J. Mar. Ecol. Prog. Ser., No. 13, pp. 311-315.

92. Shanks, A. L. (1985). Behavioral basis of internal wave induced shoreward transport of megalopae of Pachygrapsus crassipes, J. Mar. Ecol. Prog. Ser., No. 24, pp. 289-295.

93. Shanks, A. L. (1986). Tidal periodicity in the daily settlement of intertidal barnacle larvae and a hypothesized mechanism for the cross-shelf transport of cyprids. Biol. Bull. (Woods Hole), No. 170, pp. 429-440.

94. Shanks, A. L. (1987). The onshore transport of an oil spill by internal waves, Science, No. 235, pp. 1198-1200.

95. Shanks, A. L. and Wright, W. G. (1987). Internal-wave-mediated shoreward transport of cyprids, megalopae, and gammarids and correlated longshore differences in the settling rate of intertidal barnacles, J. Exp. Mar. Biol. Ecol., No. 114, pp. 1-13.

96. Shimizu, R., Shintani, T. and Umeyama, M. (2005). Instantaneous and Lagragian velocity fields of internal waves on a slope by PIV measurement and numerical simulation. Ann. J. Coastal Engineering, 52, pp. 1-5.

97. Shintani, T. (2005). Dynamic behavior of density interfaces in stratified water body - upwelling and internal wave breaking, PhD thesis, Tokyo Metropolitan University.

98. Shroyer, E. L., Moum, J. N., and Nash, J. D. (2010). Energy transformations and dissipation of nonlinear internal waves over New Jersey's continental shelf, Nonlin. Processes Geophys., Vol. 17, pp. 345-360.

99. Smyth, W. D., Nash, J. D. and Moum, J. N. (2005). Differential diffusion in breaking Kelvin-Helmholtz billows, J. Phys. Oceanogr., 35, pp. 1004–1022.

100. Stastna, M. and Lamb. K. G. (2008). Sediment resuspension mechanisms associated with internal waves in coastal waters, J. Geophys. Res., Vol. 113, C10016, doi: 10.1029/2007JC004711.

101. Stevens, C. L. and Coates, M. J. (1994). Applications of a maximized cross-correlation technique for resolving velocity fields in laboratory experiments, J. Hydraul. Res., IAHR, 32(2), pp. 195-212.

102. Stokes, G. G. (1847). On the theory of oscillatory waves, Trans. Camb. Phil. Soc., 8, pp. 197-229.

103. Thorpe, S. A. (1968). On the shape of progressive internal waves, Phil. Trans. Roy. Soc. [A], Vol. 263, No. 1145, pp. 563-614.

104. Thorpe, S. A. (1971). Asymmetry of the internal wave seiche in Loch Ness, Nature, 231, pp. 306-308.

105. Troy, C. D. and Koseff, J. R. (2005). The generation and quantitative visualization of breaking internal waves, Exp. Fluid, No. 38, pp. 549–562.

106. Tsuji, Y. and Nagata, Y. (1973). Stokes' expansion of internal deep water waves to the fifth order, J. Ocean. Soc. Japan, 29, pp. 61-69.

107. Turner, J. S. (1980). Buoyancy effects in fluids, Cambridge Uni. Press.

108. Umeyama, M. (1998), Second-order internal wave theory by a perturbation method, Mem. Tokyo Metrop. Univ., 48, pp. 137-145.

109. Umeyama, M. (2000). Third-order Stokes internal waves for a density stratified two-layer fluid, Mem., Tokyo Metrop. Univ., 50, pp. 120–136.

110. Umeyama, M. (2002). Experimental and theoretical analyses of internal waves of finite amplitude, J. Waterway, Port, Coastal, and Ocean Eng., ASCE, 128(3), pp. 133-141.

111. Umeyama, M. (2008). PIV techniques for velocity fields of internal waves over a slowly varying bottom topography. J. Waterway, Port, Coastal, and Ocean Eng., ASCE, 134 (5), pp. 286-298.

112. Umeyama, M. and Shintani, T. (2004). Visualization analysis of runup and mixing of internal waves on an upper slope, J. Waterway, Port, Coastal, and Ocean Eng., ASCE, 130(2), 89-97.

113. Umeyama, M. and Shintani, T. (2006). Transformation, attenuation, setup and undertow of internal waves on a gentle slope, J. Waterway, Port, Coastal, and Ocean Eng., Vol. 132, No. 6, pp. 477-486.

114. Umeyama, M., and H. Matsuki. 2011. Measurements of velocity and trajectory of water particle for internal waves in two density layers, Geophys. Res. Letters, 38, AGU, L03612.

115. Umeyama, M., and H. Shinomiya. (2009). Particle image velocimetry measurements for Stokes progressive internal waves, Geophys. Res. Letters, 36(6), AGU, L06603.

116. Venayagamoorthy, S. K. and Fringer, O. B. (2006). Numerical simulations of the interaction of internal waves with a shelf break, Phys. Fluids, 18, 076603.

117. Venayagamoorthy, S. K. and Fringer, O. B. (2007). On the formation and propagation of nonlinear internal boluses across a shelf break, J. Fluid Mech., Vol. 577, pp.137-159.

118. Vlasenko, V. I. and Hutter, K. (2002). Numerical experiments on the breaking of solitary internal waves over a slope-shelf topography, J. Phys. Oceanogr., 32, pp. 1779–1793.

119. Vlasenko, V., Stashchuk, N., and Hutter K. (2005). Baroclinic tides: Theoretical modeling and observation evidence, Cambridge Uni. Press.

120. Wallace, B. C., and Wilkinson, D. L. (1988). Run-up of internal waves on a gentle slope in a two-layered system. J. Fluid Mech., Vol.191, pp.419–442.

121. Wang, Y.-H., Dai, C.-F., and Chen, Y.-Y. (2007). Physical and ecological processes of internal waves on an isolated reef ecosystem in the South China Sea, Geophys. Res. Lett., Vol. 34, AGU, L18609.

122. Wen, J. and Liu, P. L.-F. (1995). Mass transport of interfacial waves in a two-layer fluid system, J. Fluid Mech., Vol. 297, pp. 231-254.

123. Wessels, F. and Hutter, K. (1996). Interaction of internal waves with a topographic sill in a two-layered fluid, J. Phys. Oceanogr., No. 26, pp. 5-20.

124. Wolanski, E. and Deleersnijder, E. (1998). Island-generated internal waves at Scott Reef, Western Australia. Cont. Shelf Res., 18, pp. 1649–1666.

125. Wolanski, E. and Delesalle, B. (1995). Upwelling by internal waves, Tahiti, French Polynesia.Cont. Shelf Res., 15, pp. 357–368.

126. Wolanski, E. and Hamner, W. H. (1988). Topographically controlled fronts in the ocean and their biological influence, Science, 241, pp. 177-181.

127. Wolanski, E. and Pickard, G. L. (1983). Upwelling by internal tides and Kelvin waves at the continental shelf break on the Great Barrier Reef. Aust., J. Mar. Res., 34, pp. 65–80.

128. Wunsch, C. (1971). Note on some Reynolds stress effects of internal waves on slopes, Deep-Sea Res., Vol. 18, pp. 583-591.

129. Ziegenbein, J. (1969). Short internal waves in the Strait of Gibraltar, Deep Sea Res., Vol. 16, pp. 479-487.